Title
Phonon Transport in Ultrahigh and Ultralow Thermal Conductivity Materials

Author
Kang, Joonsang

Publication Date
2019

Peer reviewed|Thesis/dissertation

UNIVERSITY OF CALIFORNIA
Los Angeles

Phonon Transport in Ultrahigh and Ultralow Thermal Conductivity Materials

A dissertation submitted in partial satisfaction

of the requirements for the degree

Doctor of Philosophy in Mechanical Engineering

by

Joonsang Kang

2019

ABSTRACT OF THE DISSERTATION

Phonon Transport in Ultrahigh and Ultralow Thermal Conductivity Materials

by

Joonsang Kang

Doctor of Philosophy in Mechanical Engineering

University of California, Los Angeles, 2019

Professor Yongjie Hu, Chair

Advanced materials with extreme thermal conductivity are critically important for various technological applications including energy conversion, storage, and thermal management. Low thermal conductivity is needed for thermal insulation and thermoelectric energy harvesting, while high thermal conductivity is desirable for efficient heat spreading in electronics. However, practical application deployments are usually limited by the materials availability in nature. Moreover, understanding the fundamental origins for extreme thermal conductivity still remains challenging. My PhD research focuses on finding new thermal materials and unveiling fundamental phonon transport mechanisms in extreme thermal conductivity matters to push the frontier of thermal science.

My dissertation is composed of three topics. The first topic is focused on developing and investigating a new group of ultrahigh conductivity materials. High-quality boron phosphide (BP) and boron arsenide (BAs) crystal are synthesized and measured with thermal conductivities

of 460 and 1300 W/mK, respectively. In particular, our result shows that BAs is the best thermal conductor among common bulk metals and semiconductors. To better understand the fundamental origin of such an ultrahigh thermal conductivity, advanced phonon spectroscopy and temperature dependent characterizations are performed. Our measurements, in conjunction with atomistic theory, reveal that, unlike the commonly accepted rule for most materials near room temperature, high-order anharmonicity through the four-phonon process is significant in BA because of its unique band structure. Our result underscores the promise of using BP and BAs for thermal management and develops microscopic understanding of the phonon transport mechanisms.

The second topic of my thesis is to investigate phonon transport in ultralow thermal conductivity material with a focus on tin selenide (SnSe). SnSe is a recently discovered material for high performance thermoelectricity. However, the thermal properties of intrinsic SnSe remain elusive in literature. To understand the dominant phonon transport mechanisms for the extremely low thermal conductivity of SnSe, temperature-dependent sound velocity, lattice expansion, and Grüneisen parameter was measured. The measurement result shows that high-order anharmonicity introduces strong phonon renormalization and the ultralow thermal conductivity.

The third topic of the thesis is to investigate in-situ dynamic tuning of thermal conductivity in layered materials. A novel device platform based on lithium ion battery is developed to characterize the interactions between ions and phonons of layered materials. We observe a highly reversible modulation and anisotropy of thermal conductivity from phonon scattering introduced by ionic intercalation in the interspacing layers. This study provides a unique approach to explore the fundamental energy transport involving lattices and ions and open up new opportunities in thermal engineering.

The dissertation of Joonsang Kang is approved.

Vijay K. Dhir

Timothy S. Fisher

Jayathi Y. Murthy

Yongjie Hu, Committee Chair

University of California, Los Angeles

2019

Dedicated to my mother

TABLE OF CONTENTS

LIST OF FIGURES

LIST OF TABLES

ACKNOWLEDGEMENTS

I am deeply indebted to my PhD advisor Prof. Yongjie Hu. The completion of my thesis would not have been possible without his advice and support. He motivates and inspires me for research. Also, he gives me a lot of research freedom which makes me more focused on my research interest. I have enjoyed the time since I came to UCLA with an empty lab: I started struggling with setting up TDTR, material synthesis and measurement tools, while have discussed a lot with him. It has been very fruitful to learn fundamentals of research and it was invaluable experience in my life.

I appreciate Prof. Vijay Dhir, Prof. Timothy Fisher, and Prof. Jayathi Murthy for serving on my PhD thesis committee and their invaluable comments on my works.

Thanks should also go to my labmates Man, Huan, Nicolas, Huu, and Ming. Many of my research would not be able to work without their help. Lots of discussion with them was very instrumental for my research and understanding.

I'd like to acknowledge UCLA research facility staffs Noah, Dr. Sergey, Dr. Khan, Dr. Martini. They trained me how to use instruments. I also deeply appreciate Dr. Aoki in UC Irvine who has spent a lot of time for TEM analysis of my sample; he is the best TEM specialist in SoCal.

I also sincerely thank my former advisor Prof. Sang Soo Kim. Without his generous help and guidance, I cannot even think about starting my PhD degree. I owe a great debt to him.

I am extremely grateful to my parents for their unconditional love, devotion, and sacrifice for me. There is no way to express my utmost gratitude and thanks to them.

In retrospect, I have always been one step behind others in degree, study and research. Without the help and support from my advisor, colleagues, friends, and family, I would not get my degree done. I heartfully thank to all of them.

VITA

EDUCATION

2012 M.S. in Mechanical engineering, Korea Advanced Institution of Science and Technology

2010 B.S. in Mechanical engineering, Inha University

RESEARCH EXPERIENCE

2014-2019 Research assistant, Mechanical engineering department, University of California Los Angeles

2012-2014 Researcher, Center for Environment, Korea Institution of Science and Technology

2010-2012 Research assistant, Mechanical engineering department, KAIST

AWARD

2019 Gold Winner of Graduate Student Award, Material Research Society

2018 Northrop Grumman Fellowship, Northrop Grumman-UCLA

SELECTED PUBLICATION

J. S. Kang, M. Li, H. Wu, H. Nguyen, and Y. Hu, "Basic physical properties of cubic boron arsenide", ***Appl. Phys. Lett***., 2019, 115, 122103.

J. S. Kang, H. Wu, M. Li, and Y. Hu, "Intrinsic ultralow thermal conductivity and phonon renormalization due to strong anharmonicity of single-crystal Tin Selenide", ***Nano Lett***., 2019, 19(8), 4941-4948

J. S. Kang, M. Li, H. Wu, H. Nguyen, and Y. Hu, "Experimental observation of high thermal conductivity in boron arsenide", ***Science***, 2018, 361(6402), 575-578

J. S. Kang, H, Wu, and Y. Hu, "Thermal properties and phonon spectral characterization of synthetic boron phosphide for high thermal conductivity applications", ***Nano Lett.,*** 2017, 17 (12), 7507-7514

J. S. Kang, M. Ke, and Y. Hu, "Ionic intercalation in two-dimensional van der Waals materials: in situ characterization and electrochemical control of the anisotropic thermal conductivity of black phosphorus", ***Nano Lett***., 2017, *17* (3), 1431–1438.

PATENT

Y. Hu and **J. S. Kang**, "HIGH THERMAL CONDUCTIVITY BORON ARSENIDE FOR THERMAL MANAGEMENT, ELECTRONICS, OPTOELECTRONICS, AND PHOTONICS APPLICATIONS", PCT/US2019/016255.

Y. Hu and **J. S. Kang**, "BORON PHOSPHIDE-BASED MATERIALS FOR THERMAL MANAGEMENT AND THERMAL DEVICE APPLICATIONS", PCT/US2018/053986

CHAPTER 1

Introduction

1.1 Motivation and background

Heat conduction is fundamental thermal energy transport and usually governed by Fourier's law ($q_x" = -\kappa_x dT/dx$). Heat flux is linearly proportional with temperature gradient and proportional constant is thermal conductivity. Thermal conductivity is the key parameter in a choice of materials in electronics, thermal insulator, and energy harvesting applications. Especially, ultrahigh or ultralow thermal conductivity are very desirable for many technological applications. For example, heat dissipation is becoming an increasingly critical technology challenge for modern electronics and photonics due to the continuous shrinking of devices down to the nanoscale. Ultrahigh thermal conductivity materials that can efficiently spread heat from local hot spots and improve device performance are urgently needed to address this challenge. On the other hands, in thermoelectric device, heat to electricity conversion efficiency is function of figure of merit (ZT) which is inversely proportional with thermal conductivity. Thus, low thermal conductivity is desirable to maximize conversion efficiency.

Researchers have hunted ultralow and ultrahigh thermal conductivity materials for a long time, but the choice of materials has been very limited up to date. Moreover, understanding the fundamental origins of heat transport in an extreme thermal conductivity material still remain challenging and leads to a bottleneck in state-of-art technology applications.

Fundamentally, in dielectric materials such as semiconductor and electrical insulator, thermal transport is governed by lattice vibration which is called phonon. Phonon can be described as quantized quasi-particle and phonon thermal conductivity by kinetic theory is expressed by

$$\kappa = \frac{1}{3}\sum_{p}\int C_v(\omega,p)v_g(\omega,p)\Lambda(\omega,p)\,d\omega \qquad (1\text{-}1)$$

where the C, v, Λ, ω, and p are the volumetric specific heat, phonon group velocity, mean free path of phonon, frequency of phonon, and polarization of phonon respectively. Equation (1-1) can be applicable in crystalline material which has long range of ordered and collective atomic motion. Specific heat and phonon group velocity are closely related with compound of elements and crystal structure of materials. Once crystal is determined, these are not largely affected by other conditions. On the other hands, mean free path of phonon is highly correlated with crystallinity, impurities, grain boundary, and scattering with another energy carrier (e.g. electron or magnon) inside of a sample. For example, specific heat and phonon group velocity of poly/single crystal or doped/undoped silicon is almost identical. However, mean free path spectra of phonon is significantly different resulting in large difference of thermal conductivity. Thus, knowing mean free path spectra is key to understand thermal transport in materials.

My PhD work focuses on investigating new extreme thermal conductivity materials and developing advanced experimental methodology to understand fundamental physics behind extreme thermal transport. Phonon spectroscopy and phonon anharmonicity measurement technique are deployed to quantify mean free path and anharmonicity of phonon. Also, atomistic simulation is conducted for better understanding of thermal physics in my experiment. This thesis will provide new physical understanding in thermal science and enable a rational design of

device for high performance technology applications.

1.2 Outline of the dissertation

In this dissertation, I will present thermal transport in ultralow and ultrahigh thermal conductivity materials as well as dynamic thermal conductivity tuning.

In chapter 2, I introduce ultrafast pump-probe spectroscopy which is called time-domain thermoreflectance (TDTR) method for thermal conductivity measurement. I set it up in our lab by myself and intensively used during my PhD work. With explanation about each optical component in TDTR set up, I also provide thermal modeling with detailed mathematical derivation. Also, measurement principle of sound velocity of materials is described.

In Chapter 3, I describe experimental observation of ultrahigh thermal conductivity in boron compounds which are boron phosphide and boron arsenide. I describe that detailed material synthesis, characterization, thermal conductivity measurement, and phonon spectroscopy.

In Chapter 4, I report unknown physical properties of BAs for its thermal, mechanical, and optical applications. Knowing these properties are very important in order to apply BAs to various applications. I measured bandgap, refractive index, elastic/shear modulus, Poisson's ratio, and thermal expansion coefficient.

Chapter 5 is for ultralow thermal conductivity in single crystal. I measured ultralow anisotropic thermal conductivity in tin selenide (SnSe). I revealed origin of ultralow thermal conductivity by developing new experimental methodology which can measure phonon anharmonicity.

In Chapter 6, I describe dynamic control of thermal conductivity in layered materials. I will show how external ion interaction with phonon and thermal transport in crystal. Ion and phonon

coupling can significantly reduce thermal conductivity of material and can used for dynamic thermal conductivity modulation.

Chapter 7 is conclusion of this dissertation.

CHAPTER 2

*Ultrafast optical spectroscopy for thermal conductivity and acoustic measurements**

2.1 Introduction to ultrafast optical spectroscopy measurement

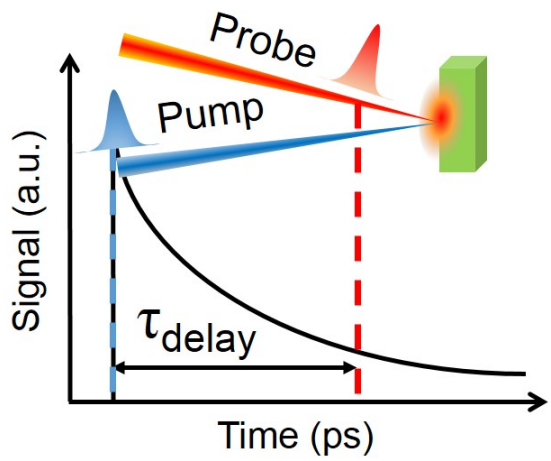

Figure 2.1 *Principle of TDTR*

In analogous with laser flash method, time-domain thermoreflectance (TDTR) is the transient optical technique to measure the thermal conductivity of materials. Figure 2.1 shows that working mechanism of TDTR method. TDTR is composed of two pulse beam called 'pump' and 'probe' beam.

*Part of this chapter is adopted from J. S. Kang et al, *Appl. Phys. Lett*., 2019, 115, 122103. J. S. Kang, et al., *Nano Lett*., 2019, 19(8), 4941-4948. J. S. Kang et al., *Science*, 2018, 361(6402), 575-578. J. S. Kang et al., *Nano Lett.*, 2017, *17* (3), 1431–1438.)

When the pump beam pulse is exited on the sample surface, sample absorb laser pulse energy and it is converted to the heat energy which generates a sharp temperature rise on the sample surface. Before the next pulse is arrived, the temperature of sample surface continuously decays. The transient temperature decay due to this heat impulse is detected by observing reflectance change of the probe pulse. In different with traditional thermal conductivity measurement such as laser flash method, the TDTR method has much higher spatial sensitivity (i.e. probing small volume below 10 μm^3) and temporal sensitivity (sub-picosecond). Such improvement over measurement sensitivity can minimize possible scattering effects from boundaries or defects in the large scale and has been approved with reliable measurement for wide range of thermal conductivity samples.

2.2 Working principle of conventional TDTR

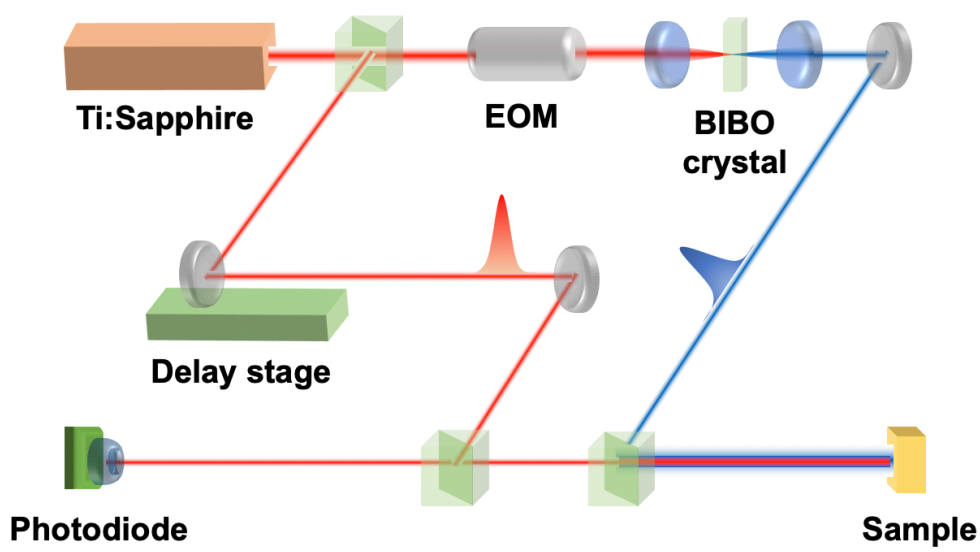

Figure 2.2 *Schematic of TDTR experimental setup*

Figure 2.2 shows that the experimental schematic of TDTR method. Ti:Sapphire oscillator (Tsunami, Spectra-physics) generates 800nm wavelength, femto-second pulse width (~100fs), and 80MHz repetition rate beam. Astigmatic and elliptic beam shape of Ti:Sapphire laser is corrected by a pair of cylindrical lenses and spherical lenses. The beam is divided into pump and probe beam by polarizing beam splitter with large ratio. The pump beam is sinusoidally modulated by passing through the electro-optic modulator (EOM) up to 20MHz and fundamental frequency of pump beam is doubled by bismuth triborate crystal (BIBO). Probe beam is delayed using mechanical delay stage from 0 to 6 ns. The probe beam measures the reflectance change by pump beam. We use concentric and relatively large beam spot size for cross-plane κ measurement. (~ 20μm ($1/e^2$ diameter)). The reflectance signal is measured and recorded by lock-in amplifier connected with EOM, providing detectable in-phase signal (V_{in}) and out-phase signal (V_{out}). The amplitude, $\sqrt{V_{in}^2 + V_{out}^2}$ and phase signal, $\tan^{-1}(-V_{in}/V_{out})$ are used to compare with thermal model for extracting thermal properties.

The reflectance signal of linear time invariant system detected by RF lock-in amplifier is expressed by[1,2]

$$Z(f_0) = P\sum_{N=-\infty}^{\infty} H(f_0 + Nf_s)\exp(iNf_s\tau) \qquad (2\text{-}1)$$

where f_0, f_s, N, and τ are the modulation frequency, probe frequency, integer, and delay time. The P is constant including the thermoreflectance coefficient, laser power, and electronics gain. The H is the temperature response in frequency domain which is modeled from transient heat conduction equation. I will describe it below. The in-phase signal (V_{in}=Re[Z(f_0)]) is related with temperature response from sample surface and the out-of-phase signal (V_{out}=Im[Z(f_0)]) is from the imaginary temperature oscillation[3].

Transient heat conduction equation in cylindrical geometry can be expressed by

$$C_v \frac{\partial T}{\partial t} = \frac{\kappa_r}{r}\frac{\partial}{\partial r}(r\frac{\partial T}{\partial r}) + \kappa_z \frac{\partial^2 T}{\partial z^2} \qquad (2\text{-}2)$$

where the C_v, T, κ_r, and κ_z are the volumetric specific heat, temperature, in-plane thermal conductivity, and cross-plane thermal conductivity, respectively. After taking zeroth-order of Hankel transform and Fourier transform, equation (2-2) is expressed by

$$\rho C_p iw\overline{T} = -\kappa_r k^2 \overline{T} + \kappa_z \frac{\partial^2 \overline{T}}{\partial z^2} \qquad (2\text{-}3)$$

Then, equation (2-3) can be rewritten and rearranged by defining β,

$$\beta^2 \overline{T} = \frac{\partial^2 \overline{T}}{\partial z^2} \qquad (2\text{-}4)$$

where the β is

$$\beta \equiv \sqrt{\frac{C_v iw + \kappa_r k^2}{\kappa_z}} \qquad (2\text{-}5)$$

The general solution of equation (2-4) is

$$\overline{T} = a\exp(\beta z) + b\exp(-\beta z) \qquad (2\text{-}6)$$

where the a and b are the constants which is determined by boundary condition. Heat flux can be expressed by applying Fourier's law which is

$$q = -a\beta\kappa_z \exp(\beta z) + b\beta\kappa_z \exp(-\beta z) \qquad (2\text{-}7)$$

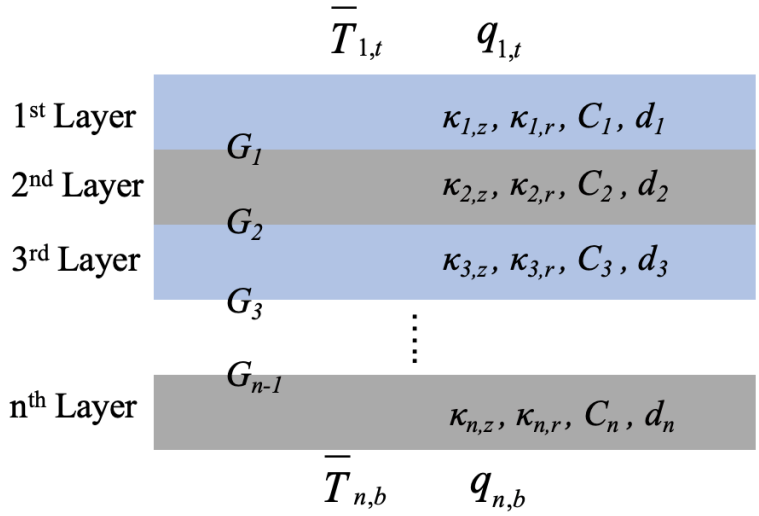

Figure 2.3 *Schematic of multilayer heat conduction model for TDTR*

Let define $\overline{T}\big|_{z=0}$, $\overline{T}\big|_{L=d}$, $q\big|_{z=0}$,and $q\big|_{L=d}$ to T_t, T_b, q_t, and q_b. By using matrix form, these can express to[1]

$$\begin{pmatrix} T_b \\ q_b \end{pmatrix} = \begin{pmatrix} a_{11} & a_{12} \\ a_{21} & a_{22} \end{pmatrix} \begin{pmatrix} T_t \\ q_t \end{pmatrix} \qquad (2\text{-}8)$$

By putting equation equation (2-6) and (2-7) into equation (2-8), constants a and b can be eliminated and each matrix component can be obtained,

$$\begin{pmatrix} T_b \\ q_b \end{pmatrix} = \begin{pmatrix} \cosh(\beta d) & -\dfrac{1}{\kappa_z \beta}\sinh(\beta d) \\ -\kappa_z \beta \sinh(\beta d) & \cosh(\beta d) \end{pmatrix} \begin{pmatrix} T_t \\ q_t \end{pmatrix} = (J) \begin{pmatrix} T_t \\ q_t \end{pmatrix} \qquad (2\text{-}9)$$

At the interface, because thermal interface conductance is defined by[4]

$q_{i,b} = q_{i+1,t} = G(T_{i,b} - T_{i+1,t})$, where the i is i-th layer of sample, equation (2-9) is expressed by

$$\begin{pmatrix} T_{i+1,t} \\ q_{i+1,t} \end{pmatrix} = \begin{pmatrix} 1 & -\frac{1}{G} \\ 0 & 1 \end{pmatrix} \begin{pmatrix} T_{i,b} \\ q_{i,t} \end{pmatrix} = (S) \begin{pmatrix} T_{i,b} \\ q_{i,t} \end{pmatrix} \qquad (2\text{-}10)$$

In multi-layer structure, equation (2-9) and (2-10) are combined and written as

$$\begin{pmatrix} T_{n,b} \\ q_{n,b} \end{pmatrix} = (J)_n (S)_{n-1} (J)_{n-1} (S)_{n-2} \ldots (J)_1 = \begin{pmatrix} A_{11} & A_{12} \\ A_{21} & A_{22} \end{pmatrix} \begin{pmatrix} T_{1,t} \\ q_{1,t} \end{pmatrix} \qquad (2\text{-}11)$$

where J_n, S_{n-1}, J_{n-1}, ..., J_n are the n-th layer of matrix shown in equation (2-9) and (2-10) from top layer. The $T_{1,t}$ and $q_{1,t}$ are the temperature and heat flux on the top of first layer. The $T_{n,b}$, and $q_{n,b}$ are the temperature and heat flux on the bottom of last layer. If last layer is adiabatic or semi-infinite (this assumption is valid in our experiment because of high frequency heating), heat flux $q_{n,b}$ will be zero and equation (2-11) can be written to

$$T_{1,t} = -\frac{A_{22}}{A_{21}} q_{1,t} \qquad (2\text{-}12)$$

Heat flux in our experimental geometry is from laser heating. The gaussian beam intensity is

$$I_{pump} = \frac{2P_{pump}}{\pi w^2} \exp\left(\frac{-2r_{pump}^2}{w^2}\right) \qquad (2\text{-}13)$$

Hankel transform of equation (2-13) is

$$\bar{I}_{Pump} = \frac{P_{pump}}{2\pi} \exp\left(\frac{-k^2 w_{pump}^2}{8}\right) \qquad (2\text{-}14)$$

Put equation (2-14) into equation (2-12) with gaussian weighted average with probe beam. Then, equation (2-11) will be

$$\bar{T}_{1,t} = -\frac{A_{22}}{A_{21}} \frac{P_{probe} P_{pump}}{4\pi^2} \exp\left(\frac{-k^2 (w_{pump}^2 + w_{probe}^2)}{8}\right) \qquad (2\text{-}15)$$

By taking inverse Hankel transform,

$$H(f) = \frac{P_0}{2\pi}\int_0^{\infty} -\frac{A_{22}}{A_{21}}\exp\left(-\frac{k^2(w_{pump}^2 + w_{probe}^2)}{8}\right)k\,dk \qquad (2\text{-}16)$$

Equation (2-16) is applicable to multiple advanced TDTR system such as elliptical beam TDTR or beam offset TDTR method by changing boundary conditions.

2.3 Extend to beam offset TDTR

Although the heat conduction model for conventional TDTR includes κ_r, it is not sensitive to κ_r because conventional TDTR typically use high modulation frequency with large beam diameter. However, when the pump beam spot size is comparable or smaller than the in-plan thermal penetration length,

$$L_p = \sqrt{\frac{\kappa_r}{\pi C_v f_0}} \qquad (2\text{-}17)$$

κ_r is sensitive to measure.

To examine the in-plane anisotropic property, we introduced beam offset TDTR (BO-TDTR) technique. In BO-TDTR, the pump and probe beams are separated with an offset distance at the sample surface. We use small beam diameter and low modulation frequency to satisfy root mean square diameter ($\sqrt{w_{pump}^2 + w_{probe}^2}$) is smaller than L_p.

Governing equation of beam offset TDTR measurement is expressed by modifying equation (2-16)[1].

$$H(f) = \left(\frac{2}{\pi w_{probe}^2}\right)\int_{-\infty}^{\infty}\int_0^{\infty} T\left(\sqrt{(x-x_0)^2 + y^2}\right)\exp\left(\frac{-2(x^2+y^2)}{w_{probe}^2}\right)dxdy \quad (2\text{-}18)$$

beam offset in lateral direction contains in-plan thermal properties of sample and V_{out} become proportional to the exp $(-x_0^2/L_p^2)$ where x_0 is the offset between pump and probe beam[5,6]. We first perform conventional TDTR to obtain κ_r and G, then fix two values in our thermal model then fit our data with equation (2-18).

The out-of-phase thermoreflectance signal (V_{out}) at short negative delay time (-50 ps) which small modulation frequency is used to determine the in-plane thermal conductivity. The beam diameter is measured with both knife-edge beam profiler (BP-209VIS) and TDTR signal at short positive probe delay time (+50ps) with high modulation frequency (9.8MHz). Pump beam is swept by motorized piezo-mirror mount (Newport model 8809) with 0.7 μrad of step resolution, or corresponding to a spatial resolution down to 2 nm on the sample surface.

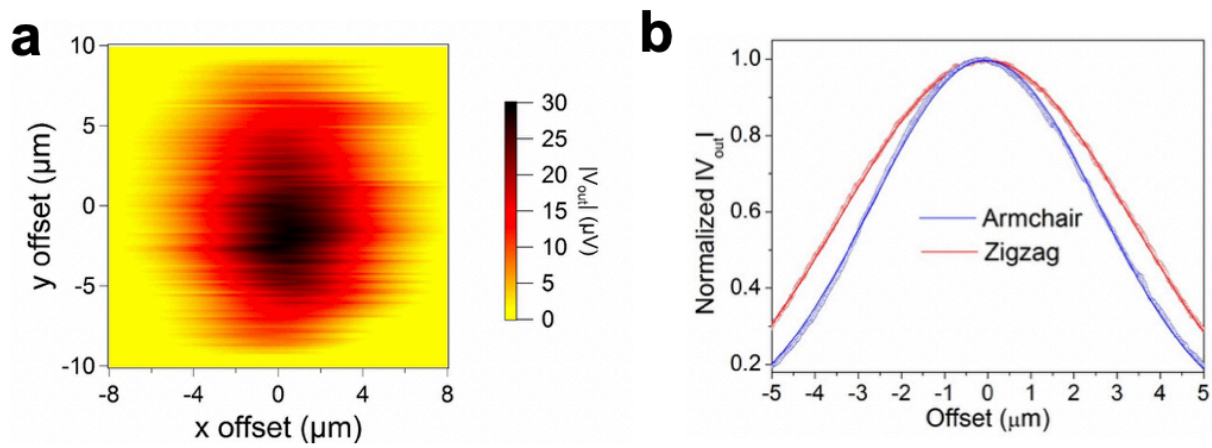

***Figure 2.4**. In-plan thermal conductivity measurement of pristine BP. (a) In-plane V_{out} map as a function of beam offset, x and y axis indicate beam offset between pump and probe beam to each direction. The color bar shows that the intensity of V_{out}; (b) κ of pristine BP to armchair and zigzag direction. Open circles represent experimental data and the solid line is best fitting. The red color and blue color represent κ_{ZZ} and κ_{AC} respectively.*

The V_{out} signal is recorded by lock-in amplifier and thermal model fitting is performed to extract the FWHM of V_{out} signal. The FWHM is converted to in-plane κ by thermal conductivity

tensor model. For in-plane fitting, the cross-plane thermal conductivity and interface conductance is included in the thermal model. The in-plane analysis was performed iteratively with the cross-plane analysis. By extracting full width half maximum (FWHM ~ κ), in-plan thermal conductivity can be obtained along with beam offset direction[6].

Figure 2-4a shows a two-dimensional data plot of V_{out} for black phosphorus sample as a function of beam offset. The in-plane thermal conductivity along the two different crystal orientation direction zigzag (ZZ) and armchair (AC) directions are obtained by fitting the full-width-at-half-maximum (FWHM) of V_{out} over the beam offset distance along respective directions. Typical experimental data from our BO-TDTR measurement and fittings are shown in Fig.2-3b. We used κ_z and interface conductance obtained from cross-plane measurement to extract κ_{ZZ} and κ_{AC}. The in-plane κ of pristine BP are measured to be κ_{ZZ} = 85.80 $W \cdot m^{-1} \cdot K^{-1}$ and κ_{AC} = 27.58 $W \cdot m^{-1} \cdot K^{-1}$. The measured thermal conductivity of pristine BP is consistent with results in recent independent studies[7–9].

2.4 Sound velocity measurement

Ultrafast pump-probe spectroscopy is also powerful tool to examine mechanical properties of materials by measuring sound velocity of material. Sound velocity is not only parameter to determine mechanical properties of materials but also important indicator of thermal properties of material. Fig. 2.5a illustrates the working principle of longitudinal sound velocity measurement, where a laser pump generates a picosecond acoustic pulse from the surface that penetrates into the sample. The acoustic pulse is generated by strain from thermal expansion of top metal transducer. When the acoustic pulse reaches the interface between metal

transducer and sample interface, it partially reflects back to top surface and partially pass through interface, it partially reflects back to top surface and partially pass through interface.

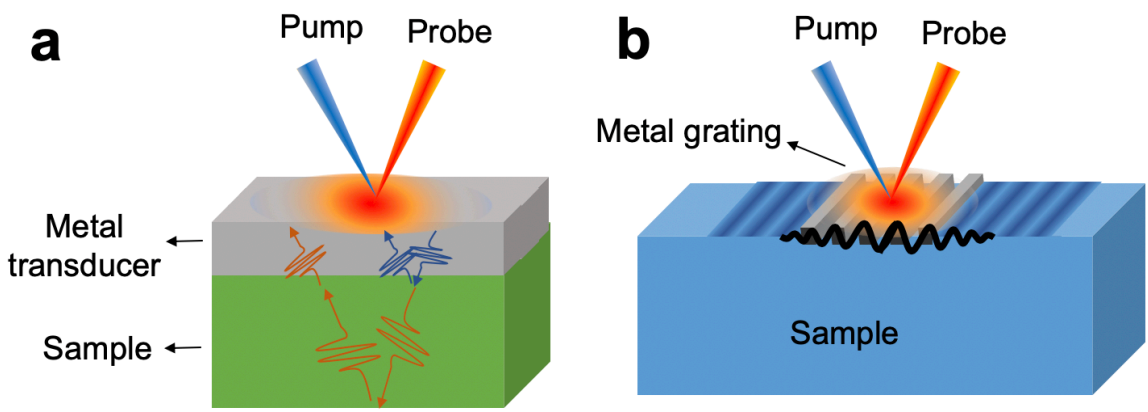

Figure 2.5 *Schematic of sound velocity measurement. (a) Longitudinal sound velocity measurement. (b) Surface acoustic wave velocity measurement.*

The penetrated pump pulse reach boundary of sample and reflect back at the top surface. Each reflection creates sound echo. The sound echoes return to the surface and are detected by a laser probe (Fig. 3b). The time delay (Δt_{echo}) between echoes is measured and contributed to by the round trip of the acoustic wave in the sample film with thickness *d*. Therefore, the longitudinal sound velocity is calculated by $v_L = 2d / \Delta t_{echo}$.

Also, surface acoustic wave (SAW) velocity which is described by stiffness of sample can be measured by pump-probe method with metal grating. Figure 2.5b shows schematic of SAW measurement. When periodic metal grating lines (with a period of L) were fabricated on the surface samples and heated up by a pump laser, it generates periodic thermal strains that

partially pass through the underneath sample to form SAWs[10]. The SAW propagates along the sample surface with strong periodic oscillations with a time periodicity of Δt_{SAW}. Oscillation of reflectance signal is detected by following probe laser. SAW velocity is determined by $v_{SAW} = L / \Delta t_{SAW}$.

CHAPER 3

*Ultrahigh thermal conductivity in boron compounds**

3.1 Introduction

The decreasing size of modern electronics makes heat dissipation one of the most critical technological challenges. The worldwide semiconductor industry, which has powered the information technology revolution since the 1960s, acknowledged in 2016 that Moore's law is nearing its end[11]. A major issue is the enormous amount of waste heat generated during electronic device operation[12]. For example, a U.S. data center devotes about 50% of its total electricity use to cooling[13]. At the nanoscale, the power density of hot spots in current transistors is approaching that of the Sun's surface[14]. Low thermal conductivity and heat dissipation rates severely degrade the performance and energy efficiency of electronic and photonic devices. Thermal management is arguably the biggest roadblock for next-generation devices, such as microprocessors and integrated circuits, light-emitting diodes (LEDs), and high-power radio frequency (RF) devices, to just name a few[11,14].

Discovering high thermal conductivity (HTC) materials is needed to enable efficient heat dissipation from hot spots and improve device performance. So far, much of the research is focused on carbon-based crystals—diamond and graphene. While these materials can have exceptional heat transfer properties, there are several drawbacks for wide-spread use.

(*The work described in this chapter was done in collaboration with M. Li, H. Wu, and H. Nguyen and was the basis for the articles published in *Science*, 2018, 361(6402), 575-578 and *Nano Lett*., 2017, 17 (12), 7507-7514.)

Diamond, the most developed material for passive cooling of high-power electronics, suffers from high cost, slow synthesis rates, low quality, and challenging integration with semiconductors. Degradation of thermal conductivity plagues graphene and nanotubes when assembled into practical sizes due to ambient interactions and disorder scattering. Their intrinsic anisotropy creates other challenges for applications.

Fundamentally, understanding the origins of HTC remains a challenge. The conventionally accepted criteria for HTC materials are: (i) small average atomic mass (M_{ave}); (ii) strong interatomic bonding; (iii) simple crystal structure; and (iv) low anharmonicity [15–17]. Criteria (i) and (ii) imply a large Debye temperature (θ_D), and provide the commonly used rule of thumb that thermal conductivity increases with decreasing M_{ave} and increasing θ_D. Diamond is the prototypical crystal. Diamond's two-atom primitive unit cell, light carbon mass, and stiff covalent bonding result in an exceptionally high value for thermal conductivity. Recent ab initio calculations show excellent agreement with the measured thermal conductivity of a wide range of materials [17–25], including silicon, diamond, graphene, and carbon nanotubes. Such calculations provide new physical insights into the nature of the phonon thermal transport and the HTC mechanism. Recent ab initio theoretical work indicates that the conventional criteria for materials are incomplete and points to new ones stemming from fundamental vibrational properties that can lead to HTC. These new criteria applied to binary compounds are: (i) a large mass ratio of constituent atoms; (ii) bunching together of the acoustic phonon branches; and (iii) an isotopically pure heavy atom. The large mass ratio provides a large frequency gap between acoustic and optic phonons (a-o gap). According to materials examined thus far, bunching of the acoustic phonon dispersions tends to occur in crystals with light constituent atoms, such as boron and carbon, where it derives from an unusual interatomic bonding that lacks core p electrons.

Criteria (i) and (ii) contribute to unusually weak phonon-phonon scattering and a large intrinsic thermal conductivity, while criteria (i) and (iii) cause relatively weak scattering of phonons by isotopes.

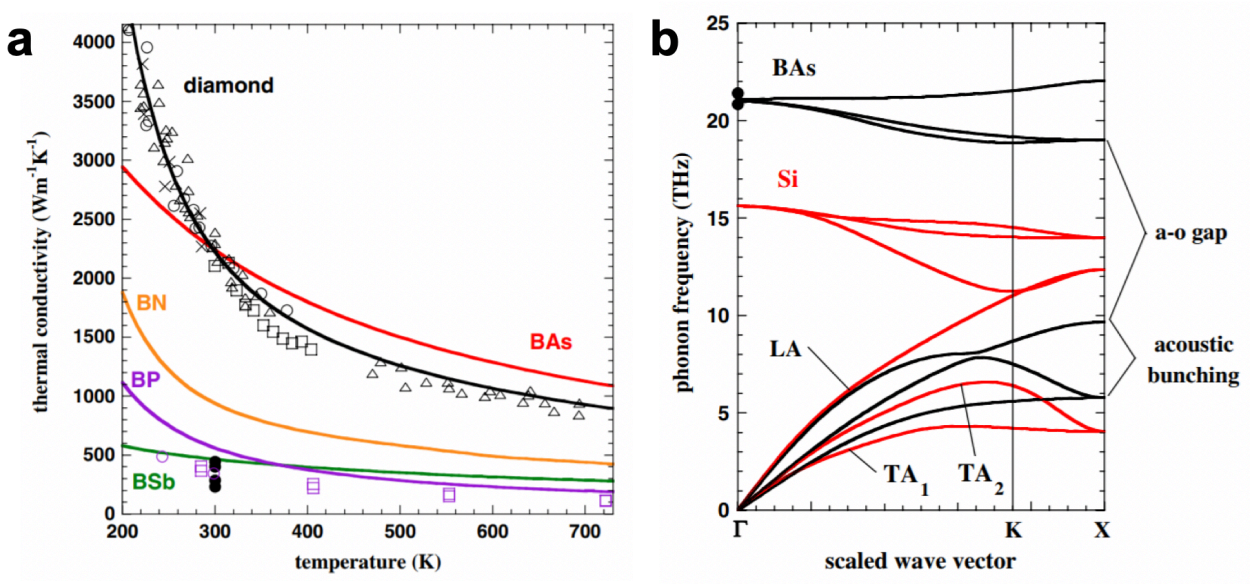

Figure 3.1 *Thermal conductivity prediction in boron compound*[17]*. a) Temperature dependent thermal conductivity of boron compound and diamond. b) Phonon dispersion of boron arsenide.*

The ab initio theory (Fig.3.1) identified the III-V zinc blende compound, defect-free BAs, as having an exceptionally HTC of over 1,000 W/mK[17,25]. This predicted HTC exceeds that of most state-of-the-art HTC materials and more than triples that of the current industrial HTC standard, i.e., silicon carbide. BAs possesses an advantageous combination of properties that incorporates both conventional (light boron mass and stiff almost pure covalent bonding) and new criteria (large arsenic to boron mass ratio, bunching together of its acoustic phonon branches, and isotopically pure As (heavy) atom).

Experimental efforts to synthesize and characterize BP and BAs has been scarce. Although the growth of cubic BP and BAs was reported in the 1960s, its detailed structural characterization and properties were never reported. Generally, boron-related materials are notably difficult to obtain in dense bulk form. The synthesis of BAs and BP is further complicated by the high volatility of arsenic and phosphorus the introduced vacancy defects, as well as the possible formation of sub-phases (e.g., $B_{12}As_2$ and $B_{12}P_2$). Here, I synthesized high-quality single-crystal BP and BAs crystal and measured an ultrahigh thermal conductivity of 460 W/mK and 1300 W/mK, respectively. This exceeds most HTC materials and is consistent with the ab initio prediction.

3.2 Crystal growth and characterization

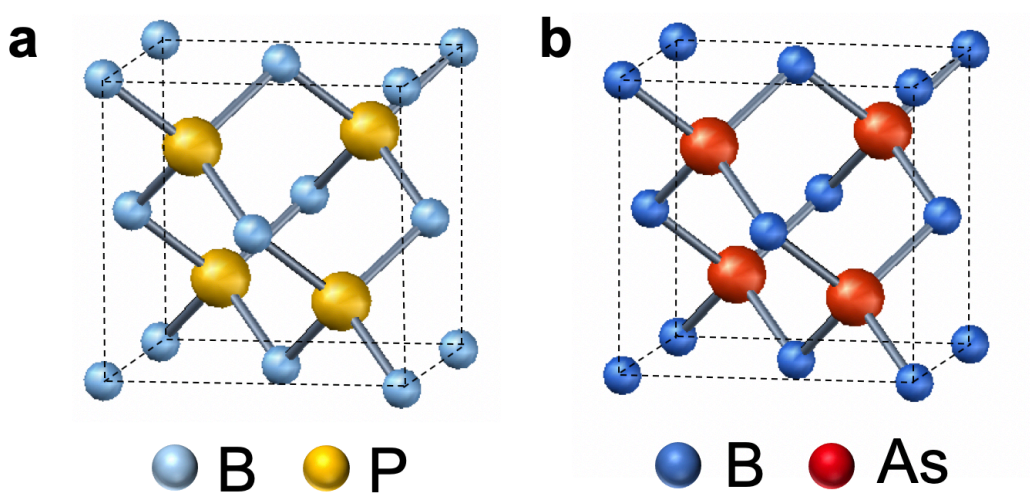

Figure 3.2 *Crystal structure of (a) BP and (b) BAs*

BP and BAs are III-V materials which has a zinc-blende face-centered cubic (FCC) crystal structure in the $F\bar{4}3m$ space group, where boron and phosphorus (BP) or arsenide (BAs) atoms are interpenetrating and covalently bonded to form a tetrahedral geometry shown in Fig. 3.2.

High quality single crystal BP is synthesized by solution growth method. Stoichiometric ratio of high-purity boron, nickel, and red phosphorus powder (99.99% purity, from Alfa Aesar) are placed into a quartz tube. The quartz tube is evacuated and flame sealed under high vacuum (10^{-5} torr). The quartz tube is placed into the customized reaction furnace and heated up to 1373 K and held on the temperature for 4 days, then slowly cool down to room temperature. The reaction steps are repeated to achieve high quality crystals. After finishing reaction, aqua regia solution is used to purify BP, followed by acetone and isopropanol wash before material characterization and thermal measurement.

On the other hands, BAs was prepared through chemical vapor transport. To minimize defects and built-in stress introduced by lattice mismatch and thermal expansion, single-crystal BP was used as the growth substrate. High-purity boron and arsenic coarse powders (99.9999% purity, from Alfa Aesar) were ground by using mortar and pestle, prior to introduction into a quartz tube at a stoichiometric ratio of 1:2. After we loaded our reaction sources, the quartz tube was evacuated and flame sealed under high vacuum (10^{-5} Torr) before placement into a customized three-zone reaction furnace with a 1083 K hot zone, 1058K center zone and a 1033K cold zone. After 5 weeks at these temperatures, the quartz tube and its content were slowly cooled down to room temperature. These reaction steps were repeated until BAs single crystals of high quality were obtained.

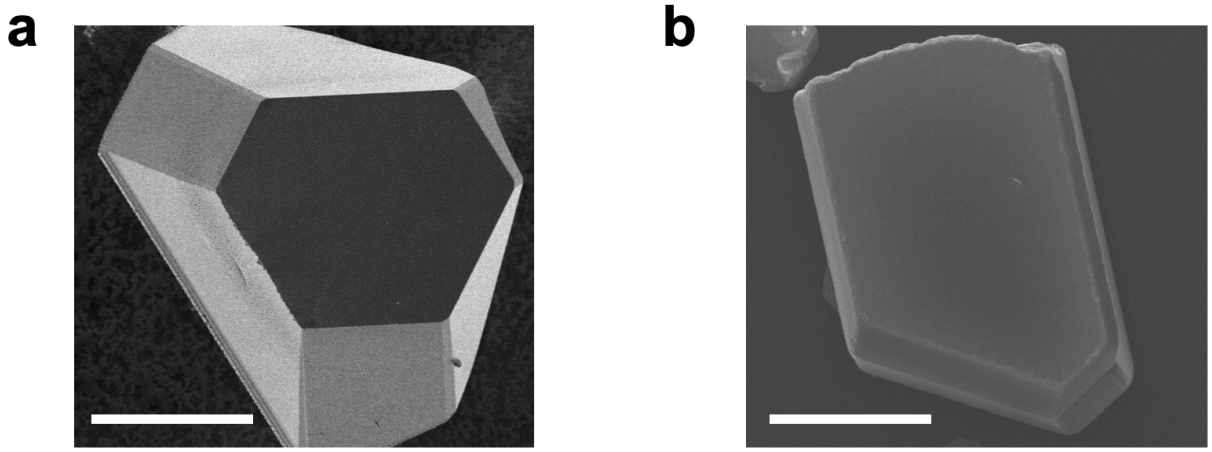

Figure 3.3 *Scanning electron microscope image of (a) BP and (b) BAs. Scale bars are 50 µm.*

Figure 3.3 shows a typical SEM image of the as-synthesized BP and BAs crystal. These crystals obtained from aforementioned method are with size distribution from 50 to 500 µm, and mostly hexagon or triangle shape with the main face of {111} orientation. The crystal morphology of BP and BAs is consistent with its crystal structure and growth kinetics. During the BP and BAs growth, {111} crystal orientation of the BP and BAs has the slowest growing rate because of the high energy of nucleation and usually tends to form the smooth top surface of crystals as seen in the SEM image (Figure 3.3). This growing restriction makes stable formation of hexagonal shape of BP and BAs bound by {111} plane and allow faster crystal growth to the {110} and {100} directions[26].

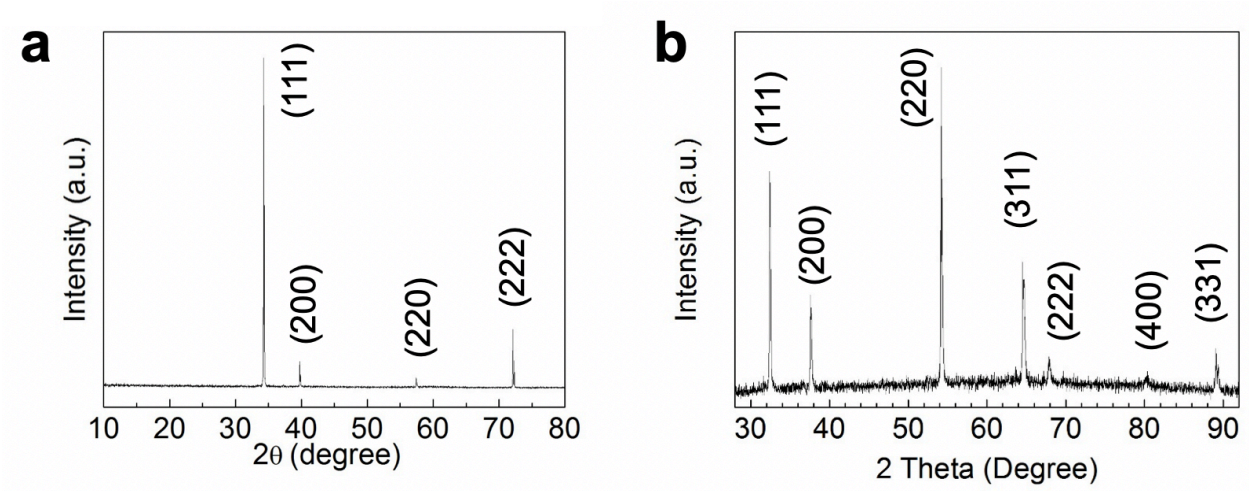

Figure 3.4 *Powder XRD data of (a) BP and (b) BAs*

The crystal structures of BP and BAs are verified by powder X-ray diffraction (P-XRD). We collect sample crystals to obtain enough measurement signal. Samples of BP and BAs crystals were gently separated from the growth substrate and transferred to the zero-diffraction substrate. P-XRD was conducted with a Cu Kα radiation source. The diffractometer was operated at 45 kV and 40 mA. After measurement, the diffraction peaks were matched with the material data directory and identified as BP and BAs crystals. Figure 3.4 shows that P-XRD data of BP and BAs. Each P-XRD data shows very sharp diffraction peaks of minimum width and agrees with the expectation from different crystal planes with no observation of any additional impurity peaks. The lattice constants of BP and BAs obtained from XRD measurement are 4.54 Å and 4.78 Å, respectively, which are the second and third smallest among zinc blende III-V materials and indicates strong lattice bonding of BP and BAs [27]. The compact structure and light atomic mass of BP and BAs leads to a large overlap of atomic orbitals in the crystal, resulting in high crystal stability [28].

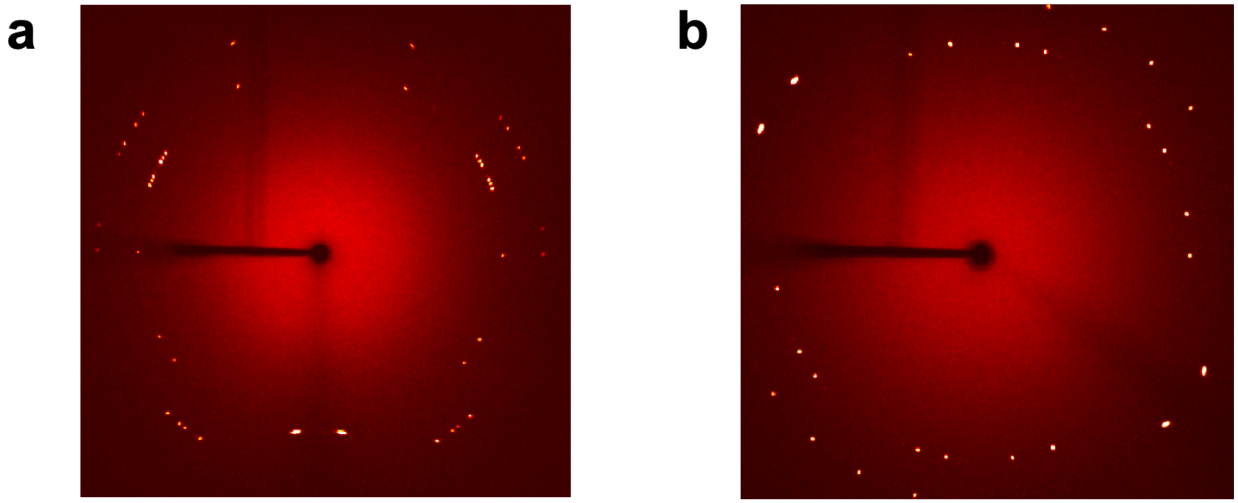

Figure 3.5 *Rotation image from single crystal XRD of (a) BP and (b) BAs*

The single crystallinity of each BP and BAs is further verified by S-XRD. It is performed using a Bruker SMART APEX II single-crystal XRD machine equipped with a charge-coupled device (CCD) detector. A single piece of BAs crystal (~50 μm size) is separated from the growth substrate and mounted onto the goniometer stage for measurement. First, the crystal quality is carefully examined by full-angle rotation images (Fig. 3.5). The samples are rotated over 360 degrees under x-ray excitation, while the diffraction data is continuously collected by the CCD detector and subsequently combined into a single plot. The combined rotation images show that the BP and BAs crystal sample was a single crystal in its entirety. For BAs, to examine the possibility of any crystal twinning and defects, S-XRD data is collected with 0.3 degree of frame width and 60s/frame of exposure time. A Mo Kα radiation source is used for data collection. Following the measurements, the Bruker APEX software is used to determine the lattice constant and crystal structure.

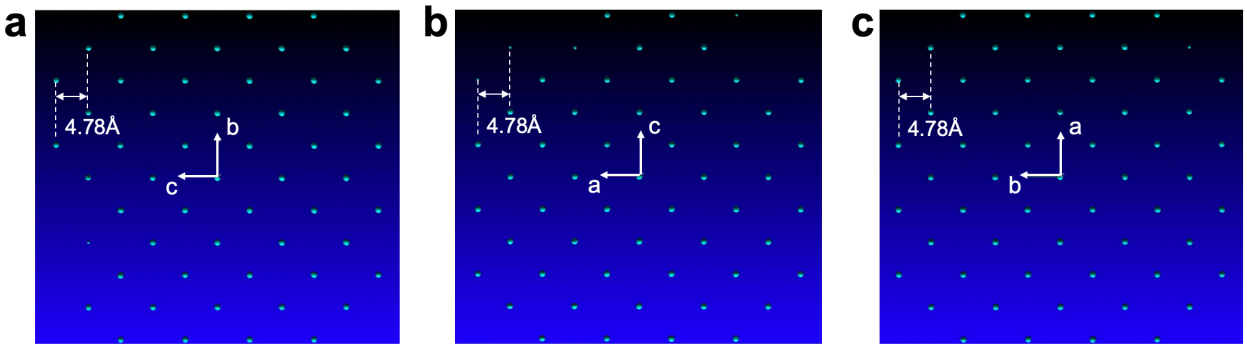

Figure 3.6 *Reconstructed reciprocal lattice space of BAs from single crystal XRD. (a) (100) plane (b) (010) plane (c) (001) plane*

The BAs crystal sample demonstrates a perfect zinc-blende FCC crystal structure with a lattice constant of 4.78Å. In combination with the measured diffraction patterns from each frame, the reciprocal lattice space (*k* space) of the BAs crystal sample is constructed and plotted (Fig. 3.6). Fig. 3.7b and 3.7c show the measured reciprocal lattice of the BAs crystal in the (001) and (010) direction, respectively. After verification of the crystallographic direction in the reciprocal lattice, we concluded that the entire BAs crystal is a homogeneous single-crystal domain without lattice twinning.

Next, we use Raman spectroscopy to further verify our crystal quality. Raman spectra were taken with a Raman microscope (inVia, Renishaw) under laser excitation at 633 nm with a 1800 /mm grating. The laser was polarized and backscattered. The Raman microscope operated with the Leica DM2500 optical system.

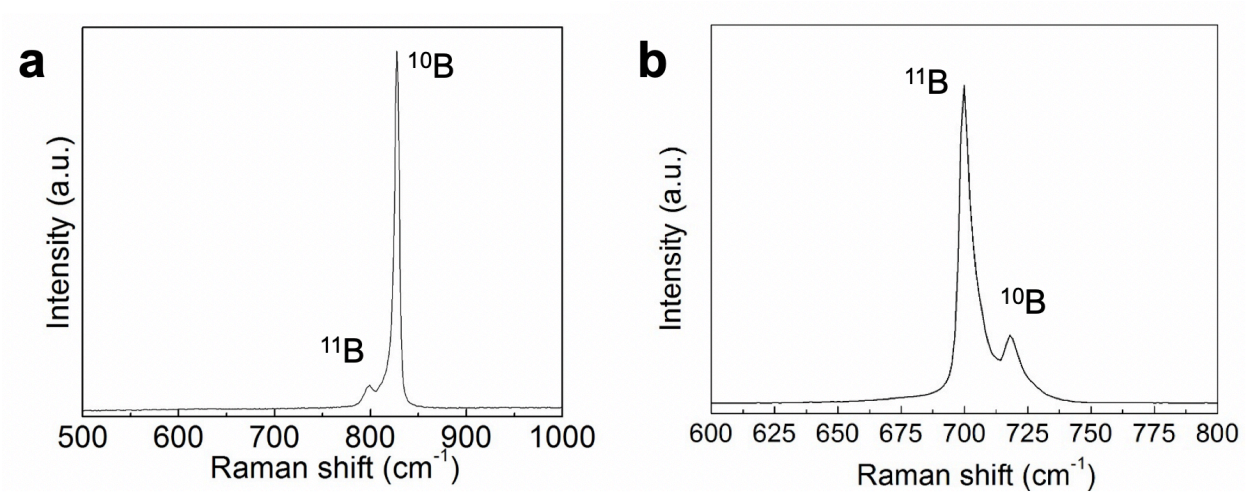

Figure 3.7 *Raman spectra of (a) BP and (b) BAs.*

Figure 3.7 shows Raman data of BP and BAs. The Raman spectroscopy data of the BP sample clearly shows the two peaks at 799 cm^{-1} and 829 cm^{-1}, corresponding to the ^{11}B and ^{10}B phonon modes respectively [29]. On the other hands, for BAs, it clearly shows two peaks, at 700 and 720cm^{-1}, corresponding to the optical branches of two boron isotopes, ^{10}B and ^{11}B, in their natural abundance, respectively. Full width half maximum of every peaks is very narrow which indicates high crystallinity of my sample. In addition, no difference has been observed for the structural characterization performed at different crystals, which indicates uniformity of grown materials.

Next, to examine atomic resolved lattice of crystal, I performed high-resolution TEM image. TEM samples were prepared by using a focused ion beam (FIB) machine (Nova 600, FEI). First, a single piece of BAs crystal was cut by FIB into small size pieces: 8 μm×8 μm×2 μm (width × height × thickness), and placed on top of a TEM grid (PELCO FIB Lift-Out, Ted Pella) with a nanomanipulator. The BAs crystal was further milled by FIB until the sample thickness was thin

enough (~ 100 nm) to be traversed by the electron beam for effective TEM imaging. Figure 3.8a shows FIB samples to ~ 100 nm for HRTEM.

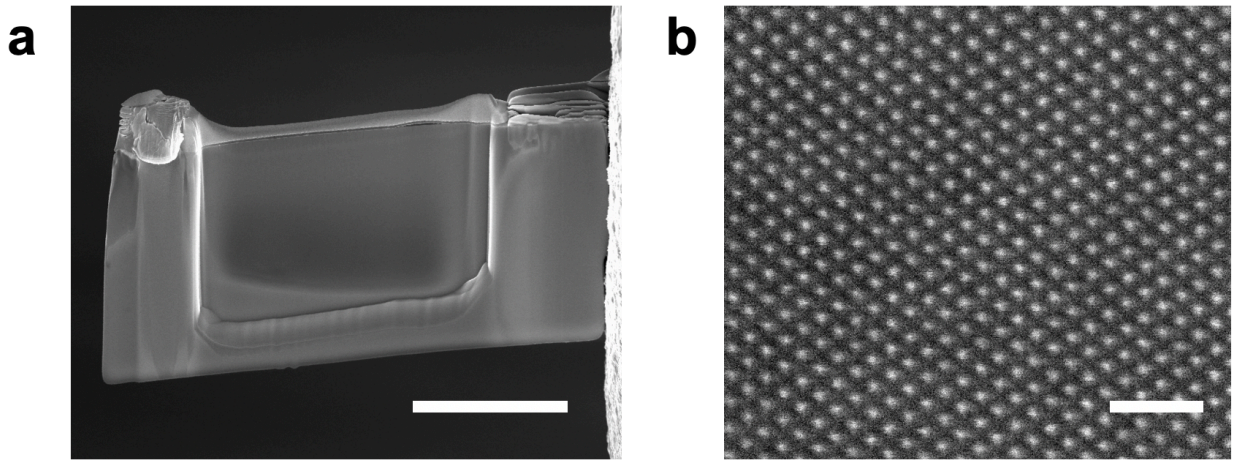

Figure 3.8 *(a) TEM sample of BAs crystal prepared by FIB technique. Scale bar is 3 μm. (b) High resolution TEM image of BAs on (110) zone axis. Scale bar is 2nm.*

After FIB, we used concentrated argon ion beam (Nanomill, model 1040, Fischeone) to clean the BAs sample surface which possibly contaminate during FIB process. After cleaning, we took the high angle annular dark field (HAADF) image by using aberration-corrected high-resolution scanning TEM (Grand ARM, JEOL, 300 kV). Atomic-resolution TEM images and their fast Fourier transform images were processed with the Gatan TEM software. Then HRTEM images (Fig. 4.6b) clearly demonstrate the atomically-resolved single-crystal lattice of our BAs sample with [110] zone axis.

3.3 Thermal and phonon transport in BP

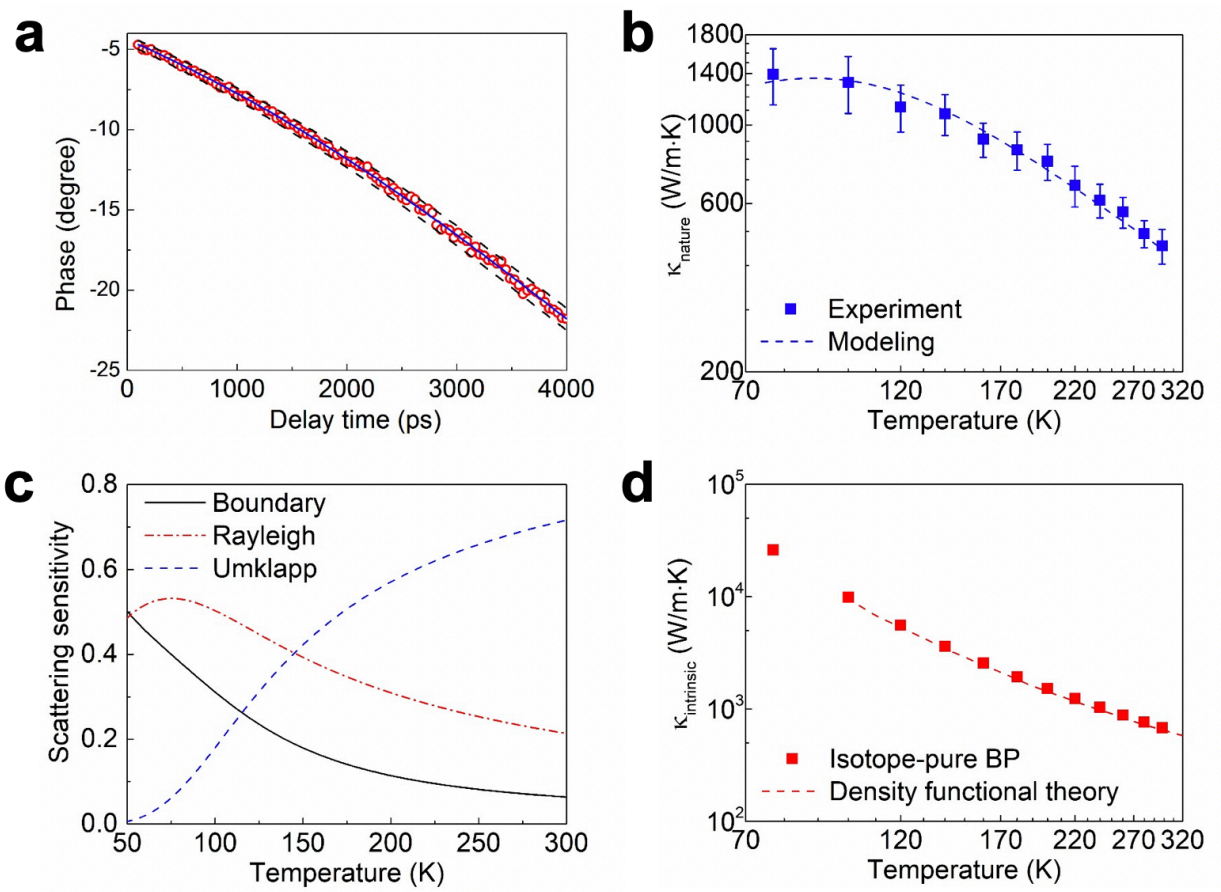

Figure 3.9. *(a) Experimental measurement data and model fitting. Experimental data (red circle) and fits from the multilayer thermal transport model (black line) for the TDTR phase signal. Calculated curves (black dashed lines) using the thermal conductivity changed by ±10% of best values are plotted to illustrate the measurement sensitivity. (bc) Experimental measurement data and modeling results of the temperature dependent thermal conductivity (κ_{nature}) from 77 to 298 K. (c) Scattering sensitivity analysis to different phonon scattering mechanisms. Experimental data (blue square) and modeling fit considering multiple phonon scattering processes (dashed blue line). (d) Temperature-dependent thermal conductivity of isotope-pure BP ($\kappa_{intrinsic}$) extracted from experiment (red square) in comparison with density functional theory (DFT) calculation*[17] *(red dashed line).*

The thermal properties of single crystal BP was characterized using a time-domain thermoreflectance (TDTR) method. The experimental data from our TDTR measurement and fittings are shown in Figure 3.9a. The thermal conductivity of BP at room temperature is measured and reported here to be a record high of~ 460 W/m·K. This value is exceeding that of common highly conductive metals such as copper and three times higher than single crystal Si, which indicates that BP is promising for high thermal conductivity applications.

To investigate the high thermal conductivity transport mechanisms of BP, temperature-dependent thermal conductivity (κ_{nature}) of our BP sample is measured from 77 K to 298 K (Figure 3.9b). Following the general temperature-dependent trend of single crystals, thermal conductivity of BP increases with reduced temperature non-linearly due to the suppression of phonon scattering.

At 77 K, the measured thermal conductivity of our sample reaches a high value of ~ 1400 W/m·K. This temperature-dependent data is directly related to phonon scattering mechanisms. Fundamentally, the lattice thermal conductivity by kinetic theory[15] is expressed by

$$\kappa = \frac{1}{3}\sum_{p}\int C(\omega,p)v_g(\omega,p)\Lambda(\omega,p)\,d\omega \qquad (3\text{-}1)$$

where $C(\omega, p)$ and $v_g(\omega, p)$ are spectral volumetric specific heat and group velocity respectively for the phonon mode with frequency ω and polarization p. Phonon mean free path (MFP), $\Lambda(\omega, p) = v_g(\omega, p)\cdot \tau(\omega, p)$, describes the average distance that phonon travels between two successive scattering. The total phonon relaxation time $\tau(\omega, p)$ is contributed by Rayleigh scattering (τ_r) from impurities or isotopes, Umklapp scattering (τ_a) from anharmonic phonon-phonon scattering, and boundary scattering (τ_b), following the Matthiessen rule [30],

$$\frac{1}{\tau} = \frac{1}{\tau_U} + \frac{1}{\tau_{ph-e}} + \frac{1}{\tau_M} + \frac{1}{\tau_B} \qquad (3\text{-}2)$$

Importantly, the temperature and frequency dependence varies for different scattering contributions [31]:

$$\tau_M^{-1} = A\omega^4 \qquad (3\text{-}3)$$

$$\tau_B^{-1} = \frac{v_s}{L} \qquad (3\text{-}4)$$

where v_s is sound velocity and L is crystal size. The Umklapp scattering follows the modified Callaway's model [32–34] as,

$$\tau_U^{-1} = BT\omega^2 \exp(-C_u / T) \qquad (3\text{-}5)$$

The temperature-dependent experimental data can be fitted well using the above phonon relaxation time model, where A, B, and C_u are the respective coefficient. Both experimental and modeling data are plotted in Figure 3.9b. To identify the dominant phonon scattering mechanism in BP, we analyze the sensitivity of thermal conductivity to each scattering contribution, and define the respective scattering sensitivity as

$$S_i = -\frac{d \ln \kappa}{d \ln \tau_i^{-1}} \qquad (3\text{-}6)$$

where τ_i^{-1} is one phonon scattering rate as defined in equations (3-2)-(3-5). The scattering sensitivity analysis in Figure 3.9c shows that τ_r affects κ most strongly at low temperature (77 K) while τ_a plays the most significant role at high temperature (300 K). This result is consistent with our physical understanding of different scattering mechanisms: phonons with long MFP at low temperature are prone to be scattered due to impurities or limited crystal size; Umklapp scattering becomes more dominant with increasing temperature. Based on our measurement, we

derive the limit for intrinsic thermal conductivity of isotope-pure BP ($\kappa_{intrinsic}$) by only considering Umklapp scattering and eliminating the impurity/isotope scattering. Interestingly, the measured temperature-dependent thermal conductivity of isotope-pure BP shows very good agreement with the recent calculation using density functional theory (DFT) (Fig. 3.9d) [35]. At 77 K, $\kappa_{intrinsic}$ reaches a very high value of 26061 W/m·K for isotope-pure BP (versus 1400 W/m·K for κ_{nature}), which verifies the presence of very strong Rayleigh scattering from isotope impurities at low temperature.

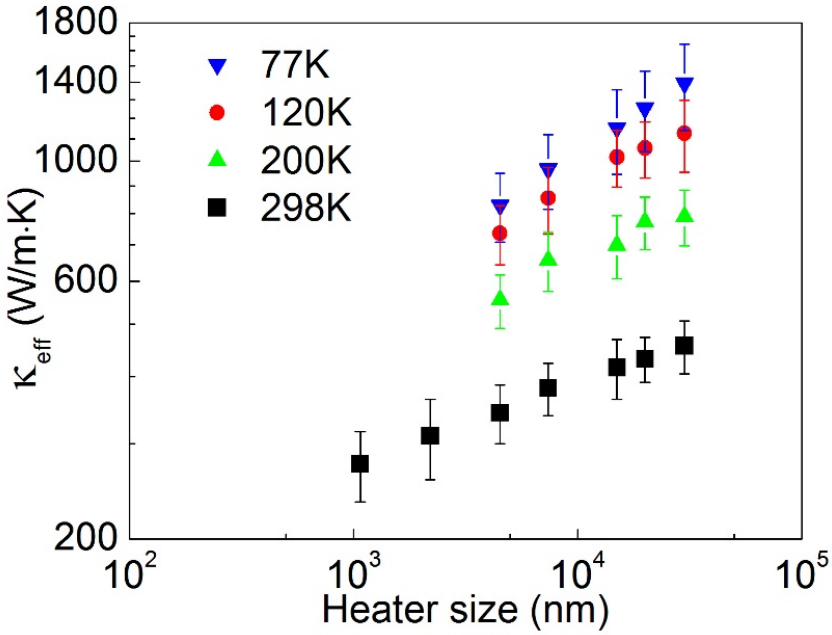

Figure 3.10 *Experimental study of ballistic phonon transport by measuring size-dependent effective thermal conductivity (κ_{eff}) at different temperatures.*

To quantify the spectral contribution to thermal conductivity of BP from different phonon modes, we measured size-dependent thermal conductivity by probing nanoscale quasi-ballistic

transport. Our experiment was designed following a similar approach that has been described in the recent work [36]. The effective heating size (D) on BP sample is controlled by varying the laser spot size, which determines a characteristic thermal length to control the heat transfer regime. In the diffusive limit, i.e., when D is larger than phonon mean free paths (Λ) of all the phonon modes, the measured thermal conductivity approaches the bulk value (κ_{bulk}) since all propagating phonons experience enough scattering to reach local thermal equilibrium and the transport can be accurately described using Fourier's law. However, as D is reduced, those phonons with $\Lambda(\omega, p) > D$ will not have enough chances to scatter and thus experience ballistic thermal transport, analogously to thermal radiation. Importantly, the heat flux for the ballistic transport is suppressed from that for the diffusive transport, and the deviations provide information about the contribution to thermal conductivity from MFPs of different phonons. The key metric to evaluate ballistic phonon transport and spectral contribution to thermal conductivity is the effective thermal conductivity (κ_{eff}), which is defined following Fourier's law. For smaller heater size (D), or increased phonon MFP (Λ) at lower temperature, a high portion of phonons will have $\Lambda > D$ and experience ballistic transport, therefore leading to a gradual reduction in κ_{eff} [36,37]. Experimentally, κ_{eff} of BP is measured as a function of heater sizes at variable temperatures (Figure 3.10). Ballistic transport can be clearly observed in the size-dependent measurement. For example, from D = 30 μm to 4.5 μm, κ_{eff} reduces by 24% at 298 K while by 42% at 77 K.

To quantify the spectral contribution to thermal conductivity of BP from different phonon modes, we measured size-dependent thermal conductivity by probing nanoscale quasi-ballistic transport. Our experiment was designed following a similar approach that has been described in the recent work[36]. The effective heating size (D) on BP sample is controlled by varying the laser spot size, which determines a characteristic thermal length to control the heat transfer regime. In

the diffusive limit, i.e., when D is larger than phonon mean free paths (Λ) of all the phonon modes, the measured thermal conductivity approaches the bulk value (κ_{bulk}) since all propagating phonons experience enough scattering to reach local thermal equilibrium and the transport can be accurately described using Fourier's law. However, as D is reduced, those phonons with $\Lambda(\omega, p) > D$ will not have enough chances to scatter and thus experience ballistic thermal transport, analogously to thermal radiation. Importantly, the heat flux for the ballistic transport is suppressed from that for the diffusive transport, and the deviations provide information about the contribution to thermal conductivity from MFPs of different phonons. The key metric to evaluate ballistic phonon transport and spectral contribution to thermal conductivity is the effective thermal conductivity (κ_{eff}), which is defined following Fourier's law. For smaller heater size (D), or increased phonon MFP (Λ) at lower temperature, a high portion of phonons will have $\Lambda > D$ and experience ballistic transport, therefore leading to a gradual reduction in κ_{eff} [36,37]. Experimentally, κ_{eff} of BP is measured as a function of heater sizes at variable temperatures (Figure 3.10). Ballistic transport can be clearly observed in the size-dependent measurement. For example, from D = 30 μm to 4.5 μm, κ_{eff} reduces by 24% at 298 K while by 42% at 77 K.

To quantitatively understand the ballistic phonon transport in BP and interpret the experiment result, we solve three-dimensional spectral-dependent phonon Boltzmann transport equation (BTE) with relaxation time approximation as given by

$$\frac{\partial f}{\partial t} + v_g \cdot \nabla f = -\frac{f - f_0}{\tau} \qquad (3\text{-}7)$$

Where f is phonon distribution function, and f_0 is the equilibrium Bose-Einstein distribution at local temperature. However, it should be noted that it is challenging to solve three dimensional (3D) spectral-dependent BTE, especially using deterministic methods.

To solve BTE for the 3D practical experimental geometry, we calculate the spectral-dependent phonon BTE in the experimental geometry using Monte Carlo method. In the Monte Carlo simulation, a large number of phonon bundles are computed to get a converged result. Each phonon bundle is processed independently, following an "advection – sampling – internal scattering" process repeatedly until reaching a given simulation time. In advection procedure, the phonon bundle is moved under group velocity without internal scattering. In sampling procedure, the phonon bundle energy at a certain position is counted. In internal scattering procedure, the phonon bundle frequency is randomly redistributed. For conventional Monte Carlo simulation, there have been several limitations.

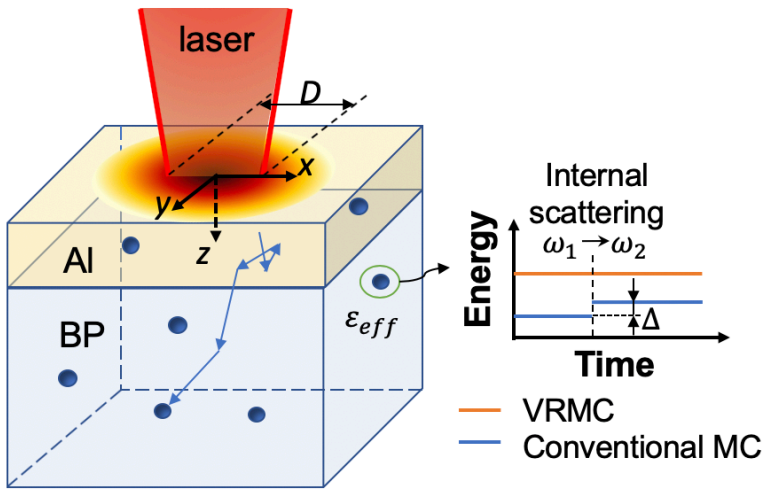

Figure 3.11. *Schematic of the simulation domain representing the practical experimental geometry. Inset schematic illustrates the comparison between conventional Monte Carlo and VRMC.* ε_{eff} *is the effective energy of the phonon bundles.*

First, as illustrated in the inset of Figure 3.11, rigorous energy conservation during phonon internal scattering is challenging for conventional Monte Carlo simulation, which conserves the energy by artificially adding or deleting phonon particles until the energy before

and after scattering matches within a certain tolerance[38]. However, this method cannot rigidly conserve energy, and may cause error in some cases. Second, conventional Monte Carlo method is time-consuming in the situation of small temperature difference, due to the higher requirement for accuracy. Generally, a large quantity of phonon bundles is needed to meet the computational accuracy and ensure uncertainties to be smaller than the finite temperature difference, hence requiring a high computational cost. Third, the computational cost can be further increased due to the required sampling of temperature field during Monte Carlo simulation. Since the local pseudo-temperature is needed to determine the local equilibrium Bose-Einstein distribution, mesh size and time step are required for the updating of temperature field, which may also lower the accuracy if the mesh size and time step are not small enough.

To enhance the computational accuracy and speed, we performed a simulation based on a recently developed variance-reduced Monte Carlo (VRMC) method[39,40]. In the VRMC method, the required convergence time is greatly reduced, and the errors introduced by internal scattering can be avoided[39–41]. Especially for the situations of small temperature difference, which is inevitable in TDTR measurement, the enhanced requirements for computational accuracy at small temperature difference can be easily satisfied without greatly increasing the computation time. The VRMC method solves the deviational energy based BTE as given by

$$\frac{\partial e^*}{\partial t} + v_g \cdot \nabla e^* = -\frac{e^* - e_0^*}{\tau} \qquad (3\text{-}8)$$

where $e^* = e - e_{T_{eq}}^{eq} = \hbar\omega(f - f_{T_{eq}}^{eq})$ is the deviational energy distribution, and $e_0^* = e^{loc} - e_{T_{eq}}^{eq} = \hbar\omega(f_{T_{loc}}^{eq} - f_{T_{eq}}^{eq})$ is the equilibrium deviational energy distribution at local temperature. $\hbar\omega$ is the energy of a single phonon with frequency ω. f is the actual phonon

distribution function, and $f_{T_{eq}}^{eq}$ is the Bose-Einstein distribution function at equilibrium temperature T_{eq} = 300K.

The three challenges in conventional Monte Carlo are solved in VRMC. First, as we are calculating the deviational energy distribution e^*, instead of the distribution function f, the energy carried by each phonon bundle is independent from the phonon frequency. Thus, the energy conservation can be rigorously guaranteed during internal scattering[39], as shown in the inset of Fig 3.11. By rigorously following energy conservation during internal scattering, we avoid the uncertain small energy difference before and after internal scattering, and consequently enhance the accuracy. For VRMC, there is no need to add or delete phonons in the cell to conserve energy. Second, we only consider the deviational energy from equilibrium state, which reduces the convergence time, especially for a small temperature difference situation. In this method, the equilibrium energy is determined deterministically, and only the deviational energy is determined stochastically. The deviational energy is much smaller than the equilibrium energy, especially in small temperature difference situation. Given that only a small term for deviational energy is determined stochastically, the absolute statistical uncertainty is dramatically decreased, so the required convergence time is greatly reduced[42]. Third, by linearization of the scattering term, each phonon bundles can be simulated independently without sampling local pseudo-temperature, and the algorithm requires no integration time step and computational cells[40]. Since we don't need to do sampling on the temperature field, the computational speed is faster. Furthermore, because our simulation does not have mesh and time step, the mesh/time step-induced inaccuracy is eliminated.

The phonon relaxation time for BP optical branches and aluminum is taken as 10 ps. To be consistent with TDTR experiment, the simulation is performed in the same geometric domain

as the experimental condition with time range from 0 to 6 ns. The thickness of the BP is considered as infinite given the sample thickness is much larger than the thermal penetration depth in the transient measurement. The initial temperature distribution in Al film follows the Gaussian distribution $\Delta T = \exp(-2r^2/r_l^2)$, where r_l is the pump beam radius, and $D = 2r_l$ is the pump beam diameter. The temperature in BP is initialized at 300 K. During initialization, phonon bundles are distributed uniformly in a region with a radius of $2r_l$ in Al film, but with different effective energy based on local initial temperature. The top surface of Al film is treated as diffusive adiabatic boundary. Once the phonon touches the diffusive adiabatic boundary, it will be reflected with randomly redistributed direction but unchanged frequency and energy. At the Al-BP interface, the phonon has a probability to be diffusively reflected by or transmitted through the interface and the thermal conductance at the Al-BP interface was set to be consistent with experimental value: for example, $1.2 \times 10^8\ \mathrm{W/(m^2 \cdot K)}$ at 298 K. To calculate the surface temperature as a function of time, a sampling region was defined as $\{(r, z) | r \leq r_l, z \leq 5\ \mathrm{nm}\}$ to represent Al surface. The average phonon energy density of sampling region was counted with time goes on, and then converted into temperature.

To extract the BP thermal conductivity from VRMC result, a Fourier's model treating BP thermal conductivity as a fitting parameter was developed in COMSOL Multiphysics to fit the VRMC result. The initial condition and sampling region of Fourier's model are the same as the VRMC model. The data picked up for fitting are in the time range of 1 ~ 6 ns, and normalized based on the surface temperature at 900 ps.

The time-averaged spectral-dependent flux can be obtained by VRMC. The time-averaged flux contributed by a single phonon bundle during the whole simulation time can be expressed as

$$f = \frac{\varepsilon \sum_{i=1}^{N} \hat{s}_i L_i}{\sum_{i=1}^{N} \tau_i} \qquad (3\text{-}9)$$

where ε is the effective energy carried by this phonon bundle, L_i and τ_i are distance and time between two successive scattering events in advection procedure i, and $\hat{s}_i$ is the unit direction vector. If the total simulation time for each phonon bundles are the same, we have $f \propto \varepsilon \sum_{i=1}^{N} \hat{s}_i L_i$. So the cross-plane and in-plane flux contributed by a single phonon bundle during one advection procedure are εL_z and εL_r respectively, where L_z and L_r are projection of L_i to axial and radial direction, respectively. During each internal scattering event, the mode of the phonon bundle could be changed. We add the flux contribution to the corresponding phonon mode after each advection step to obtain the spectral-dependent flux. In the end, we normalized the spectral-dependent flux by the phonon mode with smallest MFP which is at the cut-off frequency, since we assume the phonon mode with smallest MFP is not suppressed. To avoid the influence from the interface dispersion mismatch, we start to count the phonon bundles after their emission from the interface into the BP.

Sampling local pseudotemperature is not required, each phonon bundles can be simulated independently, and the algorithm requires no integration timestep and computational cells[40]. During the internal scattering process, the phonon frequencies are redistributed randomly, following the equilibrium distribution $\frac{D(\omega,p)}{\tau(\omega,p,T_{eq})} e_0^* = \frac{D(\omega,p)}{\tau(\omega,p,T_{eq})} \left(e_{T_{loc}}^{loc} - e_{T_{eq}}^{eq} \right)$, so local pseudotemperature T_{loc} is required in order to get $e_{T_{loc}}^{loc}$. But the e_0^* in equation (3-9) can be linearized as $e_0^* = e^{loc} - e_{T_{eq}}^{eq} \approx (T_{loc} - T_{eq}) \frac{\mathrm{d}e_{T_{eq}}^{eq}}{\mathrm{d}T}$. As $(T_{loc} - T_{eq})$ does not influence the distribution, the phonon bundles can be redistributed based on the distribution $\frac{D(\omega,p)}{\tau(\omega,p,T_{eq})} \frac{\mathrm{d}e_{T_{eq}}^{eq}}{\mathrm{d}T}$, without sampling local pseudotemperature.

To clarify the understanding for anisotropic suppression of the thermal conductivity[43–45] due to quasi-ballistic phonon transport, we develop detailed phonon spectral flux calculations to analyze the anisotropic heat transfer. We perform phonon spectral dependent simulations to calculate the in-plane and cross-plane heat flux in BP crystal at different heater sizes. The simulation geometry for phonon BTE is the same as the experimental condition, in which an Al transducer film on top of the BP is heated up by laser with circular and Gaussian distributed temperature profile as shown in Fig 3.11. During one advection step, the heat flux along a certain direction contributed by a single phonon bundle is proportional to the product of the effective energy of the phonon bundle and the phonon displacement along that direction[40,44]. By cumulating the heat flux contributed by each phonon bundle to the corresponding phonon mode, the heat flux contribution from each phonon mode can be obtained.

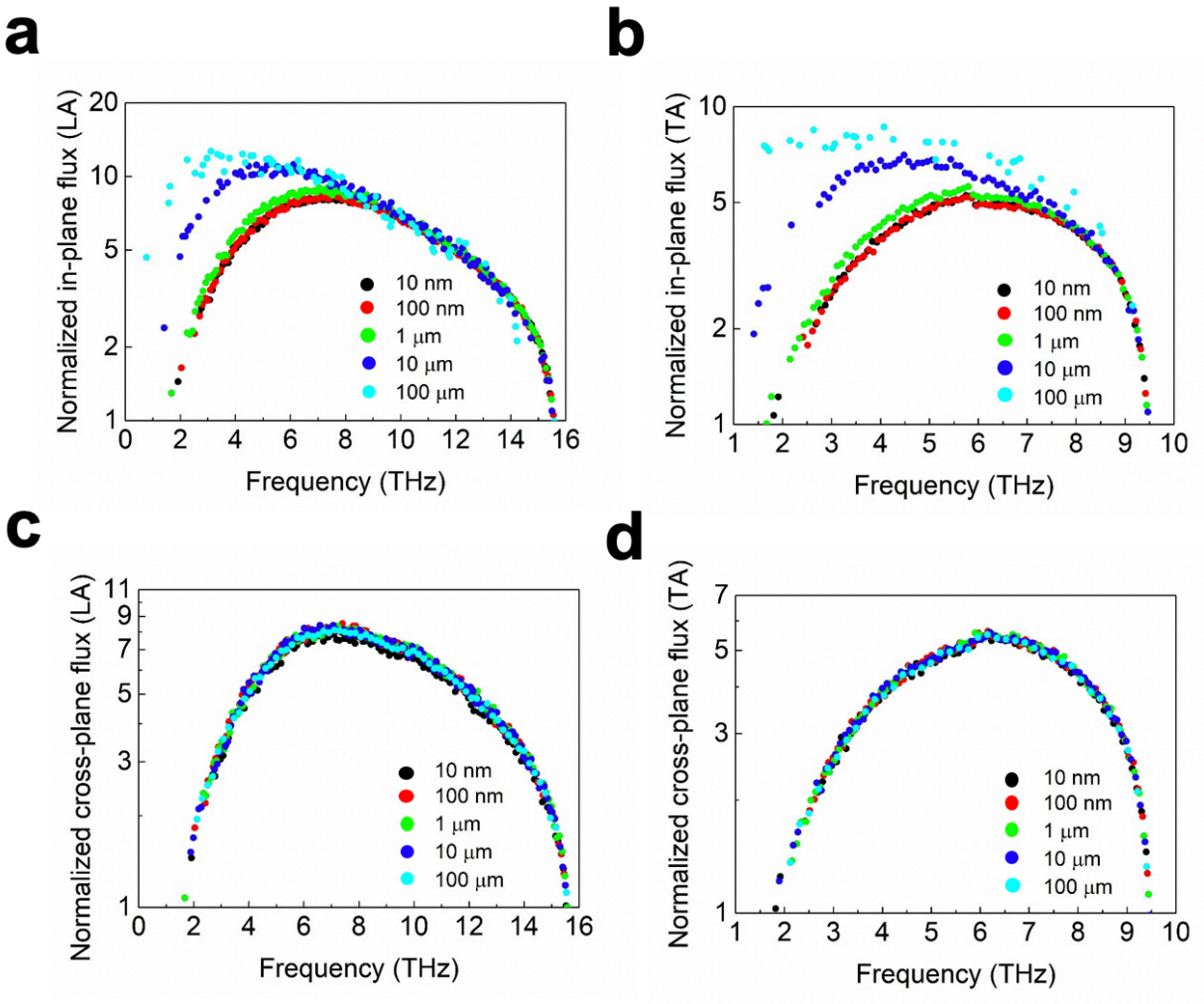

Figure 3.12 *Spectral heat flux contributed from the longitudinal acoustic (LA) and transverse acoustic (TA) phonon modes respectively are calculated in in-plane and cross-plane directions and different heater sizes. (a) LA in-plane. (b) TA in-plane. (c) LA cross-plane. (d) LA cross-plane.*

Figure 3.12 show the normalized spectral in-plane and cross-plane heat flux for longitudinal acoustic (LA) and transverse acoustic (TA) phonon polarization. The spectral heat flux in each polarization is normalized by the phonon mode with the smallest MFP, given that the phonon mode with the smallest MFP at the Brillouin zone edge is not suppressed by size confinement. In Fig 3.12a and 3.12b, both polarizations show that normalized spectral in-plane

heat flux is lower when heater size is smaller, which reveals the heat flux reduction due to size effect. In particular, the low frequency phonons with long MFPs usually get a large suppression. It is important to note that the in-plane spectral heat flux in Fig 3.12a and 3.12b shows strong dependence on the heater size, while the cross-plane spectral heat flux in Fig 3.12c and 3.12d is independent on heater size. Our detailed phonon spectral flux calculation conclusively shows that the experimentally measured size-dependent thermal conductivity mainly comes from the in-plane confinement of phonon transport, i.e., lateral ballistic thermal transport takes place for phonon modes with $\Lambda > D$, while the cross-plane heat transfer is not suppressed. The conclusion on the anisotropic suppression of thermal conductivity in TDTR measurement from our work is consistent with recent studies[43,44].

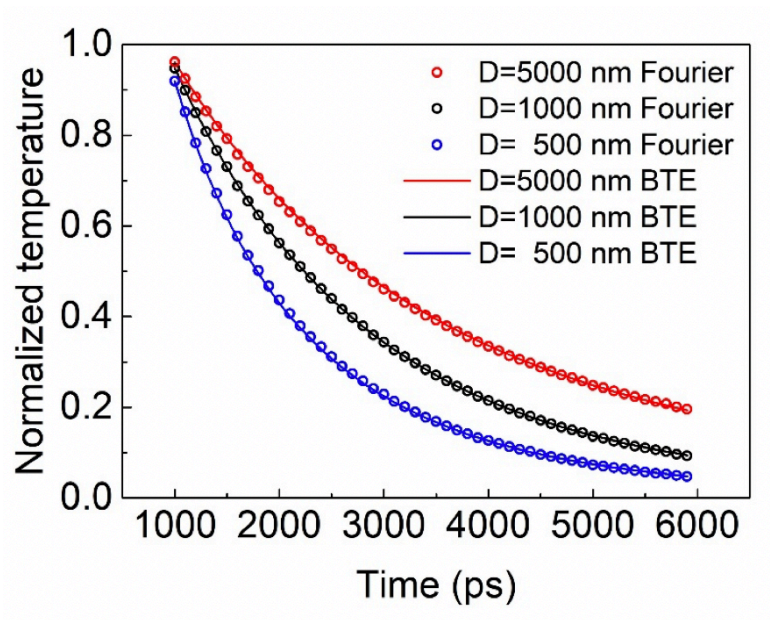

Figure 3.13. *Examples of fitting the effective thermal conductivity by matching the temperature decay curve calculated from the BTE to the Fourier solution at different heater sizes.*

To make a direct comparison of the experimental TDTR data with the multi-scale simulation results calculated by BTE and VRMC, size-dependent effective thermal conductivity

was extracted by matching the temperature decay curve calculated from the BTE and VRMC results to the Fourier solution. Figure 3.13 shows that the examples of VRMC data and fitting curves for different heater sizes. The surface temperature decays faster at smaller beam diameter even though the effective thermal conductivity is smaller, because the larger surface-to-volume ratio of the heater at a small beam diameter increases the heat dissipation efficiency.

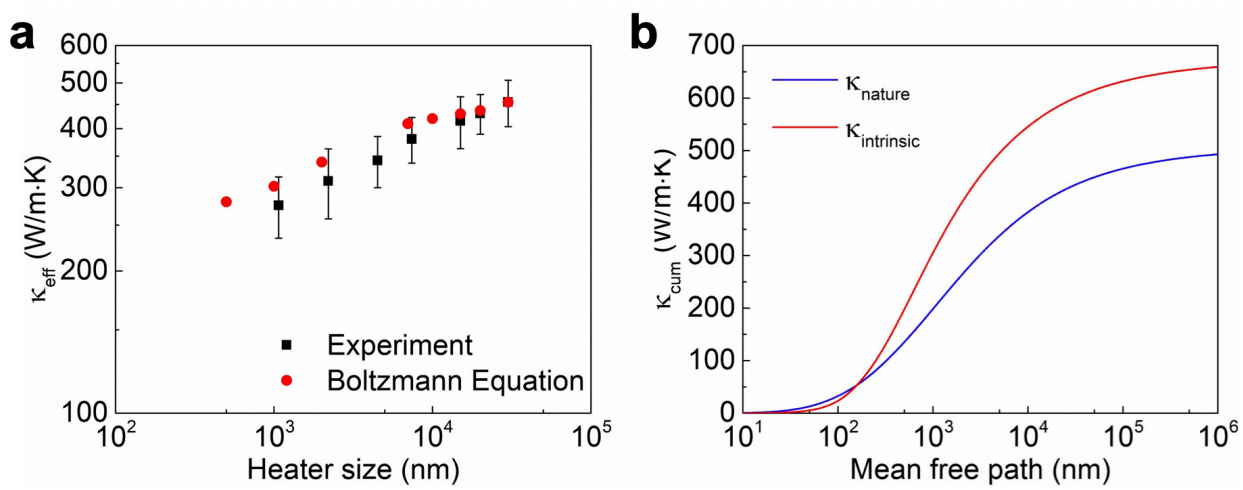

Figure 3.14. *Experimental-modeling synergy to quantify the ballistic thermal transport and to develop the phonon mean free path spectra. (a) Comparison of the size-dependent effective thermal conductivity (κ_{eff}) from the Boltzmann equation prediction (red circle) and experimental measurement (black square). (b) Constructed phonon mean free path spectra from the measurement: cumulative thermal conductivity (κ_{cum}) is plot versus phonon mean free path for both natural-abundance ($\kappa_{nature,}$ blue line) and isotope-pure BP ($\kappa_{intrinsic,}$ red line).*

The VRMC and BTE calculated results are plotted together with TDTR experiment in Figure 3.14a, showing a good agreement. This study provides a quantitative analysis based on the BP phonon spectra and shows that the failure of Fourier's law in the ballistic regime is due to in-plane size confinement.

As a further step, based on our measurement, we construct the phonon MFP spectra of BP with both natural abundant (κ_{nature}) and pure isotope ($\kappa_{intrinsic}$), shown in Figure 3.14b. The phonon MFP spectra is quantified by the cumulative lattice thermal conductivity[34,46], κ_{cum}, which is defined as the total contribution to thermal conductivity from phonon modes with MFP up to a certain value Λ′,

$$\kappa_{cum}(\Lambda') = \frac{1}{3}\sum_{p}\int_{0}^{\Lambda'} C(\omega,p)v_g(\omega,p)\Lambda(\omega,p)\,d\omega \qquad (3\text{-}10)$$

Without isotope or impurity scattering, the intrinsic bulk thermal conductivity of BP goes up to 681 W/m·K. Interestingly, a cross-over between κ_{nature} and $\kappa_{intrinsic}$ is observed for MFP around 100 nm: i.e. $\kappa_{intrinsic}$ is smaller than κ_{nature} for small MFPs, whereas $\kappa_{intrinsic}$ is larger than κ_{nature} for large MFPs. Such observation is consistent with our previous measurement on the phonon MFP spectra of silicon and $Si_{0.992}Ge_{0.008}$ alloy[36], and we attribute it to the fact that Rayleigh scattering caused by impurities or isotopes strongly affects high frequency phonons and further reduces the MFPs of these high frequency phonons to even smaller values, thereby increasing the contribution from phonon modes with very small MFPs to thermal conductivity. The measured MFP spectra projects the phonon spectral contributions of the thermal conductivity into characteristic length scales, and is very useful for the direct prediction of thermal transport in more complex nanostructured materials and devices[36] and develop rational control of thermal properties.

3.4 Thermal and phonon transport in BAs

We measure thermal conductivity of BAs by using TDTR. The limited size of our crystals makes TDTR well suited for the study as no physical contact is required with the sample

and the measurement can provide high spatial resolution down to micrometer. The thermal conductivity is obtained by fitting the full transient decay curve, acquired by varying the time delay, to a thermal model (Fig. 3.13a). We measured a room-temperature thermal conductivity of our high-quality BAs crystals of ~ 1300 W/mK. This value, exceeds that of any known metals and semiconductors, and is more than three times higher than that of industrial standards (copper and silicon carbide).

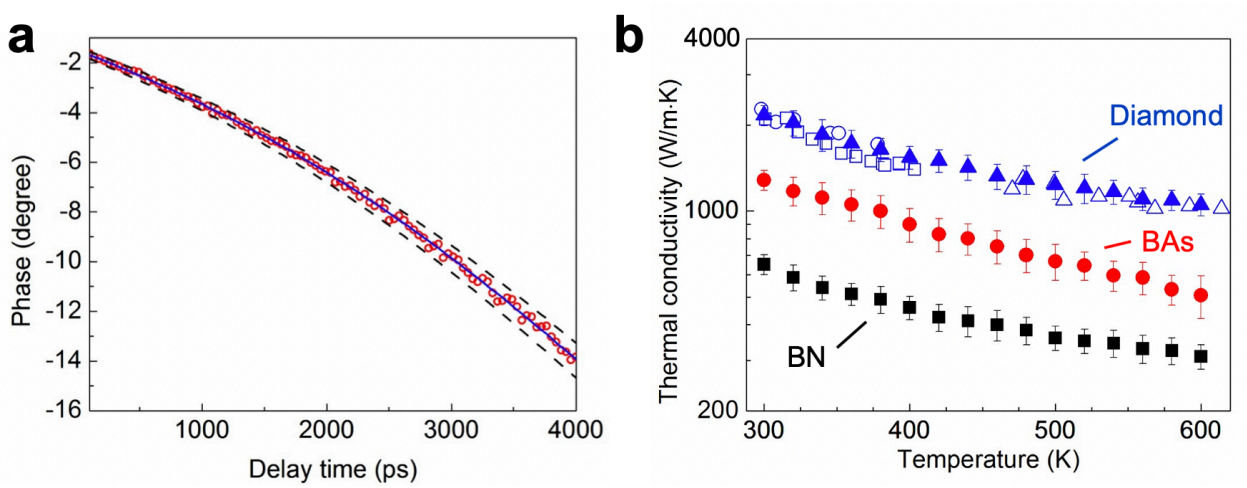

***Figure 3.15**. Thermal conductivity measurement of BAs. (a) TDTR raw data of BAs sample. Red open circle is experimental data. Solid blue line is best fit with experimental data. Black dash lines are +10% and -10% thermal conductivity fitting. b) Temperature-dependent (300 to 600 K) thermal conductivity of the three materials with the highest thermal conductivities: diamond, BAs, and boron nitride (BN). Black squares, red circles and blue triangles indicate cubic BN, BAs, and diamond, respectively. Also shown are literature data for diamond [open blue circles[47], squares[48], and triangles[49]].*

We simultaneously performed TDTR measurements on single-crystal BAs, diamond, and cubic boron nitride (BN) samples to ensure accuracy and provide direct comparison between the materials. BAs samples were loaded together with single-crystal cubic boron nitride (BN) and

diamond samples (from Element Six) into a cryostat (Janis ST-100 Optical Cryostat, from 4 to 800K) with a precise proportional-integral-derivative (PID) temperature controller (Lakeshore Model 335). Simultaneous thermal conductivity measurements on the three materials with the highest thermal conductivity, i.e. BAs, diamond, and BN, were performed with the TDTR technique to guarantee measurement accuracy for high conducting materials, and enable direct comparisons between them to understand the phonon physics. For each measurement temperature, once the set temperature was reached, an additional waiting time of over 30 minutes was added before the actual thermal measurement was performed to ensure that the samples had reached a complete thermal equilibrium and steady temperature.

The temperature-dependent thermal conductivities of these samples from 300 to 600 K are shown in Fig. 3.15b. Our thermal conductivity values for diamond (from 2200 to 1050 W/mK) are consistent with values from the literature[47–49] and validate our approach. All samples had decreased thermal conductivities with increased temperature, indicating Umklapp scattering due to increasing phonon population. This also indicates a high single-crystal quality with a minimum number of defects. The thermal conductivity of BAs is almost twice that of cubic BN, making BAs the second highest thermal conducting material among all known bulk materials. BAs has a high potential for manufacturing integration being a semiconductor and holds promise for thermal management applications.

Fundamentally, thermal transport in solids can be described by the interactions of phonons, i.e., the quantum mechanical modes of lattice vibrations[15]. Thermal conductivity results from phonon scattering processes that are closely related to the structure of materials. Previous research indicates that the last two terms of in equation (3-2)—τ_r and τ_b, play important roles in the thermal conductivity of crystals with defects and grain boundaries[50]. Importantly, the first

term of the equation (3-2), τ_U, describes the thermal conductivity of perfect single crystals without any defects, and therefore is expected to be the dominant transport mechanism in our high-quality BAs single crystals. However, a persistent fundamental question regarding the high-order phonon anharmonicity, in particular for BAs, remains in the field of atomistic phonon theory. For many decades, thermal transport in solids was considered to be governed by the three-phonon scattering process[15,51], and the effects of four-phonon and higher-order scattering processes were believed to be negligible, since they have a low probability to establish scattering configurations. The three-phonon scattering was deployed in the initial ab initio calculations of the BAs thermal conductivity[17], but according to recent theory[25,52], the four-phonon scattering is important in novel materials such as BAs. The two density functional theories (DFT) predict different thermal conductivity values for BAs. We compared our experimental measurements at different temperatures with two DFT theory predictions (Fig. 3.16). In addition, to compare and exclude the effect of point defects, we performed three-phonon DFT calculation with vacancies and included it in the figure.

To obtain temperature dependent thermal conductivity of BAs with defects, ab initio calculation is performed to consider the effect of arsenic vacancy defects at different temperatures (*T)*, following the settings in recent literature[17,35,50]. The nonequilibrium phonon distribution function n_λ under an applied temperature gradient can be described by the Boltzmann transport equation (BTE) as

$$\mathbf{v}_\lambda \cdot \nabla T \frac{\partial n_\lambda}{\partial T} = \left(\frac{\partial n_\lambda}{\partial t}\right)_{collisions} \quad (3\text{-}11)$$

where $\lambda \equiv (\mathbf{q}, p)$ labels the phonon mode with wave vector $\mathbf{q}$ and polarization p, and $\mathbf{v}_\lambda$ is the phonon group velocity. In equation (3-11), the phonon drift due to temperature gradient on the left side is balanced by the phonon scattering on the right side. The scattering term on the right

side of the equation includes intrinsic phonon-phonon scattering and phonon-isotope/defect scattering,

$$\left(\frac{\partial n_\lambda}{\partial t}\right)_{collisions} = \left(\frac{\partial n_\lambda}{\partial t}\right)_{intrinsic} + \left(\frac{\partial n_\lambda}{\partial t}\right)_{defect} \quad (3\text{-}12)$$

For phonon scattering due to isotopes or point defects, a perturbation to Hamiltonian due to mass disorder is considered. Using Fermi's golden rule, the phonon-isotope/defect scattering term[53] in BTE is expressed as

$$\left(\frac{\partial n_\lambda}{\partial t}\right)_{defect} = \frac{\pi}{2N}\omega_\lambda^2 \sum_{\lambda'} \delta(\omega_\lambda - \omega_{\lambda'}) \sum_b g(b) |\mathbf{e}_{\lambda'}^*(b) \cdot \mathbf{e}_\lambda(b)|^2 \left[n_\lambda(n_{\lambda'}+1) - n_{\lambda'}(n_\lambda+1)\right] \quad (3\text{-}13)$$

where ω_λ is the angular frequency of phonon mode λ, $\mathbf{e}_\lambda(b)$ is the vibrational eigenvector of the bth atom in unit cell and phonon mode λ, and N is the number of unit cells in the crystal. $g(b)$ is a factor that describes the mass variance of the bth atom in unit cell,

$$g(b) = \sum_i f_i(b) \left[1 - \frac{M_i(b)}{\bar{M}(b)}\right]^2 \quad (3\text{-}14)$$

where $f_i(b)$ and $M_i(b)$ are the fraction and the atomic mass of the ith isotope of the bth atom, and $\bar{M}(b)$ is the average atomic mass of the element of the bth atom. Arsenic vacancies are treated as an isotope to arsenic with zero mass. In this method, the changes of interatomic potential are ignored, whose influence to lattice thermal conductivity is negligible at low vacancy concentration (< 0.01%) (32). For the calculation of Figure 3.16 in this paper, we used a vacancy concentration ~ 0.002% to match the calculated thermal conductivity with the measured value at room temperature. The calculated curve (green dashed line, Figure 3.16) represents the prediction of temperature-dependent thermal conductivity when three-phonon process and defect scattering dominate the thermal transport (i.e. four-phonon process is negligible).

According to Eq. (3-13), the isotope scattering term is determined by nonequilibrium phonon distribution function n_λ. Similarly, using Fermi's golden rule, phonon-phonon intrinsic

scattering term considering three-phonon process can be expressed as a function of nonequilibrium phonon distribution function and third-order interatomic force constants[20,54]. Hence, the unknown n_λ is on both sides of the BTE. To calculate the thermal conductivity of most common materials, a single mode relaxation time approximation (RTA) is usually applied to derive the phonon lifetime time, and subsequently the thermal conductivity can be derived from kinetic theory[15]. Within the single mode RTA approximation, the phonon distribution for mode λ' in Eq. (3-13) (or mode λ' and λ'' for three phonon process) follows the equilibrium Bose-Einstein distribution, and a perturbation is given to mode λ, so that one can compute the phonon lifetime for mode λ by BTE. However, the single mode RTA approximation can underestimate the thermal conductivity for high thermal conductivity materials such as graphene and diamond[20]. This is due to inaccurate treats of the normal phonon-phonon scattering process and the breakdown of the local equilibrium for materials with small phonon scattering rates. Therefore, instead of RTA, we used the iterative solution of BTE[20] here to calculate the thermal conductivity of BAs. For a small temperature gradient (∇T), the nonequilibrium phonon distribution n_λ can be linearly expanded as $n_\lambda = n_\lambda^0 + \left(-\partial n_\lambda^0/\partial T\right)\mathbf{F}_\lambda \cdot \nabla T$, where n_λ^0 is the Bose-Einstein distribution under equilibrium state. $\mathbf{F}_\lambda$ can be derived by iteratively solving the BTE. The lattice thermal conductivity tensor $\kappa^{\alpha\beta}$ can be calculated by summing over all the phonon modes in first Brillouin zone[20,54],

$$\kappa^{\alpha\beta} = \frac{1}{k_B T^2 \Omega N} \sum_\lambda n_0(n_0+1)(\hbar\omega_\lambda)^2 v_\lambda^\alpha F_\lambda^\beta \qquad (3\text{-}15)$$

where $\hbar$ is the Plank constant over 2π, Ω is the volume of unit cell. Here, the first Brillouin zone is discretized by a 28 × 28 × 28 **q** mesh. v_λ^α is the group velocity of phonon mode λ along direction α, which can be calculated from phonon dispersion relation,

$$v_{\lambda\alpha} = \frac{\partial\omega}{\partial q^{\alpha}} \qquad (3\text{-}16)$$

where q^{α} is the wave vector along direction α.

We calculated the second and third order interatomic force constants (IFCs). Second-order IFCs are required for deriving phonon dispersion relation. We obtained second-order IFCs based on density functional theory (DFT)[55,56] and density functional perturbation theory (DFPT)[57] using the PWscf and PHonon codes of Quantum ESPRESSO[58,59] package respectively. In self-consistent calculations of electronic structure using plane-wave basis, we used norm-conserving pseudopotentials under local density approximation for both boron and arsenic[60]. The kinetic energy cutoff for electronic wavefunctions was set as 80 Ry. The lattice constant of BAs is determined by minimizing the total energy of the system in ground-state. After self-consistent calculations of electronic structure, DFPT was applied to obtain the second-order IFCs. For both DFT and DFPT calculation, we used 6 × 6 × 6 Monkhorst-Pack k-points meshes. Third-order IFCs are required for three phonon process of the intrinsic phonon-phonon scattering. The third-order IFCs were obtained from a 4 × 4 × 4 supercell with 128 atoms, using finite displacement method in real space. Up to fifth nearest neighbors were considered. A package thirdorder.py[61] was used to generate an irreducible set of displacements and then extract third order IFCs from the forces acting on atoms under each displacements. The forces acting on atoms was calculated by DFT. After obtaining the IFCs, the lattice thermal conductivity was computed using ShengBTE package[54,62].

We found that our experimental results are in good agreement with the four-phonon DFT calculation, verifying that, the Umklapp phonon scattering dominates phonon interactions. More importantly, our experiments indicate that, unlike in most materials, the probability of higher-order phonon scattering in BAs is important and cannot be ignored. The high-order

anharmonicity we observed for BAs is due to its unique band structure (i.e., large a-o gap and a large mass ratio) that leads to an extremely weak three-phonon process, and provides sufficient numbers of possible four-phonon scattering configurations.

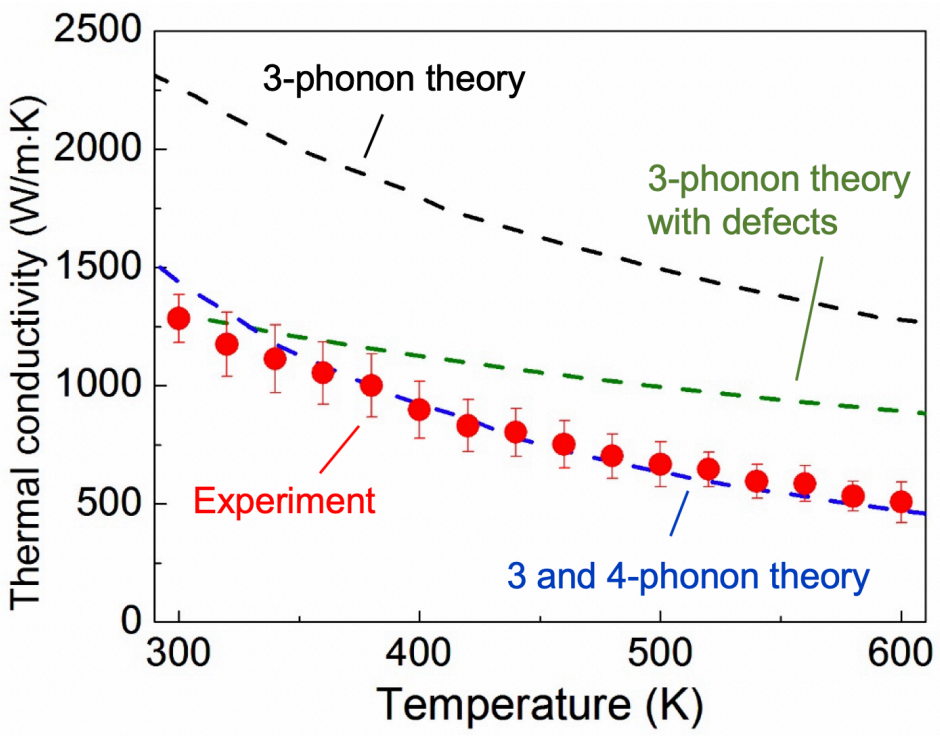

Figure 3.16. *Experimentally measured thermal conductivity of BAs in comparison to ab initio predictions by DFT, considering the three-phonon scattering process*[17] *(black dashed line), the three- and four-phonon scattering process*[25] *(blue dashed line), and the three-phonon scattering process with point defects (green dashed line).*

Another important phonon mechanism for HTC in BAs is its unique phonon mean free path (MFP) spectra that come from its extraordinary phonon band structure. MFPs represent the characteristic lengths corresponding to the distance over which heat carriers transmit thermal energy before being scattered; in general, MFPs can span several orders of magnitude—usually from ~1 nm to ~100 μm. According to the ab initio theory, BAs has a large phononic band gap between acoustic and optical phonon branches, which minimizes acoustic-optical phonon

scattering and leads to MFPs longer than those of most common materials. In particular, BAs phonons with MFPs longer than 1 μm contribute to more than 90% of its total thermal conductivity. By comparison, for diamond and cubic BN, phonons with MFPs longer than 1μm only contribute to about 30% of their total thermal conductivity.

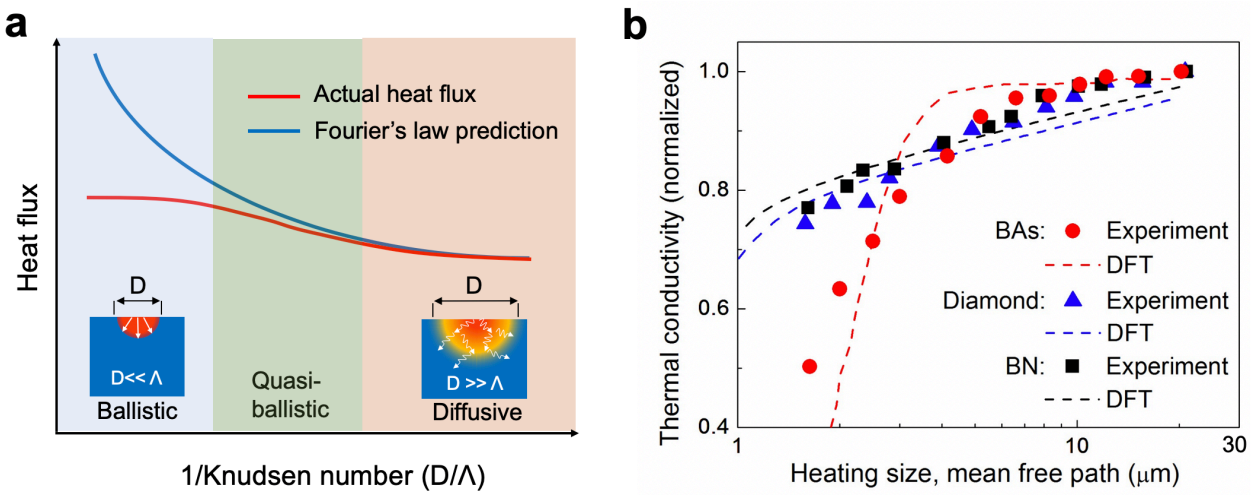

Figure 3.17. *Probing phonon mean free path spectra of BAs through size-dependent ballistic transport.* ***(a)*** *Schematic of heat flux for a fixed temperature difference as a function of the Knudsen number. Red and blue lines indicate the actual heat flux and the flux predicted by Fourier's law, respectively. Insets show that the thermal transport evolves from a diffusive to a ballistic regime when the heating size is gradually reduced. When the actual heat flux was measured and fitted to Fourier's law to obtain an effective thermal conductivity (κ_{eff}), a gradual reduction in κ_{eff} was expected with a decreasing heating size. Essentially, the κ_{eff} decrease is due to the evolution from diffusive to ballistic transport for the phonons with a mean free path comparable to the heating size, and thereby represents the phonon MFP spectra.* ***(b)*** *The normalized effective thermal conductivity was measured for the three best thermal conductors (BAs, diamond, and BN), as a function of heating diameters from 21 to 1.6 μm. Experimental results, compared with the MFP spectra calculated with DFT*[17,25,35]*, indicate that in BAs, a large portion of phonons have long mean free paths, owing to the distinctive band structure of BAs.*

To gain further insight and verify the phonon MFP distribution in BAs, we probed the phonon spectral contribution through exploiting the size-dependent ballistic transport. This quantitative spectral information projects the contributions to thermal conductivity into

characteristic length scales and is key to understanding thermal properties in connection with atomistic phonon theory[34].

Experimentally, this phonon MFP distribution information can be investigated by exploiting the ballistic (or non-equilibrium) heat conduction around a small heating area, with the physical concept described in our recently developed thermal spectral mapping spectroscopy technique (Fig. 3.15a) [24,63]. In this measurement, hot phonons travel from the heated area into the underlying substrate material. The heat transfer regime is controlled by a characteristic thermal length, which is proportional to the heating size D, in comparison to phonon MFPs. In the diffusive limit, when $D >> \Lambda$, propagating phonons experience enough scattering to reach local thermal equilibrium. In this case, Fourier's law accurately describes the transport and heat flux, and the thermal conductivity of materials is simply the bulk value (κ_{bulk}). From the kinetic theory[15], the contribution to the total thermal conductivity from a specific phonon mode is $\kappa_{\omega,bulk} = \frac{1}{3} C_{\omega} \cdot v_{\omega} \cdot \Lambda_{\omega}$. As the heater size D decreases, phonons with $D < \Lambda$ will have fewer opportunities to scatter. In the ballistic limit ($D << \Lambda$), phonons propagate analogously to the thermal radiation over the whole region with a characteristic length of ~ D. Therefore, the actual heat flux will deviate from the Fourier's law prediction for the quasi-ballistic, or ballistic regimes (Fig. 3.15a). Mathematically, the actual heat flux is measured and fitted to Fourier's law to obtain an effective thermal conductivity (κ_{eff}), which gradually decreases in value for smaller Ds, as a higher portion of phonons evolves from diffusive to ballistic transport. The decrease in κ_{eff} (D) represents MFP spectra and should follow the same trend in $\kappa(\Lambda_m)$. Therefore, the size-dependent thermal conductivity measurement can provide a fundamental understanding of such

MFP spectra, although the exact relationship between κ_{eff} and D requires careful atomistic and multi-scale simulations, and is a function of the heating geometry and materials[24,63].

In our experiments, the laser beam served as the heater and we measured the effective thermal conductivity of materials by varying the laser heating size from 21 to 1.6 μm. The thermal conductivity of BAs, diamond, cubic BN were measured simultaneously as a function of the heating sizes (Fig. 3.15b). The results clearly show that ballistic transport occurs in all three materials, but that their thermal conductivity decreases differ. For diamond and cubic BN, κ_{eff} decreases by ~ 26% and 23%, respectively, when reducing the laser heating size from 21 to 1.6 μm. By comparison, under the same conditions, a strong thermal conductivity reduction of ~50% is observed for BAs, indicating that long MFP phonons contribute significantly more to heat conduction in BAs crystals. Our measurements (Fig. 3.15b) are consistent with the DFT-predicted results for these materials[17,25,64]. Phonons with long phonon MFPs (1 ~ 10 μm) contribute to a very high portion of BAs' total thermal conductivity (> 50%). By comparison, in most known materials, phonon MFPs are distributed over a wider range (1 nm ~ 100 μm). Thus, we demonstrated that the ultrahigh thermal conductivity of BAs originates from the enhanced MFPs resulting from its unique phonon band structure.

3.5 Summary

I experimentally observed an ultrahigh thermal conductivity of 460 W/mK and 1300 W/mK at room temperature in synthetic high-quality single-crystal BP and BAs, respectively. My study verifies the prediction from ab initio theory and establishes BP and BAs as a benchmark material with the highest isotropic thermal conductivity of bulk metals and semiconductors. I performed temperature-dependent thermal conductivity measurement using

time-domain thermoreflectance technique and analyzed phonon scattering mechanisms through modeling and multi-scale simulations. My temperature-dependent data suggests that, unlike most common materials, high-order phonon anharmonicity strongly affects heat conduction in boron compounds. I further explored the phonon spectra through probing quasi-ballistic thermal transport and size-dependent measurement. Based on phonon Boltzmann transport equation, the ballistic transport is explained based on phonon mode dependent scattering. Furthermore, in combination of experiment and modeling, I directly constructed the phonon mean free path spectra, which shows that in comparison to most materials, long phonon MFPs contribute to a significantly higher portion of the thermal conductivity. Our experimental discovery of ultrahigh thermal conductivity in boron compound highlights its potential as a new material platform, possibly revolutionizing future thermal management of electronics and photonics. The investigation of fundamental transport mechanisms represents a critical research benchmark in advancing the experiment-theory synergy for the rational design of new materials. Together with the unique chemical inertness and refractory behaviors, this study underscores the promise of BP as a unique high thermal conductivity material for a wide range of applications.

CHAPTER 4

*Physical properties of boron arsenide**

4.1 Introduction

In previous chapter, I report the successful synthesis of single-crystal BAs, along with the measurement of a record-high thermal conductivity of 1300 W/mK, a value which is beyond that of most common semiconductors and metals. Thus, BAs is a promising new semiconductor that could potentially revolutionize the current technology paradigms of thermal management and possibly extend the semiconductor roadmap. To apply BAs to actual electronical and photonic device, it is essential to know complete set of material properties because these highly affect device performance, or some properties may not be suitable for fabrication process. However, many of physical properties of BAs have yet been explored experimentally. In this chapter, I demonstrate the systematic experimental study of our chemically synthesized high-quality BAs crystals, including the measurement of basic BAs characteristics such as, the band gap, optical refractive index, sound velocity, elastic modulus, shear modulus, Poisson's ratio, thermal expansion coefficient, and heat capacity.

(*The work described in this chapter was done in collaboration with M. Li, H. Wu, and H. Nguyen and was the basis for the article published on *Appl. Phys. Lett*., 2019, 115, 122103.)

4.2 Optical properties of BAs

First, I report the experimental measurement of the optical bandgap of BAs. The band gap (E_g) is a major factor that determines the optical absorption and electrical transport in a solid.

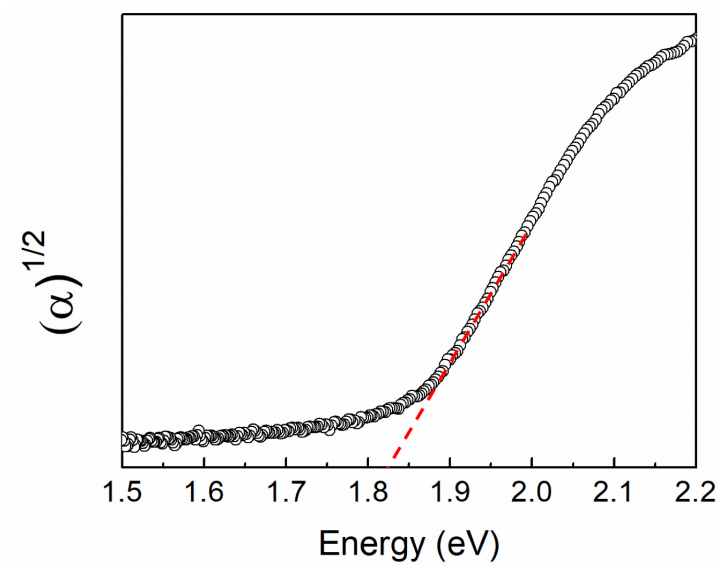

Figure 4.1 *Bandgap measurement from light absorption experiments. The absorptivity is plotted vs the photon energy of a 55 μm thick BAs sample.*

However, owing to the synthesis challenge to obtain high-quality BAs crystals until recently[65], the E_g of bulk BAs remained inconclusive with theoretical calculated values varying from 0.67 to 2.05eV[66–72]. Here I measured the light absorption of BAs to determine E_g using ultraviolet–visible spectroscopy. The transmission spectrum of BAs was collected by scanning light wavelengths with photon energy from 1.5 to 2.2 eV, following the Beer–Lambert law:

$$I / I_0 = e^{-\alpha d} \qquad (4\text{-}1)$$

Where the I and I_0 are the transmitted light and the intensity of incident light, respectively, and α and d are the absorption coefficient and the thickness of sample crystal, respectively. Figure

4.1 shows the absorption measurement data of BAs at room temperature. As an indirect band gap semiconductor, the band edge absorption of BAs was determined by[73]:

$$\alpha \propto (hf - E_g \pm \hbar\Omega)^2 \qquad (4\text{-}2)$$

where h, f, and E_g are respectively the Planck constant, light frequency, a proportional constant, and band gap. Equation (4-2) indicates a threshold in the absorption close to E_g, but with a small $\hbar\Omega$ difference due to the contribution of phonons during the light absorption process, as required by momentum conservation. The absorption data plot of $\alpha^{1/2}$ versus photon energy (hf) fits well onto a straight line, which confirms Equation (4-2) and enables the extrapolation of a band gap of ~ 1.82 eV. Note that E_g of BAs could be slightly shifted due to the absorption or emission of phonons, whose energies at the X point are 0.02 ~ 0.04 eV for transverse acoustic (TA) and longitudinal acoustic (LA) branches. In addition, the experimental curve shows a tail extending down to about 1.5 eV, which is caused by the absorption of high-energy phonons or multi-phonons.

I also measured the refractive index of BAs. The refractive index (n) is a dimensionless number that describes how fast light propagates through the material. n is key parameter for photonic applications and that of BAs was unknown so far. Theoretical refractive indexes of BAs appearing in recent literature have different values, possibly due to variations in pseudo-potentials[68,74] or empirical relationships[75]. Here, I directly measured the refractive index of BAs by Fabry-Perot interference. When light passes through a BAs crystal with smooth surfaces (inset of Fig. 4.2a), the top and bottom surfaces can serve as two parallel reflecting mirrors. The transmission spectrum measured as a function of wavelength from 657 to 908 nm exhibits large transmission oscillations corresponding to resonances, which are measured (Fig. 4.2a). n can be extracted from following equation under normal light incidence[76,77]:

$$n = \frac{M\lambda_1\lambda_2}{2(\lambda_1 - \lambda_2)d} \tag{4-3}$$

where M is the number of fringes between the two extrema (M = 1 between two consecutive maxima), and λ_1 and λ_2 are the corresponding wavelength of light between fringes.

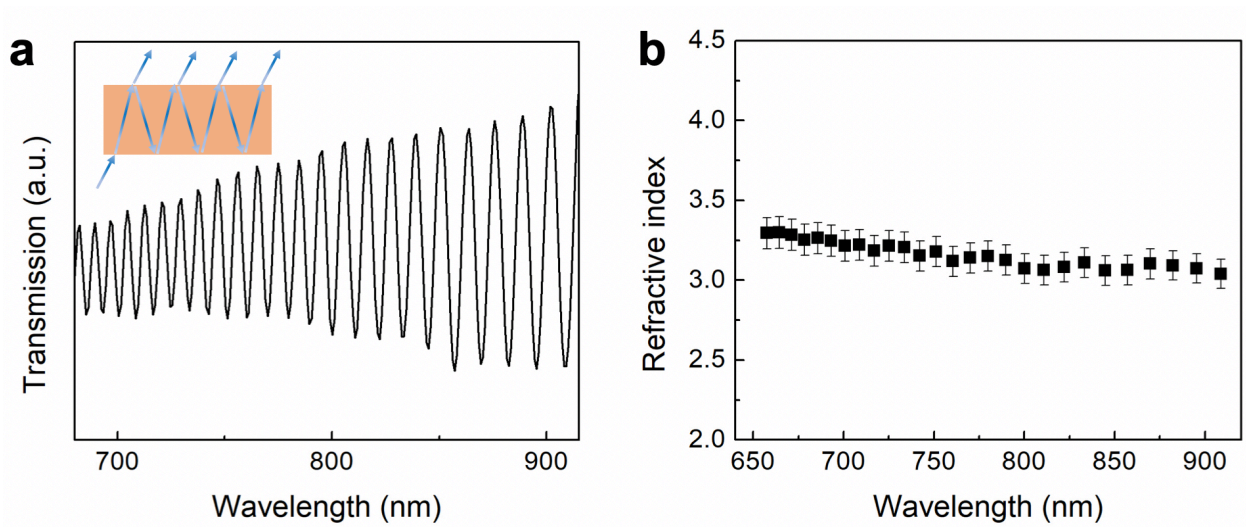

Figure 4.2. *(a) Refractive index measurement from a Fabry–Pèrot interference experiment: the optical transmission measured on a 8.79 μm thick BAs sample shows strong oscillations due to resonances from the light reflected by the top and bottom sample surfaces (inset); and (b) wavelength dependent refractive index of BAs.*

Figure 4.2a shows the measured transmission data of an 8.79 μm thick BAs crystal for optical wavelengths varying from 657 to 908 nm. The transmission spectrum shows clear interference patterns with oscillations between maxima and minima. The refractive index of BAs was measured as n = 3.29 to 3.04 with increased optical wavelengths from 657 to 908 nm and plotted in Figure 4.2b The refractive index of BAs is close to that of prototyped optoelectronic materials, such as GaP (3.2 at 900 nm)[78] and GaAs (3.7 at 876 nm)[79].

4.3 Mechanical properties of BAs

I measured the basic mechanical properties of BAs, including elastic modulus, shear modulus, sound velocity, and Poisson's ratio. The stresses and strains of a material are connected by a linear relationship mathematically following Hooke's spring law:

$$\sigma_{ij} = C_{ijkl}\varepsilon_{kl} \tag{4-4}$$

where σ, C, and ε are the stress, stiffness, and strain, respectively. In general, for anisotropic materials, C_{ijkl} is a fourth-order tensor with a total of 81 components[80,81] called the stiffness tensor or elasticity tensor. Under the symmetry and Voigt notation[82], the stiffness tensor can be simplified to 36 components. For cubic symmetry materials, such as BAs, only 3 constitutive components— C_{11}, C_{12}, C_{44}— are independent. They are closely related with the sound velocities as discussed below.

To measure the stiffness of BAs, we first performed picosecond ultrasonic measurements[83] to determine sound velocity using a pump-probe ultrafast optical spectroscopy[24,84–86] (Fig. 2.5a). In this setup, a thin aluminum layer is deposited on the BAs thin film sample surface to serve as the optical transducer and a picosecond laser pump generates a longitudinal acoustic wave from the aluminum layer that penetrates into the BAs sample, travels across it, reflects back, and creates sound echoes. The sound echoes are detected by a probe pulse laser with a controlled sub-picosecond stage delay (Figure 4.3a).

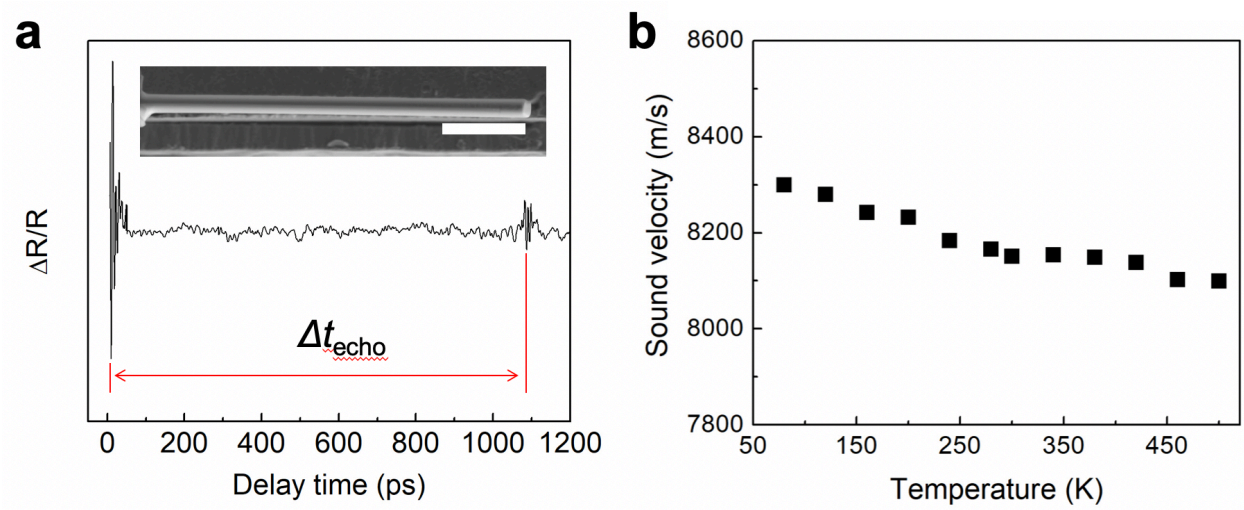

Figure 4.3. *(a) Picosecond acoustic data: the sound echoes indicate a round trip of the acoustic wave generated inside the BAs sample. The inset shows a thin film (4.37 μm) of BAs prepared with a focused ion beam in the (111) plane; (c) temperature dependent sound velocity of BAs.*

The time delay (Δt_{echo}) between echoes is measured and contributed to by the round trip of the acoustic wave in the BAs film with a given thickness, d. Note that the consecutive oscillations (with smaller amplitude) are caused by sound echoes involving the aluminum layer. We prepared a BAs thin film slab along the (111) orientation using a focused ion beam (FIB) (inset of Figure 4.3a). The longitudinal sound velocity in the <111> direction of BAs was therefore measured as,

$$v_{LA,111} = \frac{2d}{\Delta t_{echo}} \qquad (4\text{-}5)$$

The room temperature $v_{LA,111}$ is 8150 ± 450 m/s. We also measured the temperature-dependent sound velocity of BAs from 80 to 500 K and plotted the results in Fig. 4.3b, indicating a slightly decrease with increased temperature. Note that the stiffness C_{44} of BAs can be linked with $v_{LA,111}$, C_{11} and C_{12} with the following formula[87],

$$C_{44} = \frac{(3\rho v_{LA,111}{}^2 - C_{11} - 2C_{12})}{4} \qquad (4\text{-}6)$$

where ρ is the mass density measured as 5.22 g/cm^{3}for BAs[65]. Since C_{11} and C_{12} can be linked by[80] $C_{12} = \frac{3B - C_{11}}{2}$ where B is the bulk modulus reported as 148 GPa[88], and C_{11} cancels out in Equation (4-6) leaving a relationship between C_{44} and $v_{LA,111}$. Therefore, from these results, the stiffness C_{44} is determined to be 149 GPa. The transverse acoustic velocity along <100> direction is $v_{TA} = \sqrt{C_{44} / \rho}$ = 5340 ± 510 m/s.

To obtain the stiffness C_{11} value of BAs, we measured surface acoustic waves (SAW)[89] on BAs samples (Fig. 2.5b). Periodic aluminum lines (with a period of L) were fabricated on the surface of BAs samples (Fig. 4.4a) and aligned with the desired crystal directions using electron beam lithography[90], and heated up by a pulsed laser to generate periodic thermal strains that partially pass through the BAs crystals to form SAWs[10,24,91].

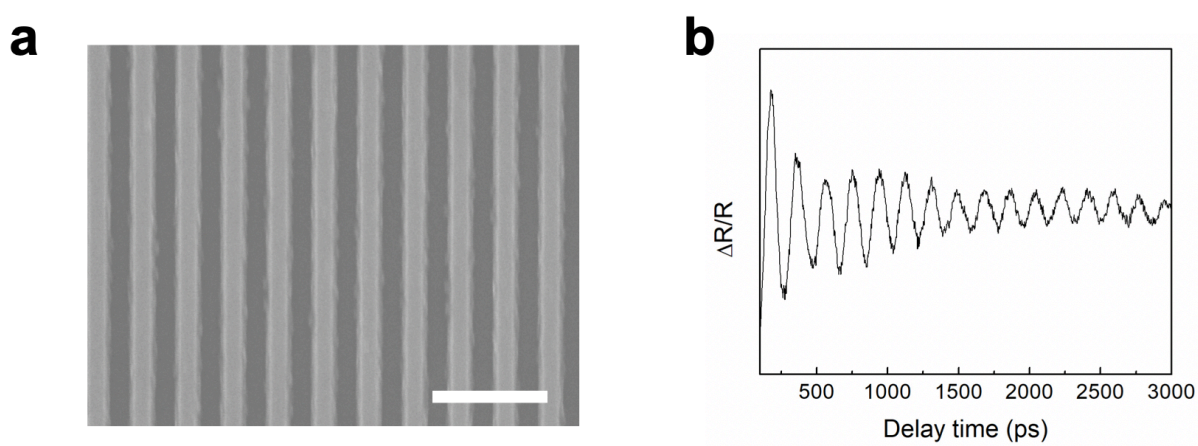

Figure 4.4. *(a) Al grating on top of BAs surface fabricated by e-beam lithography for SAW velocity measurement. Scale bar is 1μm. (b) Reflectance change as function of delay time. Periodic oscillation corresponds to propagation of SAW.*

The SAW propagating along the BAs surface and detected by a laser probe shows strong periodic oscillations with a time periodicity of Δt_{SAW} in the reflectance signal (Fig. 4.4b). The velocity of the SAW can be measured from the oscillation curve in the ultrafast time domain. For example, for the main top crystal surface in the (111) orientation, the SAW velocity was measured as: $v_{SAW} = L/\Delta t_{SAW}$ = 4320 ± 120 m/s at room temperature, and this value is used to extract the C_{11} of BAs as discussed below.

In general, the bulk wave equation for the displacement in a perfectly elastic and anisotropic medium can be written

$$C_{ijkl}\frac{\partial^2 u_k}{\partial x_l \partial x_j} = \rho \frac{\partial^2 u_i}{\partial t^2} \qquad (4\text{-}7)$$

where the u_i are the displacement components along the Cartesian axes x_i to which the stiffness tensor C_{ijkl} is referred. P is the density of the material, and the Einstein summation on repeated subscripts is implied. For bulk waves, the solutions of Equation (4-7) are plane waves. However, for SAWs, these solutions represent the modes of propagation of elastic energy along the free surface of a half-space, and their displacement amplitudes decay exponentially with depth beneath the surface, so that most energy is concentrated within a wavelength distance below the surface[89,92]. When a combination coefficient (*A)* for each wave component is used to consider the direction-dependent free propagation, space confinement, and amplitude decays respectively, the solution for SAWs can be written as linear combinations[89]

$$u_i = \sum_m A^{(m)} U_j^{(m)} \exp(ik(l_i x_i - \upsilon_{SAW} t)) \qquad (4\text{-}8)$$

where k, U_j, δ_{ij} are the wave vector, wave amplitude, and Kronecker delta, respectively, and l is the directional vector of the wave propagation. The solution of equation (4-8) can be

determined by substituting the wave forms of equation (4-8) into the wave equation (4-7) that leads to the Christoffel equation

$$[k^2 l_i l_l C_{ijkl} - \rho\omega^2 \delta_{ij}][U_i] = 0 \qquad (4\text{-}9)$$

where ω is the SAW frequency, $\omega = k \cdot v_{SAW}$. Thus, the only unknown parameter A can be determined by using the periodic mass boundary condition[93] of the experimental system and the eigenvector l_i and U_i can be obtained by solving Equations (4-7~4-9)[89]. The stiffness C_{11} is thereby determined to be 285 GPa and the longitudinal acoustic velocity in the [100] direction, calculated by $v_{LA} = \sqrt{C_{11}/\rho}$, is 7390 m/s.

Therefore, all the stiffnesses of BAs were measured as C_{11}= 285 GPa; C_{12} = 79.5 GPa; and C_{44} = 149 GPa, and the corresponding elastic compliances are: $S_{11} = \frac{C_{11}+C_{12}}{(C_{11}-C_{12})(C_{11}+2C_{12})}$ = 3.99×10^{-12}Pa^{-1}; $S_{12} = \frac{-C_{12}}{(C_{11}-C_{12})(C_{11}+2C_{12})}$ = -0.87×10^{-12}Pa^{-1}; and $S_{44} = \frac{1}{C_{44}}$ = 6.71×10^{-12}Pa^{-1}.

The elastic modulus of an arbitrary direction is determined from the elastic compliances[94]

$$E_{hkl} = \frac{1}{S_{11} - 2(S_{11} - S_{12} - 0.5S_{44})(a_1^2 a_2^2 + a_2^2 a_3^2 + a_3^2 a_1^2)} \qquad (4\text{-}10)$$

where <*hkl*> is the Miller index that denotes the crystallographic directions. a_1, a_2, a_3 are directional cosine between the <*hkl*> and <100> directions. Hence, the elastic modulus of BAs along any direction can be obtained from the measurements. For example, E_{100}, E_{110}, and E_{111} of the three major directions, <100>, <110>, and <111> are 250GPa, 308GPa, and 335GPa, respectively. In addition, the Poisson's ratio of BAs, determined similarly to the equation (4-10), is[94]

$$\upsilon_{ab} = -\frac{S_{12} + (S_{11} - S_{12} - 0.5S_{44})(e_1^2 b_1^2 + e_2^2 b_2^2 + e_3^2 b_3^2)}{S_{11} + (S_{11} - S_{12} - 0.5S_{44})(e_1^2 e_2^2 + e_2^2 e_3^2 + e_3^2 e_1^2)} \tag{4-11}$$

where e_1, e_2, e_3 are directional cosine of the transversal strain direction with respect to the <100> direction. b_1, b_2, b_3 are the directional cosine of the axial strain direction with respect to the <100> direction.

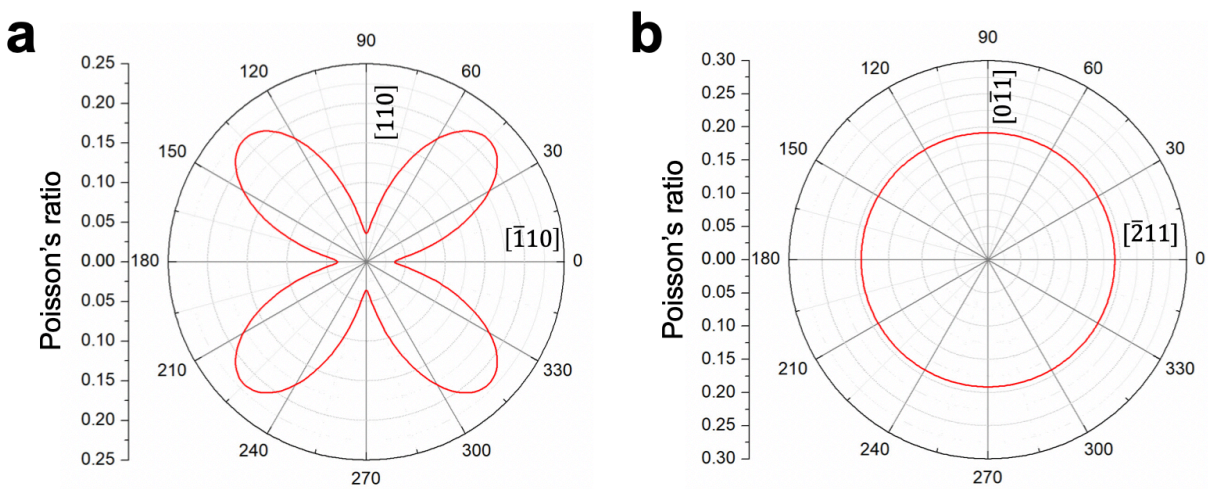

Figure 4.5. *Poisson's ratio of BAs on (a) (100) plane and (b) (111) plane.*

The Poisson's ratio in the <100> direction on the (100) plane was measured as 0.22. On the other hands, the Poisson's ratio on (111) plane was measured as 0.19 to all direction. Additionally, the averaged elastic (E_{VRH}) and shear moduli (G_{VRH}) of the polycrystalline form of BAs can be determined by Voigt-Reuss-Hill average method[95]

$$E_{VRH} = \frac{1}{2}\left(\frac{(C_{11} - C_{12} + 3C_{44})(C_{11} + 3S_{12})}{2C_{11} + 3C_{12} + C_{44}} + \frac{5}{3S_{11} + 2S_{12} + S_{44}}\right) \tag{4-12}$$

$$G_{VRH} = \frac{1}{2}\left(\frac{(C_{11} - C_{12} + 3C_{44})}{5} + \frac{5}{4(S_{11} - S_{12}) + 3S_{44}}\right) \tag{4-13}$$

The averaged elastic and shear moduli were measured as 326 GPa and 128 GPa, respectively. Despite a lower sound velocity, it should be noted that the averaged elastic modulus of BAs is about twice as high as that of silicon (~160 GPa) and comparable to that of GaN (~300 GPa), due to the large mass density. This result suggests that BAs is a good material for mechanical applications, such as mechanical micromachining and high-pressure applications.

4.4 Thermophysical properties

We also measured the thermal expansion coefficients of BAs by temperature dependent X-ray diffraction (XRD) using a Cu Kα radiation source. Figure 4.6a shows the XRD data of BAs collected from 293 to 773 K. As the temperature increases, the (311) peak of the BAs crystal clearly shifts to a smaller angle (Figure 4.6a), which indicates a decrease in the d-space and an increase of the lattice constant. The measured lattice constant of BAs at 298K is 4.78Å, which is in good agreement with our previous reported value[65]. The temperature-dependent lattice constants of BAs, measured and plotted (Figure 4.6b), were used to obtain the linear thermal expansion coefficient (α_L),

$$\alpha_L \equiv \frac{1}{l}\frac{dl}{dT} \qquad (4\text{-}14)$$

where the l is the lattice constant and T is the temperature. Using the least square method we fitted the measured α_L(T) with a second-order polynomial curve to obtained the best fit shown as the red line in Figure 4.6b. Figure 4.6c shows a plot of the measured temperature-dependent α_L of BAs; α_L is 3.85×10^{-6}/K at 298 K (room temperature) and increases to 6.06×10^{-6} /K at 723 K.

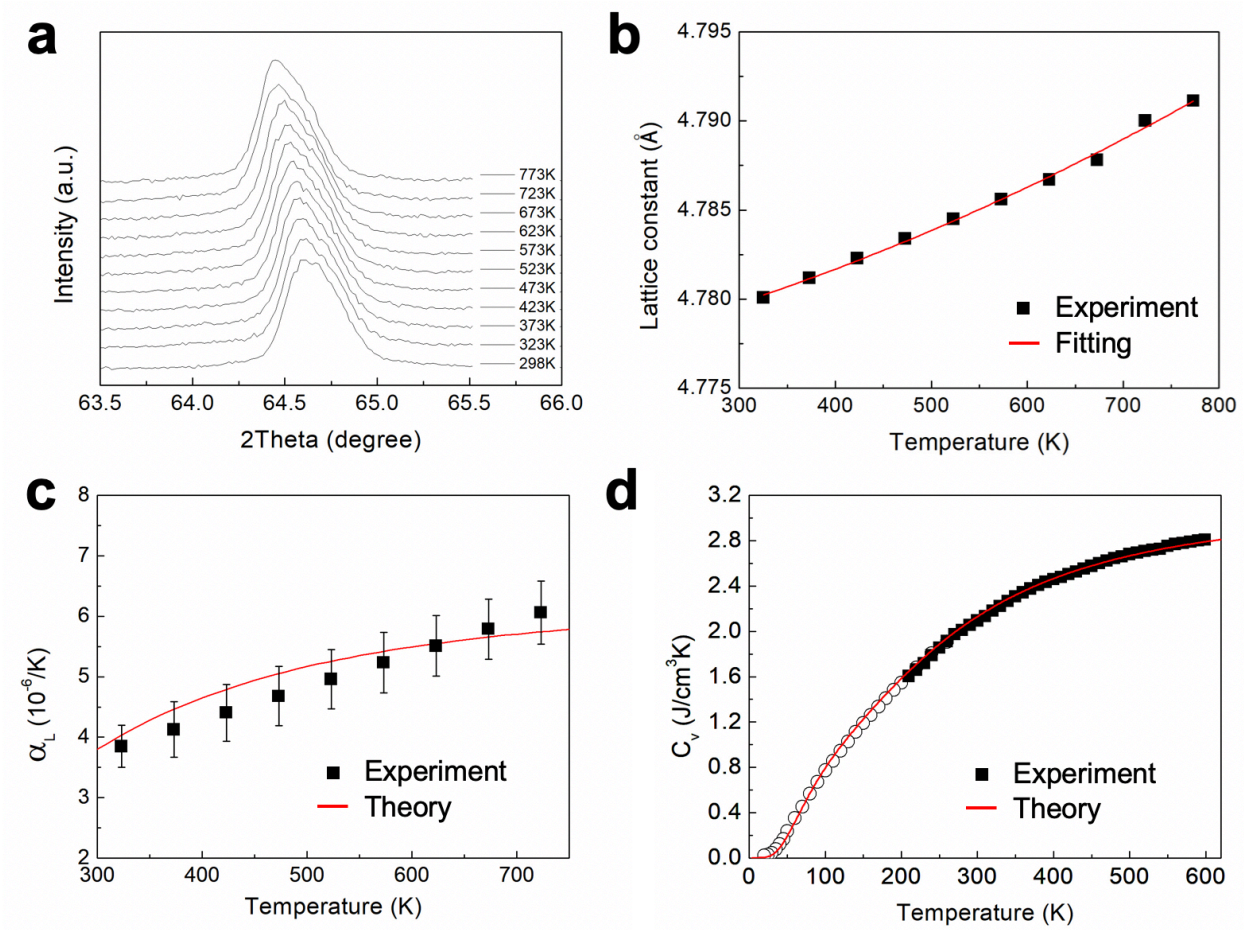

Figure 4.6. *Thermal properties of BAs. (a) The temperature dependent X-ray diffraction (XRD) measurement for (311) peaks with temperatures from 298 K to 773 K; (b) the measured lattice constant of BAs as a function of temperature. The red line represents the second order polynomial fitting; (c) the linear thermal expansion coefficient (α_L) of BAs with temperature dependence; and (d) the specific heat (C_V) of BAs from 5 to 600 K. Symbols indicate experimental data, and the red line represents the DFT calculations.*

Due to its cubic structure, BAs has a volumetric thermal expansion $\alpha_v = 3 \cdot \alpha_L = 11.55 \times 10^{-6}$/K at room temperature. Here, we also performed *ab initio* calculations of the thermal expansion of BAs. Under quasi-harmonic approximation, the thermal expansion coefficient can be calculated from the phonon dispersion relation and mode-dependent Grüneisen parameters[96–98]. The phonon dispersion relation is calculated from the 2nd order interatomic force constants (IFCs). Mode-dependent Grüneisen parameters are calculated from the 2nd and 3rd order IFCs

using ALAMODE package[99]. The IFCs are calculated based on 216 atoms supercell using finite displacement plus least square fitting method. Up to the 5th nearest neighboring atoms are considered for 3rd order IFCs. The force acting on each atom is calculated by DFT with 2 × 2 × 2 Monkhorst-Pack k-points meshes for supercell. We set the cut-off kinetic energy at 120 Ry and the convergence threshold for self-consistency iteration at 1×10^{-11} Ry. This calculation shows good agreement with our measurement results (Fig. 4.6c).

Knowledge of the thermal expansion property of BAs is critical for its integration into high-power electronics materials, which will benefit from the ultrahigh thermal conductivity of BAs. A thermal expansion match between device layers is desired to minimize the residual stress and prevent the delamination of materials with their adjacent layers, as well as to reduce the thermal boundary resistance[100]. Therefore, it is worthy to compare α_L of BAs with those of GaN and GaAs, as they are potential target materials for passive cooling application of BAs. α_L of GaN is 3.94×10^{-6}/K at 300 K and 5.33×10^{-6}/K at 800K (a-axis)[101], and that of GaAs is 5.9×10^{-6}/K at 300K[102]. These values are very close to our measured thermal expansion coefficients of BAs, thereby underscoring the high promise of BAs as a superior cooling material for high power and high frequency GaN or GaAs electronic devices. In comparison, most prototype high thermal conductivity materials, such as diamond (1.6×10^{-6}/K)[103] and SiC (3.2×10^{-6}/K)[104] at room temperature, have a much larger thermal expansion mismatch that can potentially lead to thermal mechanical instability and large thermal boundary resistances.

We also measured the temperature dependent specific heat (C_v) of BAs using differential scanning calorimetry and plotted results in Fig. 4.6d. In addition, we performed *ab initio* calculations to derive the specific heat from the phonon dispersion[105] using the same DFT settings as discussed above. When plotted together, our experimental data from this and prior

work[65,106] show good agreement with the DFT calculations (Fig. 4.6d). The Grüneisen parameter (γ)[107] is generally used to describes the effect of volumetric change of a crystal lattice on the vibrational properties , and is a weighted average overs all phonon modes[86] and can be calculated by

$$\gamma = \frac{\alpha_v B}{C_v} \qquad (4\text{-}15)$$

where α_v and C_v are the volume expansion coefficient —$3\alpha_L$ for BAs—and the volumetric specific heat capacity, respectively. In our study, the room temperature Grüneisen parameter of BAs was determined as $\gamma = 0.82$.

4.5 Crystal stability

To evaluate the stabilities of BAs crystals, I measure the thermal conductivity of our BAs crystal after 12 months from its growth. I keep our sample in the atmosphere condition (300K, 1atm, and ~ 60% of relative humidity). We found that there is no degradation in the thermal conductivity of BAs, indicating that BAs crystal is stable in the air up to 12 months. Furthermore, I confirmed temperature stability of our BAs crystal. I prepare four BAs crystals and heat up each BAs crystal up to 873K, 1073K, 1173K, and 1373K, respectively, in the vacuum for 12 hours and cooling down to room temperature. I repeat the temperature cycle twice and find that BAs decompose between 1173K and 1373K. Figure 4.6 shows that SEM image of BAs crystal heated up to 1173K (Fig. 4.6(a)) and 1373K (Fig. 4.6(b)). FIB technique is used to cut sample to observe inside of crystal. Figure 4.6(b) clearly shows decomposition of BAs, but Fig. 4.6a shows no different with typical BAs crystal.

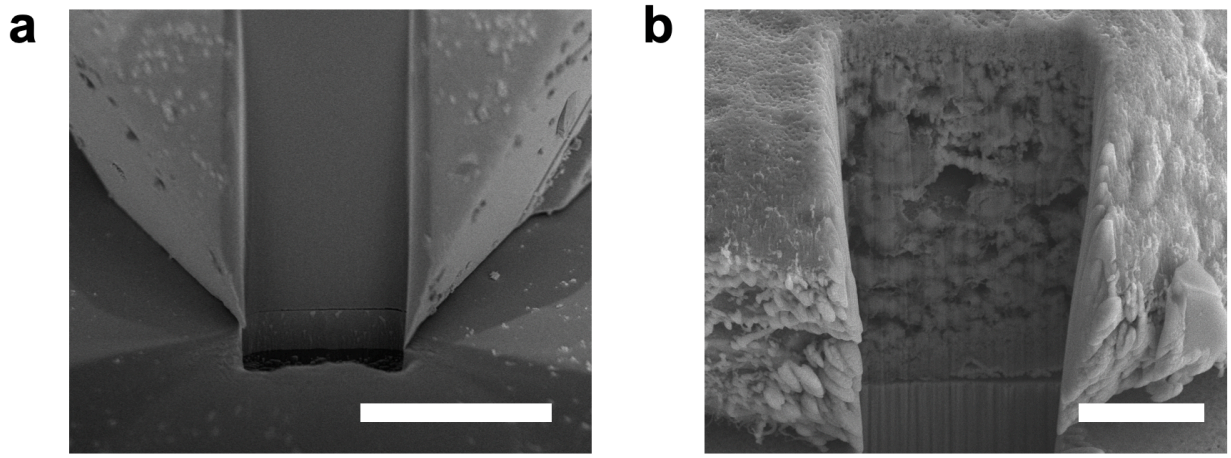

Figure 4.7. *Temperature stability of BAs. (a) SEM image of BAs after heating up to 1173K. Scale bar is 20 µm. (b) SEM image of BAs after heating up to 1373K. Scale bar is 5 µm.*

To test acid stability of crystal, BAs crystal is dipped into HNO_3 for one day. Figure 4.8 shows that SEM image of BAs crystal after dipping into nitric acid which shows that HNO_3 significantly reacts which BAs crystal. Anisotropic reaction is observed. Top surface shown in figure 4.8 is (111) crystal direction which is less reactive with HNO_3 than other crystal direction. It assumed that high atomic density of (111) direction is more resistive for acid.

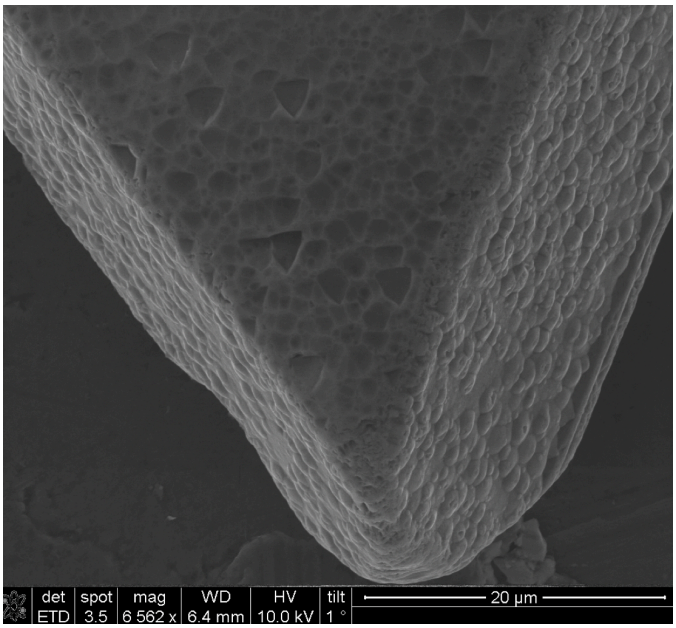

Figure 4.8. *SEM image of BAs after dipping into nitric acid for 1 day.*

4.6 Summary

In summary, we report for the first time the systematic experimental measurements of important basic physical properties of cubic BAs, including the band gap, refractive index, elastic modulus, shear modulus, Poisson's ratio, and thermal expansion coefficient, and specific heat capacity. The database of the physical properties of BAs, summarized in Table 1, is now complete after addition of the experimental values from this work to the literature. With an ultrahigh thermal conductivity of 1300 W/mK[65], I believe that the systematically reported physical properties of BAs will further facilitate the development of this new semiconductor for thermal, electrical, optical, and mechanical applications.

Physical property	Experimental value
Crystal structure	Zinc-blende cubic ($F\bar{4}3m$)
Lattice constant (Å)	4.78
Band gap (eV)	1.82
Refractive index	3.29 (657nm) 3.04 (908nm)
Mass density (g/cm^3)	5.22
Stiffness C_{11}, C_{12}, C_{44} (GPa)	285, 79.5, 149
Compliance S_{11}, S_{12}, S_{44} ($\times 10^{-12}$ Pa^{-1})	3.99, -0.87, 6.71
Averaged elastic modulus (GPa)	326
Averaged shear modulus (GPa)	128
Bulk modulus (GPa)	148
Poisson's ratio	0.22 (<100> direction on (001) plane) 0.19 (all direction on (111) plane)
Longitudinal sound velocity (m/s)	7390 (<100> direction) 8150 (<111> direction)
Transverse sound velocity (m/s)	5340 (<100> direction)
Thermal conductivity (W/m·K)	1300
Volumetric heat capacity (J/cm^3 K)	2.09
Thermal expansion coefficient (K^{-1})	3.85×10^{-6} (linear) 11.55×10^{-6} (volumetric)
Grüneisen parameter	0.82

Table 4.1. *Summary of basic physical properties of BAs at room temperature.*

CHAPTER 5

*Strong phonon anharmonicity and ultralow thermal conductivity in single crystal tin selenide**

5.1 Introduction

Layered van der Waals materials have been intensively investigated for their exotic properties[108–117]. Very recently, tin selenide (SnSe) has drawn a lot of attention because of the reported exceptional thermoelectric properties[117–126]. For thermoelectrics, the heat-to-electricity energy conversion efficiency of SnSe is improved by a very low thermal conductivity. However, the fundamental mechanisms behind the ultralow thermal conductivity in SnSe have remained elusive. Experimentally, different results have been reported in the literature due to varied crystal quality including mass density, polycrystallinity, doping levels, carrier densities, defects, and phase mixing etc.[117,119,127–132]. Theoretically, in semiconductors, thermal transport is generally considered as the entropy propagation and interactions of phonons, i.e. the quantum-mechanical modes of lattice vibrations[15,105]. Under current phonon theory, most calculations take harmonic models[126,133] that are limited to quadratic terms in the interatomic potential or quasi-harmonic models[134–136] that assume harmonic oscillators after frequency renormalization to account for the thermal expansion.

(*The work described in this chapter was done in collaboration with H. Wu and M. Li and was the basis for the article published on, *Nano Lett.,* 2019, 19(8), 4941-4948.)

Therefore, it remains unclear if these theory calculations can be sufficient to explain the behaviors in those materials with strong anharmonicity like SnSe. To clarify the confusion and understand the intrinsic thermal property, here we perform nanoscale anisotropic thermal transport study and *ab initio* calculation on un-doped and fully dense single crystals of SnSe.

5.2 Material synthesis and structural characterization

To investigate the intrinsic properties, it is key to minimizing defects and achieving high quality crystals. High quality single-crystal SnSe was synthesized through a repeated multi-step chemical vapor transport process. Details of the chemical vapor transport setups and synthesize process to grow high-quality single crystals can be found in our recent publications [S1-S3]. Stoichiometric ratio of high-purity Tin (Sn) and selenium (Se) (99.999% purity, from Alfa Aesar) were placed into a quartz tube. This tube was evacuated and flame sealed under high vacuum (10^{-5} torr). A customized multi-zone reactor was set up with reaction temperatures of 1223 K and 1173 K for the hot and cold zones, respectively. Temperature changes were controlled with a very slow rate for over 12 hours. The reactor was held at the reaction temperatures for over 96 hours and then cooled down to room temperature. The initial growth led to crystal ingots. The as-grown crystals were pulverized and returned to the quartz tube, which was evacuated, flame sealed, and loaded into the reactor. This growth procedure was repeated until high quality single crystal SnSe with the close-to-theory maximum density were obtained. Fig. 5.1a shows an optical image of as-grown SnSe samples, and Fig. 5.1b depicts its crystal structure. At room temperature, single-crystal SnSe is a layered material with an orthorhombic structure, which is classified as Pnma space group, #62.

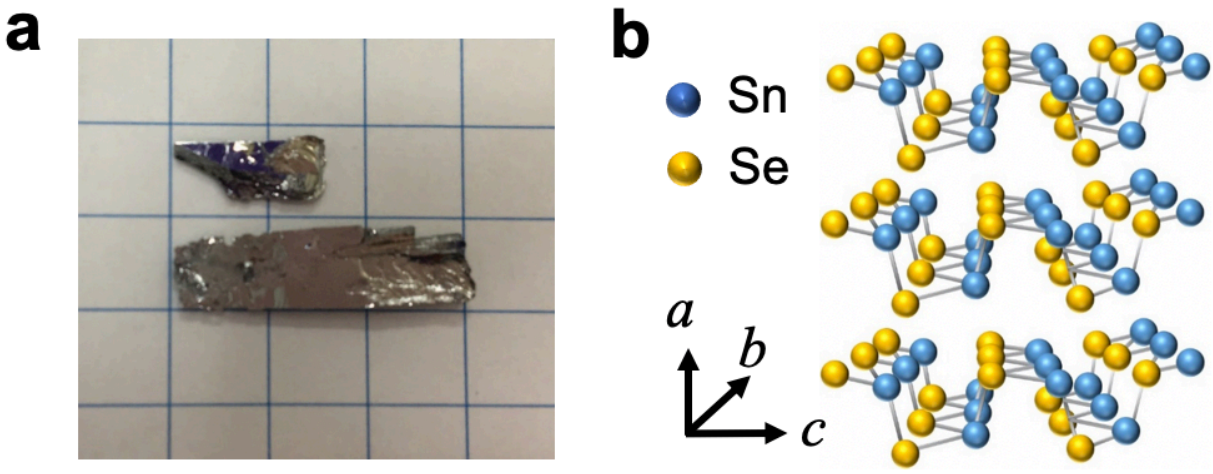

Figure 5.1. *(a) Optical image of as-grown SnSe sample. Scale bar is 1cm. (b) Crystal structure of SnSe.*

X-ray diffraction (XRD) measurement on the a-axis cleavage plane (Fig. 5.2) clearly shows the diffraction peaks from lattice planes (400), (600) and (800), indicating that the cleaved plane is perpendicular to the a-axis and that no defects and grains are observable.

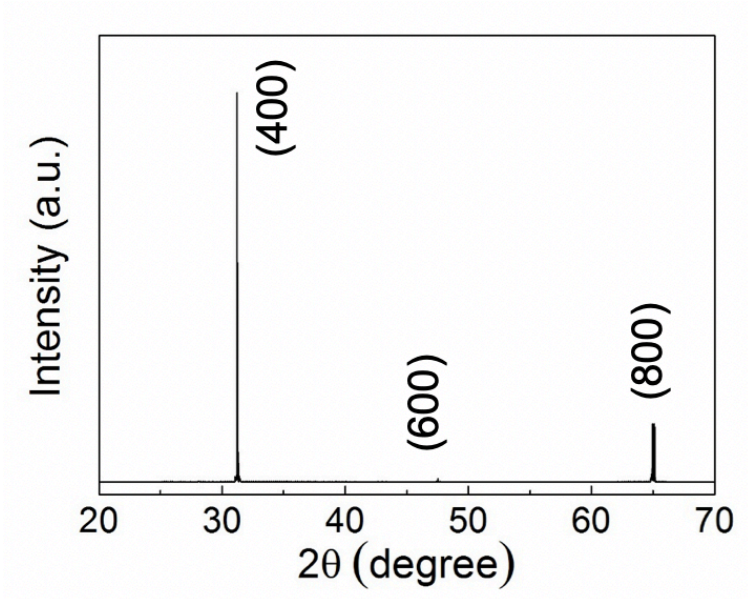

Figure 5.2. *Powder XRD data of SnSe.*

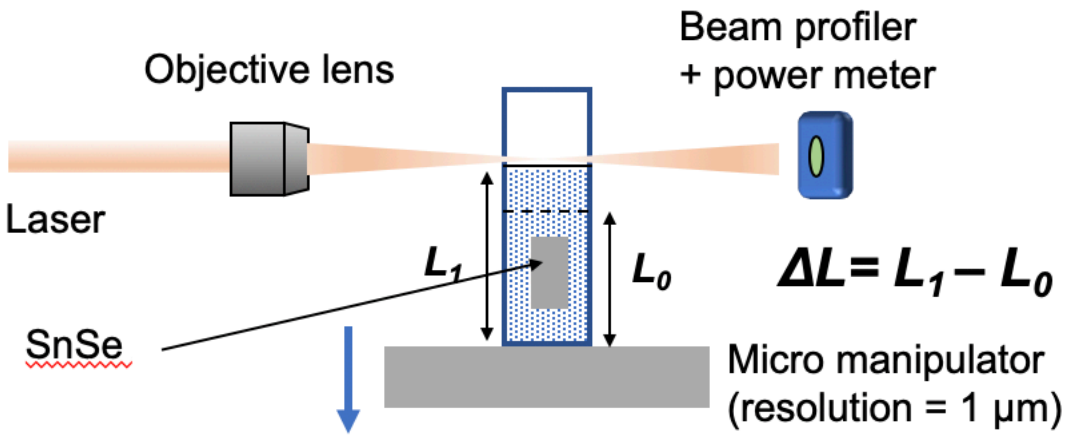

Figure 5.3. *Precise density measurement of SnSe .*

In addition, we measured the mass density of the as-grown SnSe sample using Archimedes' principle. Figure 5.3 shows our density measurement setup. SnSe crystal is dipped in mineral oil and volume of SnSe is calculated from changing height of liquid caused by SnSe crystal. We excite laser at liquid meniscus near top surface. If laser hit the liquid meniscus, the laser beam refracts, and beam position is different with initial position. Beam position and intensity is monitored by changing height of sample stage. The measured value, 6.10 g/cm^3, approaches the theoretical value and verifies the high quality of the synthesized SnSe crystals. Raman spectroscopy (Fig. 5.2a-b) is used to examine defects and in-plane crystal disorder in large area shows no difference between Raman spectra performed at different spots throughout the whole SnSe samples (> 1 cm), thus validating the large-scale uniformity of our synthetic SnSe single-crystals.

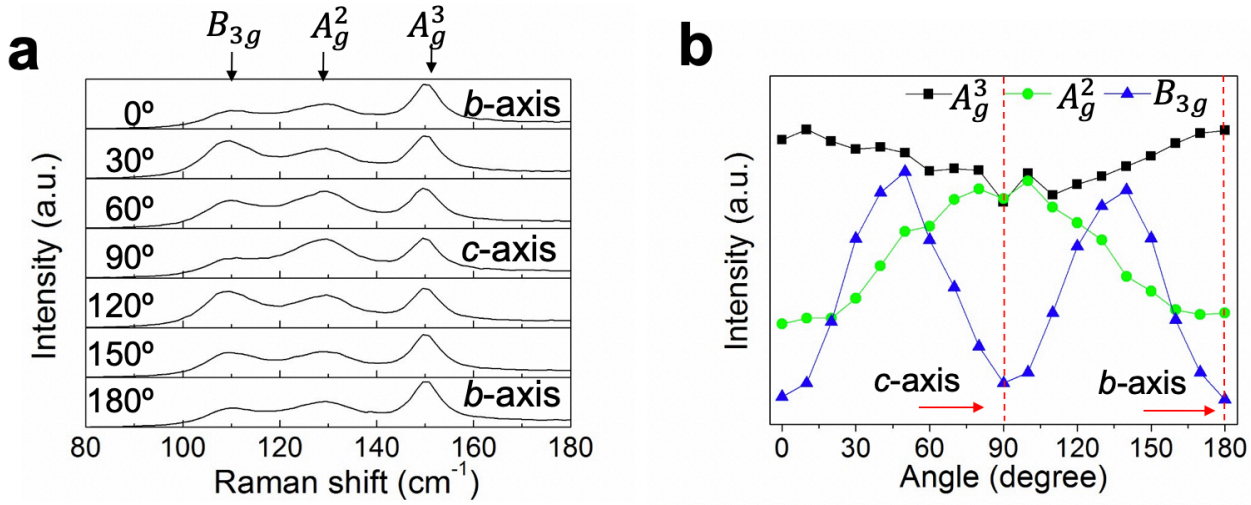

Figure 5.4 *Raman spectra of SnSe. (a) Raw Raman data of SnSe (b) Angle dependent intensity of each Raman peak.*

To measure the anisotropic thermal properties of SnSe, the crystal orientation was identified by angular dependent Raman spectroscopy. Under the parallel incidence of the laser beam to the a-axis of SnSe, only A_g and B_{3g} modes were excited and measured, as shown by the three peaks located at 130 cm^{-1}, 151 cm^{-1} and 108 cm^{-1} Raman shifts (Fig. 5.2a). Due to its highly anisotropic structure, SnSe possesses angular dependent Raman spectra[137]: for example, the A_g^2 peak was maximized when the laser polarization direction was perpendicular to the zigzag direction. Therefore, the crystal orientation was identified by measuring the angle dependent intensity of the Raman signal (Fig. 5.2b).

Before thermal conductivity measurement, the specific heat of SnSe was measured across the temperature range from 120 K – 300 K, using the differential scanning calorimetry (PerkinElmer DSC 8000), the two furnaces system and the StepScan mode of which ensured the measurement accuracy. The measurement parameters were set as 10 K/min for the heating rate,

10 K for the temperature interval, 1 min for thermalization time and 20 mL/min for the nitrogen purge flow rate. The temperature-dependent specific heat of SnSe was plotted by averaging ten repetitive measurement results (Fig. 5.3) [S15].

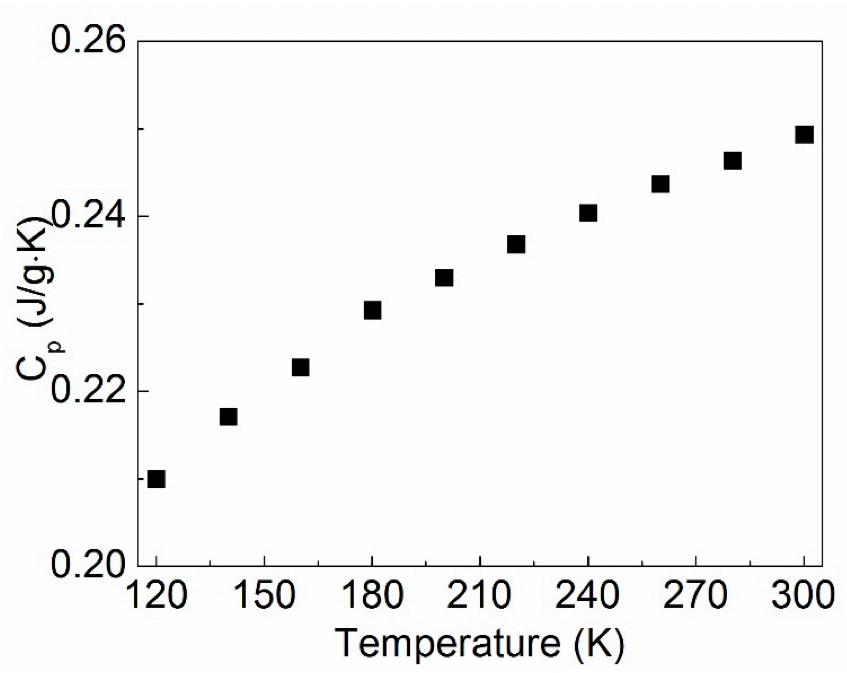

Figure 5.5 *Temperature dependent specific heat capacity of SnSe*

5.3 Anisotropic thermal transport study

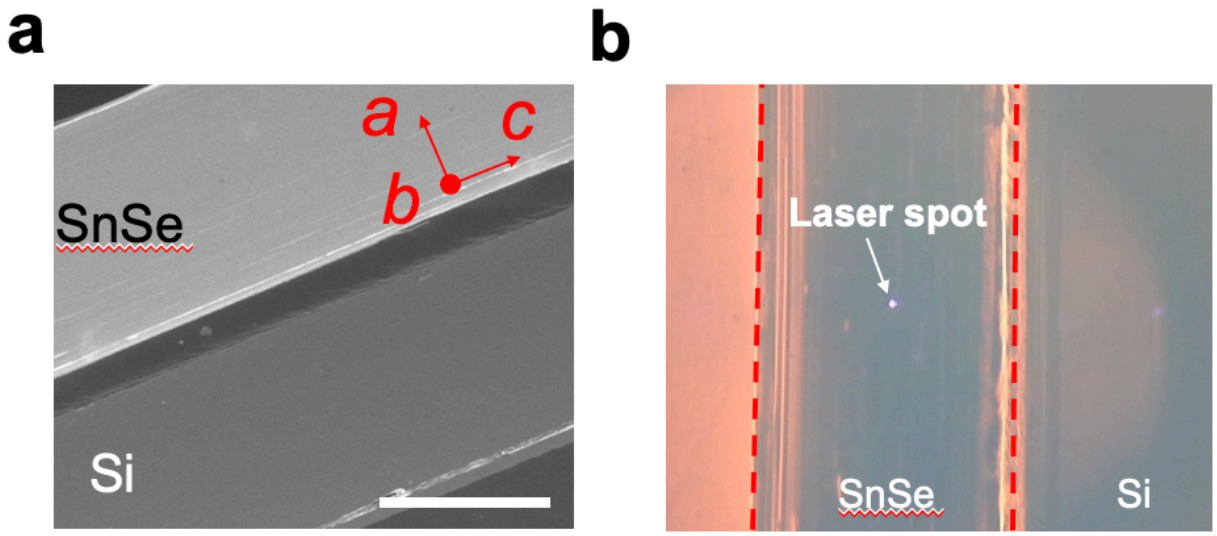

Figure 5.6 *(a) SEM image of polished SnSe sample aligned to b-axis. (b) Optical image of SnSe sample during TDTR measurement. Laser spot indicates measurement volume of thermal conductivity.*

Once the crystalline orientation was determined, the samples aligned along a specific crystal direction were prepared for ultrafast optical-thermal measurements. Fig. 5.6a shows scanning electron microscopy (SEM) images of a sample fabricated with the surface perpendicular to the b-axis. To measure the intrinsic thermal conductivity with minimal phonon scatterings from large-scale disorders, nanoscale optic-thermal measurements were performed using TDTR technique.

The anisotropic thermal conductivity of single-crystal SnSe was carefully measured. Fig. 5.7a shows typical experimental data in which the ultrafast signal (i.e., the time-dependent phase decay) was fitted to the thermal diffusive model[1,36] to measure the thermal conductivity (κ) along

different directions. To evaluate the measurement reliability, 50 different samples were measured along each crystal direction, and the histogram distribution is summarized in Fig. 5.8.

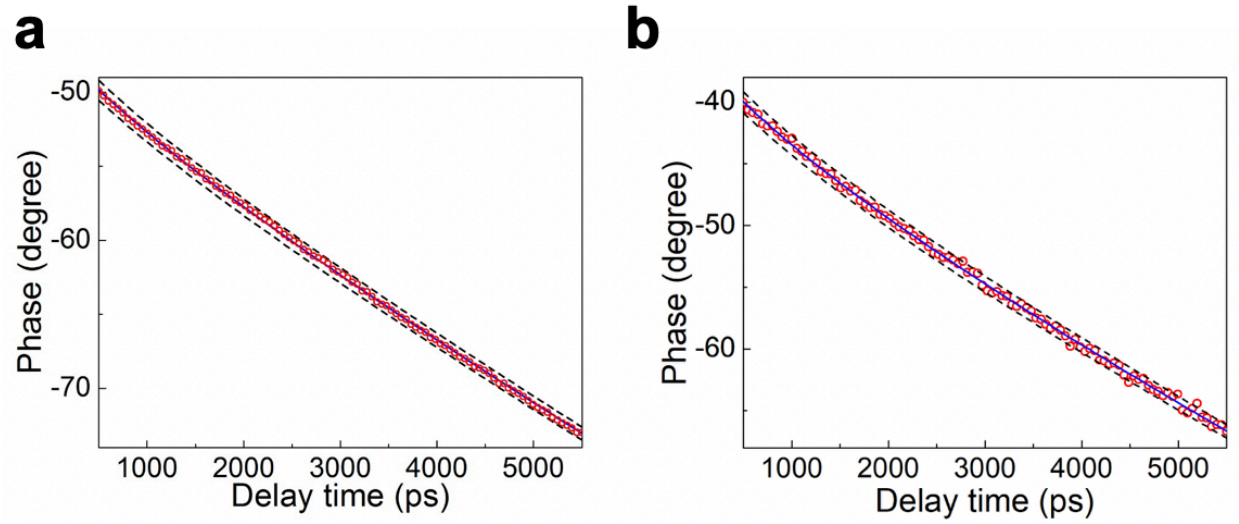

Figure 5.7 *Typical TDTR data: thermal reflectance phase signal versus time (red circles), fitted by the thermal transport model (blue lines). Calculated curves (black dashed lines) using the thermal conductivity changed by ±10% of the best values to illustrate measurement accuracy. (a) a-axis. (b) c-axis*

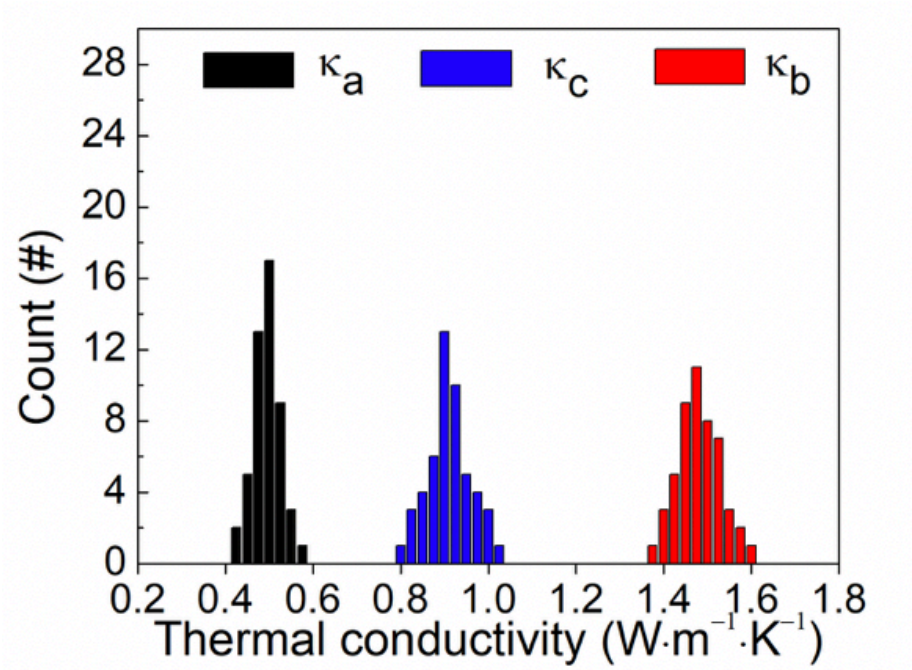

Figure 5.8 *Statistical distribution of thermal conductivity with 50 measurements for each direction.*

The data clearly show that the thermal conductivity of SnSe is highly anisotropic with 1.48 W/mK, 0.91 W/mK and 0.49 W/mK in the b-, c-, and a-axis, respectively. Such a low thermal conductivity was only observed in some amorphous phases with heavy elements or misfit layered 2D compounds with defects. In comparison to other 2D van der Waals materials, such as graphite, transition-metal dichalcogenides, and black phosphorus, the cross-plane thermal conductivity of SnSe is about one-order smaller. It is also about three times smaller than the thermal conductivity of amorphous silicon oxide (1.4 W/mK). To better understand the transport mechanism for this extremely low thermal conductivity, we performed additional measurements on the temperature dependence of thermal conductivity, acoustic velocity, thermal expansion, and the Grüneisen parameter.

The lattice thermal conductivity and phonon relaxation time can be calculated by the kinetic theory which is expressed in equation (3-1) and (3-2). Interestingly, only the anharmonic phonon scattering term (equation (3-5)) is temperature dependent. At the high temperature Debye limit, if the impurity scattering is suppressed in high purity materials so that anharmonic scattering dominates the phonon transport, the thermal conductivity should be proportional to τ_a, i.e. T^{-1} [138].

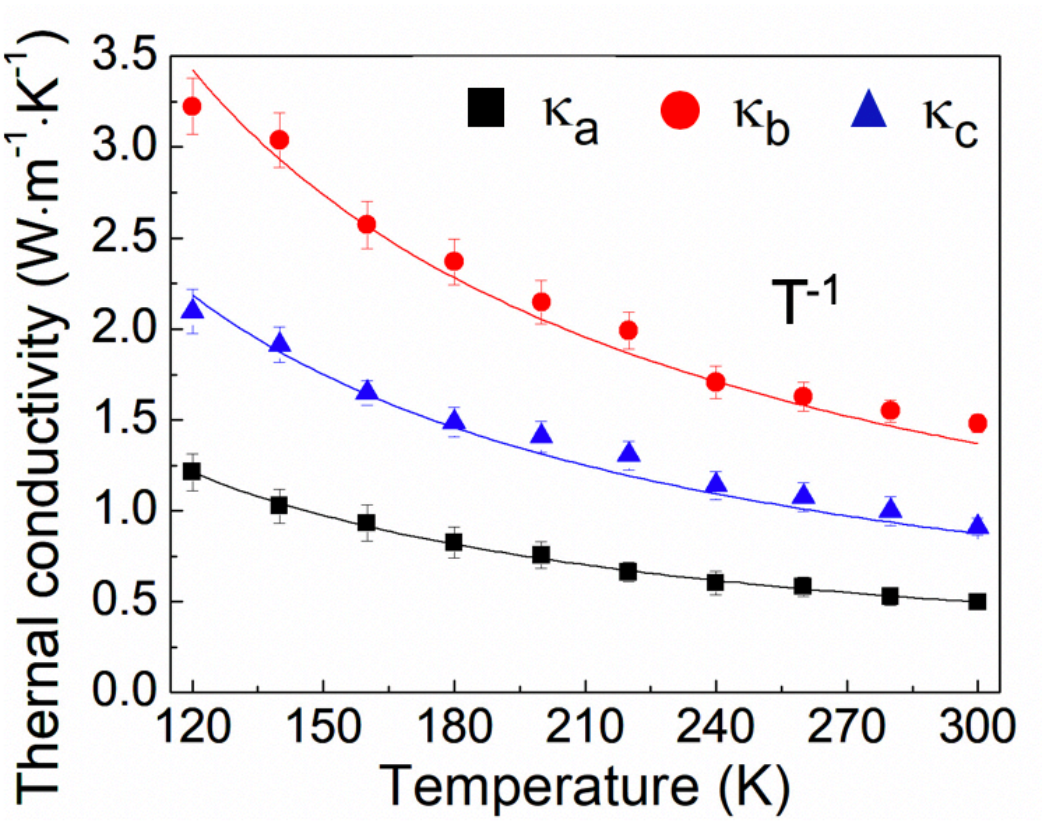

Figure 5.9 *Temperature dependent thermal conductivity from 120 to 300 K.*

The temperature dependent thermal conductivity of SnSe in the three characteristic directions was measured from 120 to 300 K (Fig. 5.6). A guideline of the T^{-1} relationship was directly calculated and plotted along with the experimental data. The good agreement between the experimental and guideline data clearly indicates that the defect and boundary scattering are negligible, which verifies the high quality single-crystal nature of the SnSe samples used. Therefore, in these high-quality SnSe single crystals, anharmonic phonon scattering dominates thermal transport, and the extremely low thermal conductivity indicates strong anharmonicity.

5.4 Phonon anharmonicity and renormalization

To further quantitatively investigate the strong anharmonicity of SnSe, we start to look at the special features and unique physics of high anharmonicity materials from a theoretical point of view. Fundamentally, the phonon picture was following Albert Einstein's seminal idea of using quantized harmonic oscillator to describe atomic vibrations in solids: Phonons are defined as quantized normal modes resulted from harmonic forces between atoms. In most literatures, harmonic models that limited to quadratic terms in the interatomic potential are used to derive phonon frequencies. In this case, the phonon dispersion relation is invariant to temperature. This holds good approximation for most materials, but may not be valid for materials with strong anharmonicity. With non-negligible anharmonic forces, the phonon dispersion will change with temperature, which results in change of sound velocity. To quantify the anharmonicity, we measured the sound velocity at different temperature, and extract the mode-dependent Grüneisen parameter at Brillouin zone centre (Γ point) from the temperature-dependent sound velocity. The mode-dependent Grüneisen parameter (γ_λ)[139] is a key metric to quantify the anharmonicity, which characterizes the relationship between phonon frequency and volume change:

$$\gamma_\lambda = -\frac{V}{\omega_\lambda}\frac{\partial \omega_\lambda}{\partial V} \qquad (5\text{-}1)$$

where $\lambda = (q, j)$ labels a phonon mode with wave vector q and polarization j. ω_λ is the frequency of the mode λ, and V is the volume of the unit cell. Recent controversial literature calculations have reported widely varying values for the Grüneisen parameter— from 0.5 to 6.5[118,126]. Generally, a small Grüneisen parameter value ($\gamma \sim 1$) at the Brillouin zone centre (Γ point: $\omega_\lambda \sim 0$) is expected for most normal materials[140]. At the Brillouin zone centre (Γ), phonon dispersion is linear ($\omega_\lambda = vs \times q$) where the phonon group velocity equals to the speed of sound (v_s). The ω_λ depends on the material volume (V) and the temperature (T) — ω_λ (V, T). The phonon group velocity ($v_{g\lambda}$) are defined by:

$$v_{g\lambda} = \frac{\partial \omega_\lambda}{\partial q_\lambda} \qquad (5\text{-}2)$$

where $q_\lambda = 2\pi\lambda / Na_\lambda$ (a_λ is the lattice constant).

Near the Brillouin zone center, i.e., for small frequency phonons, $v_{g\lambda}$ is independent of the frequency and is equivalent to the sound velocity ($v_{g\lambda}$),

$$v_{g\lambda} = v_g = \frac{\partial \omega_\lambda}{\partial q_\lambda} = \frac{\omega_\lambda}{q_\lambda} \qquad (5\text{-}3)$$

Under constant pressure,

$$\frac{\partial \omega_\lambda}{\partial T} = \frac{\partial (v_g \times q_\omega)}{\partial T} = v_g \frac{\partial q_\lambda}{\partial T} + q_\lambda \frac{\partial v_g}{\partial T} = -v_g q_\lambda \frac{\partial a_\lambda}{a_\lambda \partial T} + q_\lambda \frac{\partial v_g}{\partial T} \qquad (5\text{-}4)$$

$$\frac{\partial \omega_\lambda}{\omega_\lambda \partial T} = -v_g \frac{q_\lambda}{\omega_\lambda}\frac{\partial a_\lambda}{a_\lambda \partial T} + \frac{q_\lambda}{\omega_\lambda}\frac{\partial v_g}{\partial T} = -\frac{\partial a_\lambda}{a_\lambda \partial T} + \frac{1}{v_g}\frac{\partial v_g}{\partial T} = -\alpha_L + \frac{1}{v_g}\frac{\partial v_g}{\partial T} \qquad (5\text{-}5)$$

where α_L is the linear thermal expansion coefficient along the specific crystal orientation.

Therefore,

$$\gamma_\lambda = -\frac{V}{\omega_\lambda}\frac{\partial \omega_\lambda}{\partial V} = -\frac{\partial \omega_\lambda}{\omega_\lambda \partial T} / \frac{\partial V}{V \partial T} = -\frac{\partial \omega_\lambda}{\omega_\lambda \partial T} / \alpha_v \qquad (5\text{-}6)$$

where α_v is the volumetric thermal expansion coefficient. From Equation (S6) and (S7), we have,

$$\gamma_\lambda = \frac{\alpha_L}{\alpha_v} - \frac{1}{\alpha_v v_g}\frac{\partial v_g}{\partial T} \qquad (5\text{-}7)$$

Therefore, the mode-dependent Grüneisen parameter at the Γ point is

$$\gamma_\Gamma = \frac{1}{\alpha_v}(\alpha_L - \frac{1}{v_s}\frac{\partial v_s}{\partial T}) \qquad (5\text{-}8)$$

where the v_s is the sound velocity. In Equation (5-8), γ_Γ contains the thermal expansion induced phonon frequency shifts (i.e. the quasi-harmonic contribution), and a second term of anharmonicity induced frequency shifts. The difference of those two contributions will be further discussed later. Eq. (5-8) enabled us to measure the temperature-dependent *Γ* point Grüneisen parameter γ_Γ for the first time.

Here we developed an experimental approach to directly measure the mode-dependent Grüneisen parameter of the Brillouin zone center at different temperature using picosecond ultrasonic and XRD. Note that most literature are limited to measuring the macroscopic Grüneisen parameter (i.e. weighted average of mode-dependent γ_Γ by heat capacity contributions), or probing Raman shifts for optical branch phonons. To evaluate the temperature effect for the ultralow cross-plane thermal conductivity in single-crystal SnSe, we focused on the longitudinal phonon branch along the a-axis and measured the sound velocity, lattice thermal

expansion, and specific heat from 120 to 300 K. First, the longitudinal sound velocity was measured using ultrafast pulse-echo measurement.

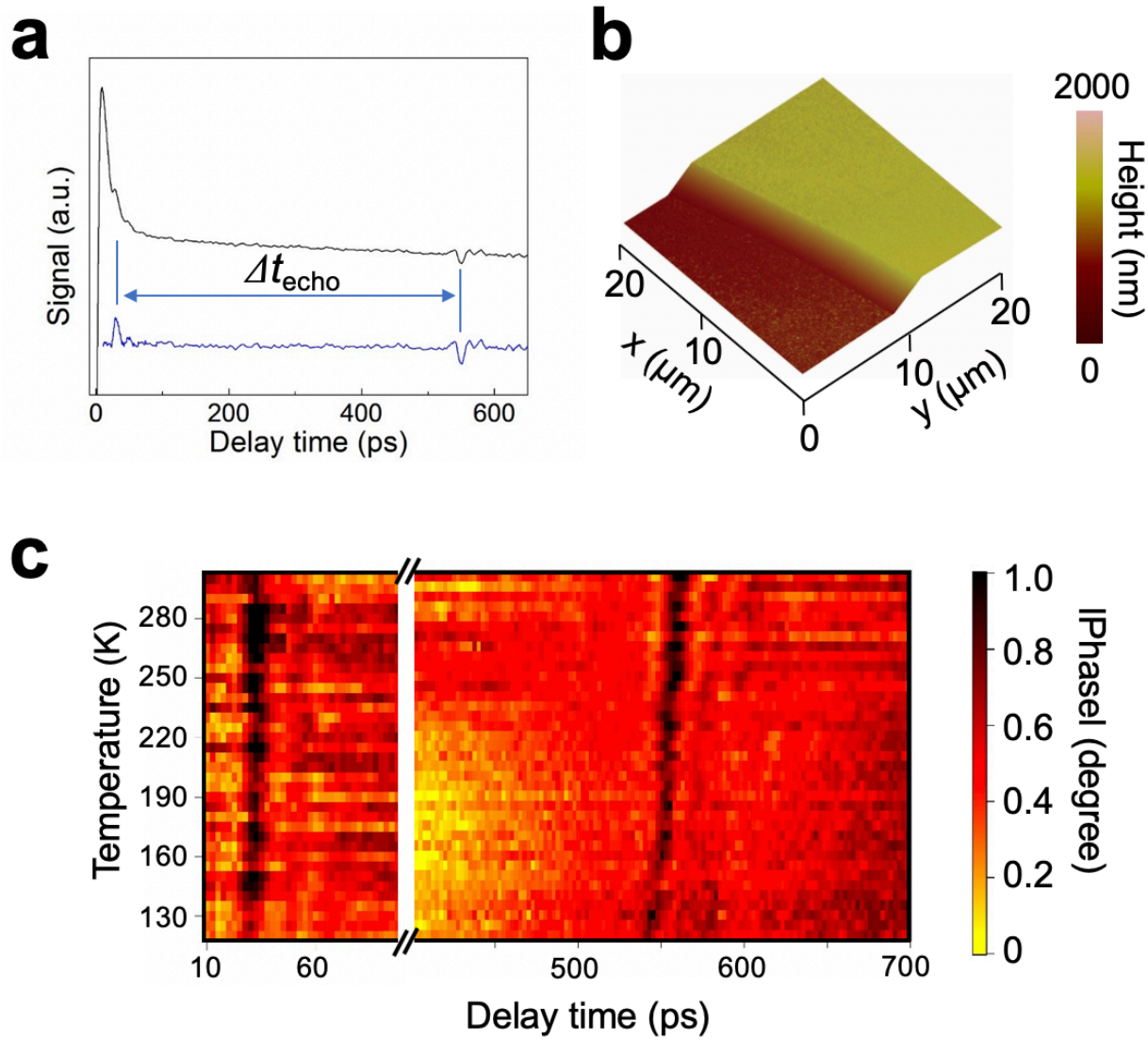

Figure 5.10 *(a) Picosecond laser ultrasonic data along the a-axis. The interval (Δt_{echo}) between the peak and valley echoes is the time for a round trip of the acoustic wave inside the SnSe sample. b) Atomic force microscopy image of a thin film SnSe sample, measuring the sample thickness of 884 nm. d) Two-dimensional mapping of the temperature dependent ultrasonic data along a-axis of SnSe from 120K to 300K*

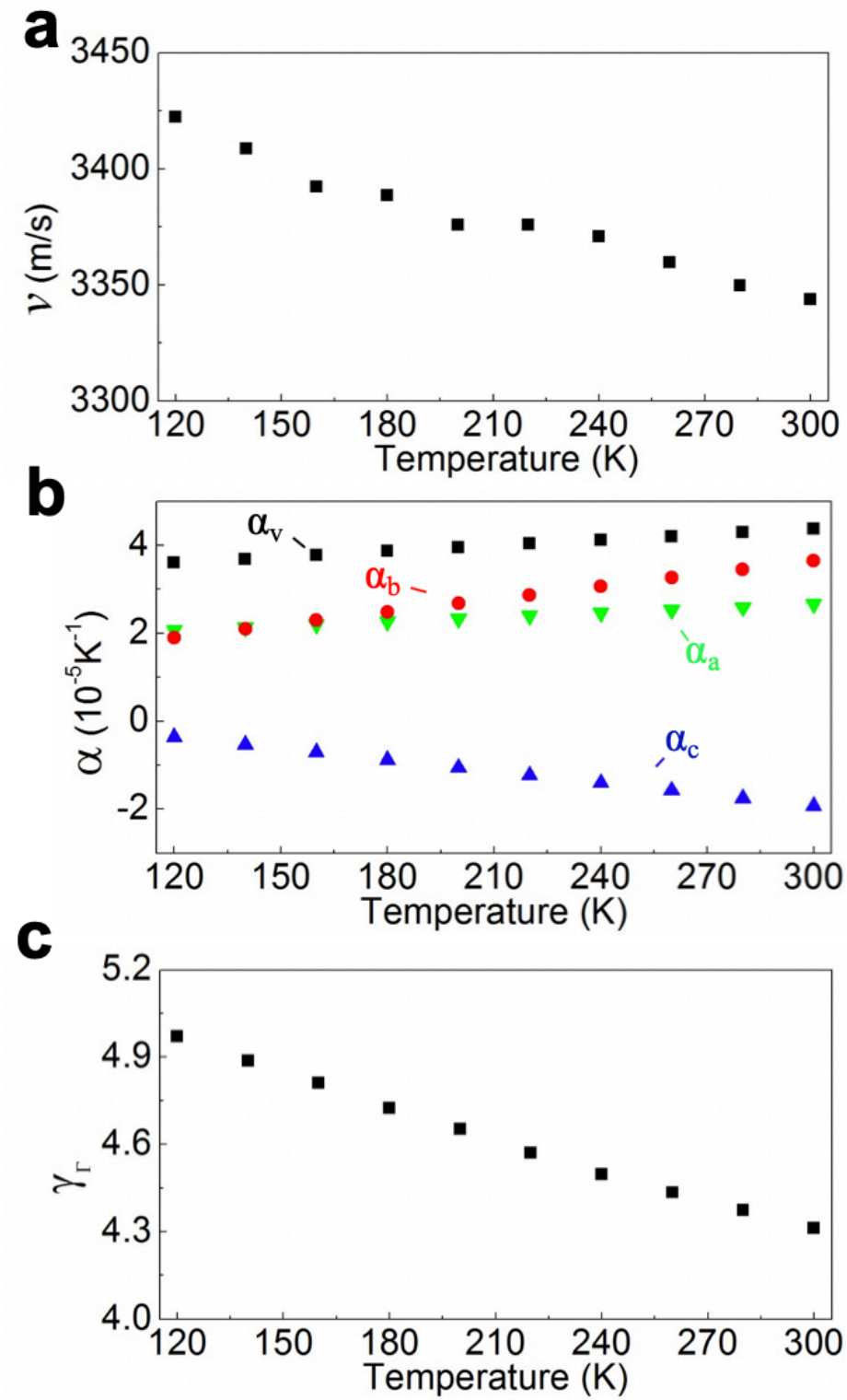

Figure 5.11 *(a) Temperature dependent longitudinal sound velocity (a-axis) of SnSe. (b) Linear and volumetric thermal expansion coefficients in each direction. c) Temperature dependent Grüneisen parameter (γ_Γ) of SnSe.*

For longitudinal sound velocity measurement, exfoliated SnSe films were transferred on a SiO_2 substrate, and sample thickness was measured by atomic force microscopy (AFM) (Fig. 5.10b). The evolution of the PLU signal between temperatures of 120 to 300 K was plotted as a 2D map (Fig. 5.10c), and clearly shows that Δt_{echo} is reduced at low temperature. The sound velocity was measured from 3343 m/s at 300 K to 3422 m/s at 120K (Fig. 5.11a). These measurements show a significant 2.4% change in temperature-dependent sound velocity (thus the phonon dispersion relation) of SnSe in comparison with other common materials (for example, 0.46% for silicon). In addition, the measured sound velocity of SnSe is actually over 50% larger than that predicted from the density functional theory (DFT) (2117 m/s)[118]. Next, we directly measured the volumetric and linear thermal expansion coefficients along each crystal orientation of the SnSe lattice, using temperature dependent XRD (Fig. 5.11b). Finally, using Eq. (5-8), we extracted the temperature dependent Γ point Grüneisen parameter (Fig. 5.11c).

From the measurement (Fig. 5.11c), a strong temperature effect was observed for γ_Γ. The measured γ_Γ is 4.31 at room temperature and increases to 4.97 at 120 K, which indicates a very strong phonon anharmonicity. Such an experimental observation has important insights to the state-of-the-art phonon theory calculations. Mathematically, the interatomic potential (U) of a crystal can be expanded with respect to atomic displacements from the equilibrium positions of atoms,

$$U = U_0 + \frac{1}{2}\frac{\partial^2 U}{\partial r_i^\alpha \partial r_j^\beta} u_i^\alpha u_j^\beta + \frac{1}{3!}\frac{\partial^2 U}{\partial r_i^\alpha \partial r_j^\beta \partial r_k^\gamma} u_i^\alpha u_j^\beta u_k^\gamma + \frac{1}{4!}\frac{\partial^2 U}{\partial r_i^\alpha \partial r_j^\beta \partial r_k^\gamma \partial r_l^\delta} u_i^\alpha u_j^\beta u_k^\gamma u_l^\delta + \cdots \quad (5\text{-}9)$$

Where U_0 is the interatomic potential at the equilibrium, r_i^α denotes the coordinate of the i-th nucleus along Cartesian direction α and u_i^α denotes the atomic displacement from equilibrium

position. The n-th order derivative of the interatomic potential with respect to displacement is the interatomic force constants (IFCs).

Most current theoretical methods generally use the harmonic (HA) model,

$$D(q)e_q = \omega_q^2 e_q \qquad (5\text{-}10)$$

where e_q and ω_q are the phonon eigenvector and phonon frequency corresponding to the phonon wave vector q. $D(q)$ is the dynamical matrix determined by second-order IFCs and atomic masses. HA only considers the parabolic expansion of interatomic potential, where forces acting on each atom linearly response to the atomic displacements (Fig. 5.12a).

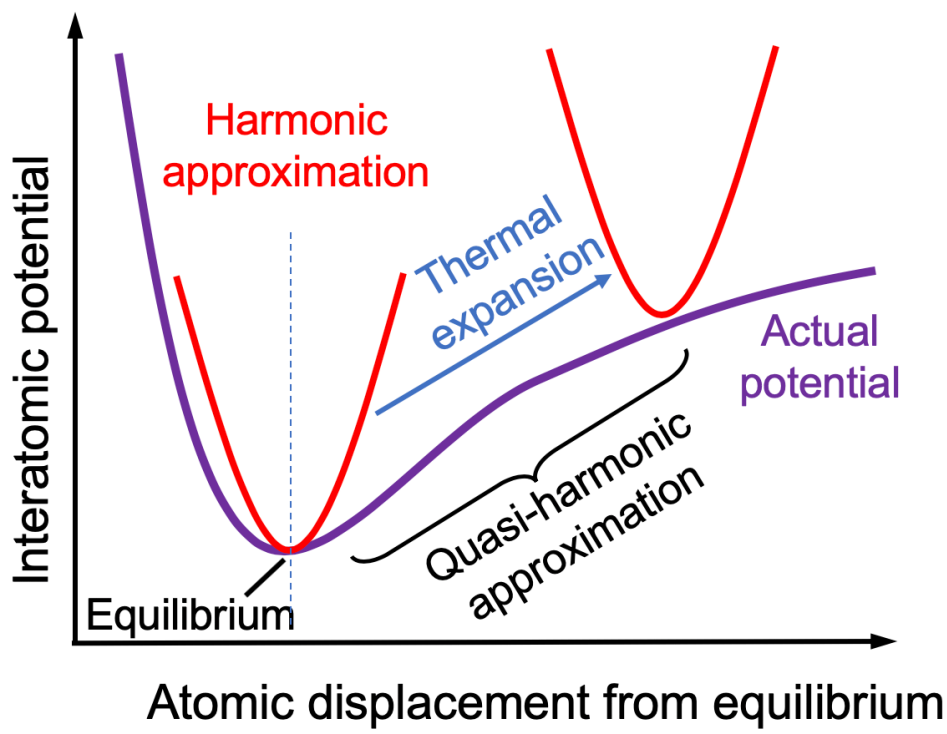

Figure 5.12 *(a) Schematic of interatomic potential as a function of atomic distance, illustrating HA and QHA*

Combined with the DFT calculated second-order IFCs, HA can precisely predict the phonon dispersion for 0 K, but neglects the temperature effect. However, the phonon frequency will shift with the increase of temperature. The decrease of phonon frequency with increasing temperature is called phonon softening effect, and the opposite is called phonon hardening. In general, phonon frequency shift is contributed by two mechanisms: the thermal expansion and the intrinsic anharmonicity.

Thermal expansion stems from the change of interatomic potential. With the rising of temperature, the lattice usually expands due to the change of interatomic potential, thereby shifts the phonon frequency. Quasi-harmonic model (QHA) covers the frequency shift due to thermal expansion[98,141] (Fig. 5.12a),

$$\Delta\omega_{\lambda}^{QHA} \approx -\omega_{\lambda}^{0}\gamma_{\lambda}\int_{0}^{T}\alpha_{v}(T)\,dT \qquad (5\text{-}11)$$

where $\lambda = (q, j)$ labels a phonon mode with wave vector q and polarization j. ω_{γ}^{0} and $\Delta\omega_{\gamma}^{QHA}$ are the 0 K phonon frequency and quasi-harmonic frequency shift of phonon mode λ respectively. γ_{λ} is the gruneisen parameter of phonon mode λ. α_{v} is the volumetric thermal expansion coefficient at different temperature. Besides the frequency shift, the change of wavevector q due to thermal expansion is also considered in this work.

QHA is plausible in most materials, especially, at low and moderate temperatures owing to small phonon populations. However, for strongly anharmonic materials, the intrinsic anharmonicity due to the cubic, quartic and higher-order terms of the interatomic potential, can cause strong interaction and energy exchange between normal modes, and thereby introducing nontrivial temperature-dependent phonon renormalization, which are not accounted for by QHA. For SnSe, the measurement (Fig. 5.11) shows that the temperature-driven change in phonon dispersion (the 2nd item in Equation 5-8) contributes to over 90% of the total changes in phonon

frequencies. This very strong phonon softening effect, not fully accounted for by thermal expansion, indicates that the quasi-harmonic model may not be appropriate for SnSe. At room temperature, such a strong lattice softening is only observable when a phase change of the material is approached, but usually not for a single material phase[142]. At high temperature ~ 1500 K, a recent measurement using inelastic neutron scattering shows consistent phonon shifts in silicon[143]. Therefore, the measured temperature effect here suggests a re-examination of the ubiquitous theory models[139] for SnSe at room temperature and even below.

To take account the phonon softening due to intrinsic anharmonicity, we apply self-consistent phonon theory[144–146] to calculate the frequency shift, i.e. anharmonicity (AH) model. Essentially, back to the original phonon picture following the idea of using quantized harmonic oscillators to describe atomic lattice vibrations, the AH accounts interactions and energy exchange between the normal quantization modes[139]. There are two theories to consider the anharmonic effect to phonon frequency shift, perturbation theory and self-consistent phonon theory. Within perturbation theory[147–152], the anharmonic correlation is far smaller than the harmonic frequency, the frequency shift due to anharmonicity is given by the real part of self-energy as $\Delta\omega_{\lambda}^{AH} = -\frac{1}{\hbar} Re\, \Sigma_{\lambda}$, where Σ_{λ} is the self-energy of phonon mode λ. However, when the anharmonic terms is very large, a non-perturbative self-consistent phonon theory[153,154] should be applied, where the anharmonic phonon frequencies $\{\Omega_{\lambda}\}$ and harmonic phonon frequencies $\{\omega_{\lambda}\}$can be linked as

$$\Omega_{\lambda}^{2} = \omega_{\lambda}^{2} + 2\Omega_{\lambda} I_{\lambda} \qquad (5\text{-}12)$$

where I_{λ} is associated with fourth-order IFCs if only considering the first-order self-energy,

$$I_{\lambda} = -\sum_{\lambda_1} \frac{\hbar\Phi_4(\lambda;-\lambda;\lambda_1;-\lambda_1)}{4\Omega_{\lambda}\Omega_{\lambda_1}} \frac{2n_1(\Omega_{\lambda_1})+1}{2} \qquad (5\text{-}13)$$

where $\Phi_n(\lambda;\lambda_1;\cdots;\lambda_n)$ is the reciprocal representation of the n-th IFCs. ω_λ is the phonon frequency of phonon mode λ, and $-\lambda = (-q, j)$. n_1 is the Bose-Einstein distribution function for phonon mode λ_1. Since the high-order self-energy is usually much smaller than the first-order self-energy, we only consider the first-order self-energy in this paper.

Note that prior work has observed strong anharmonicity in SnSe[126,133–135]. However, most calculations were using parabolic interatomic potential or QHA. Here, we include high-order anharmonic contributions to calculate the temperature-dependent phonon dispersion of SnSe in the AH model[155]. Our *ab initio* calculation on temperature dependent phonon dispersion of SnSe can be divided into three steps. First, density functional theory (DFT) was applied to find an optimized equilibrium structure with force acting on each ion less than 10^{-4} eV/Å. Second, the second and fourth order IFCs were calculated by finite displacement method. We built a 144 atoms supercell, generated irreducible sets of displacement using ALAMODE package, calculated the force acting on each ion by DFT, and derived IFCs based that. For the 3rd order IFCs, we consider up to 8th nearest neighboring atoms for Sn atoms and up to 5th nearest neighboring atoms for Se atoms. For 4th order IFCs, we consider up to 4th nearest neighboring atoms for both Sn atoms and Se atoms. The DFT calculations are accomplished using Quantum ESPRESSO[58,59]. For all the DFT calculations, we used projector augmented-wave pseudopotential with local density approximation[156], and the electronic wave functions were expanded in plane-wave basis with kinetic energy cutoff at 544 eV. We used 4 × 6 × 6 Monkhorst-Pack k-points meshes to sample the Brillouin zone for structure optimization, and 2 × 2 × 2 Monkhorst-Pack k-points meshes for IFCs calculation. Third, we solved Eq. (5-11) using ALAMODE package[145] to get temperature dependent dispersion relation of SnSe.

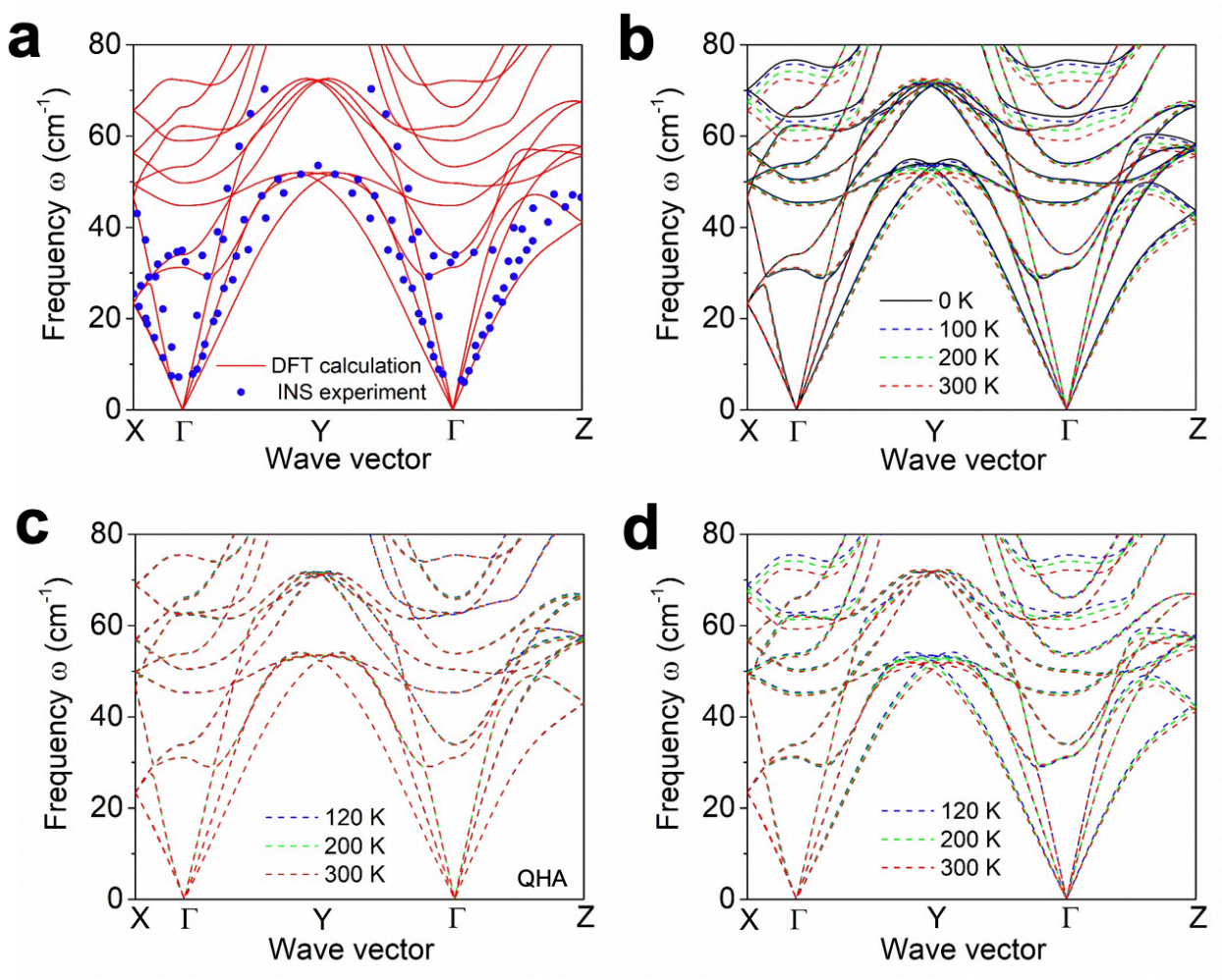

Figure 5.13 *Ab initio calculations of temperature-dependent phonon band structures of SnSe using harmonic approximation (HA), quasi-harmonic approximation (QHA), and anharmonicity approximation (AH). (a) Phonon dispersion relation of SnSe at 300 K from density functional theory (DFT) in comparison with experimental data from inelastic neutron scattering (INS). (b-d) Temperature-dependent phonon band structures using different models: (b) AH only considering the anharmonicity, (c) QHA only considering the thermal expansion, (d) AH + QHA model considering both anharmonicity and thermal expansion.*

Figure 5.13 displays our ab initio calculation results considering different mechanisms. Figure 5-9b shows the DFT calculated phonon dispersion in good agreement with inelastic neutron scattering experiment[134]. The calculation results of the phonon dispersions at different temperatures are shown in Figure 5.13b-d, with the comparison between HA, QHA, and AH.

Figure 5.13b shows the temperature dependent phonon dispersions from anharmonic models (ω_λ^{AH}). In Figure 5.13c, we calculate the quasi-harmonic frequency shift from 120 K ($\Delta\omega_\lambda^{QHA}$), based on our measured volumetric thermal expansion coefficient α_V from 120 K to 300 K and first-principles calculated mode dependent Gruneisen numbers. We take the phonon dispersion from anharmonic model at 120 K as the starting point for QHA calculation. While a decrease in phonon frequency with increasing temperature is observed in both models, it clearly shows that the AH has a stronger effect than QHA. Combining both QHA and AH effects, i.e. $\omega_\lambda^{Total} = \Delta\omega_\lambda^{QHA} + \omega_\lambda^{AH}$, the phonon dispersion is updated in Figure 5.13d.

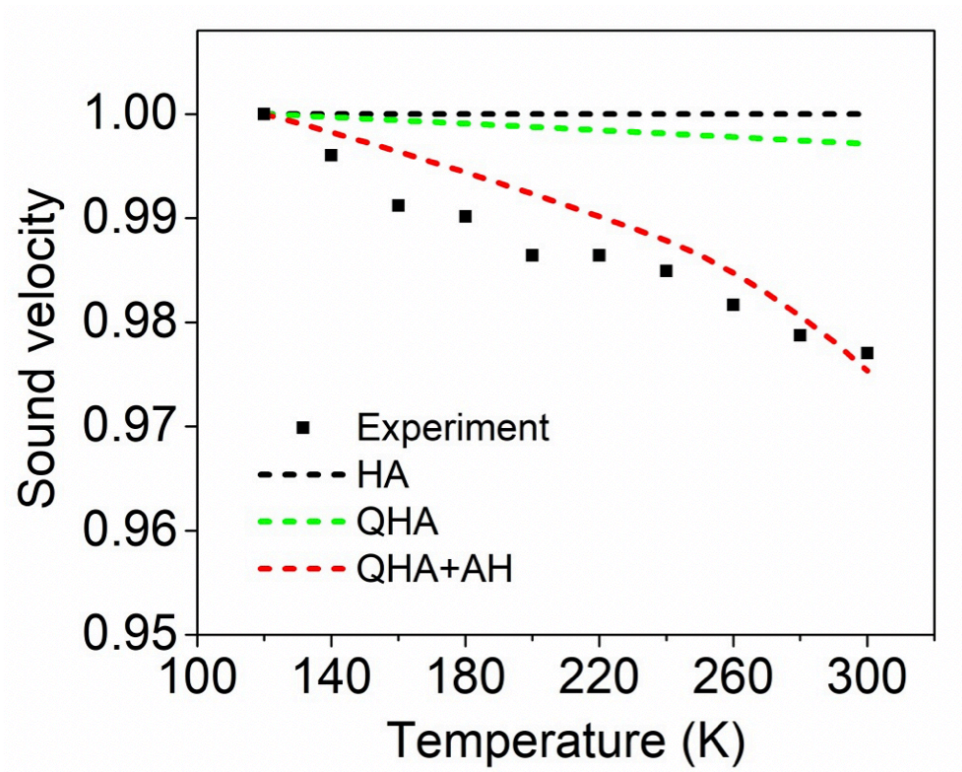

Figure 5.14 *The ab initio predictions of temperature dependent sound velocity of SnSe from different models, in comparison with experimental data. For illustration clarity, the sound velocity is normalized at 120 K. The HA result is independent with temperature; QHA shows weak dependence on temperature, while AH shows a strong temperature dependence comparable with experiment.*

Furthermore, in Figure 5.14, the longitudinal cross-plane sound velocity (v) of SnSe is extracted and plotted in comparison with our experimental data shown in Figure 5.11a. In HA, the sound velocity is independent from temperature. In QHA, the sound velocity is changed with temperature only due to thermal expansion and for SnSe, the temperature dependence of sound velocity within QHA is much weaker than experiment. After including the AH, a much stronger temperature dependence in sound velocity is predicted from 120 to 300 K, consistent with our experimental measurement. Therefore, this study verifies the failure of QHA for SnSe even below room temperature and confirms the importance of high-order anharmonic effects in understanding its thermal properties.

5.5 Summary

In summary, we performed nanoscale anisotropic thermal transport on truly dense SnSe single-crystals and measured their intrinsic thermal conductivity to be highly anisotropic. Our temperature dependent data from 120 to 300 K verifies that the anharmonic phonon scattering dominates transport in high purity single crystals. Furthermore, we successfully measured the temperature dependent acoustic velocity, thermal expansion coefficient, and the Grüneisen parameter at the Brillouin zone center using Picosecond Laser Ultrasonics and XRD. We also performed ab initio calculations of phonon band structures using harmonic, quasi-harmonic, and anharmonic models. Our experimental study and modelling based on self-consistent theory show a very strong temperature-dependent intrinsic anharmonicity in SnSe at room temperature or below, and indicates that the harmonic and quasi-harmonic models that are widely used in the current phonon calculations are not applicable to SnSe. Our study represents a significant

research benchmark for high-performance thermal materials, and establishes a fundamental insight to improving the ab initio calculations for modern phonon transport theory.

CHAPTER 6

*In situ thermal conductivity modulation in layered material**

6.1 Introduction

In this chapter, I demonstrate *in situ* thermal-electrochemical characterization of a 2D van der Waals material in a lithium ion battery. A novel approach to integrate ultrafast optical spectroscopy and electrochemical control has been developed to investigate the thermal transport in the 2D material electrode (black phosphorus) during the battery's normal operation process. The study reveals intriguing anisotropic ion-phonon interactions and highly reversible electrochemical control over the thermal properties.

6.2 Material growth and structural characterization

High-quality black phosphorus (BPh) is synthesized by chemical vapor transport method with mineralization additives. Amorphous red phosphorus, Tin, and Tin iodide (99.99+% purity, from AlfaAesar) are used black phosphorus growth. We use 500mg of red phosphorus, 10mg of tin powder, and 10mg of tin iodide for each growth. Mixture of these chemicals are placed into a quartz tube. The quartz tube is evacuated, and flame sealed under high vacuum (10^{-5} torr). The quartz tube is placed into reaction furnace and heated up to 873 K and held on the temperature for 1 days, then slowly cool down to room temperature.

(*The work described in this chapter was done in collaboration with M. Ke and was the basis for the article published on *Nano Lett.,* 2017, 17 (3), 1431–1438.)

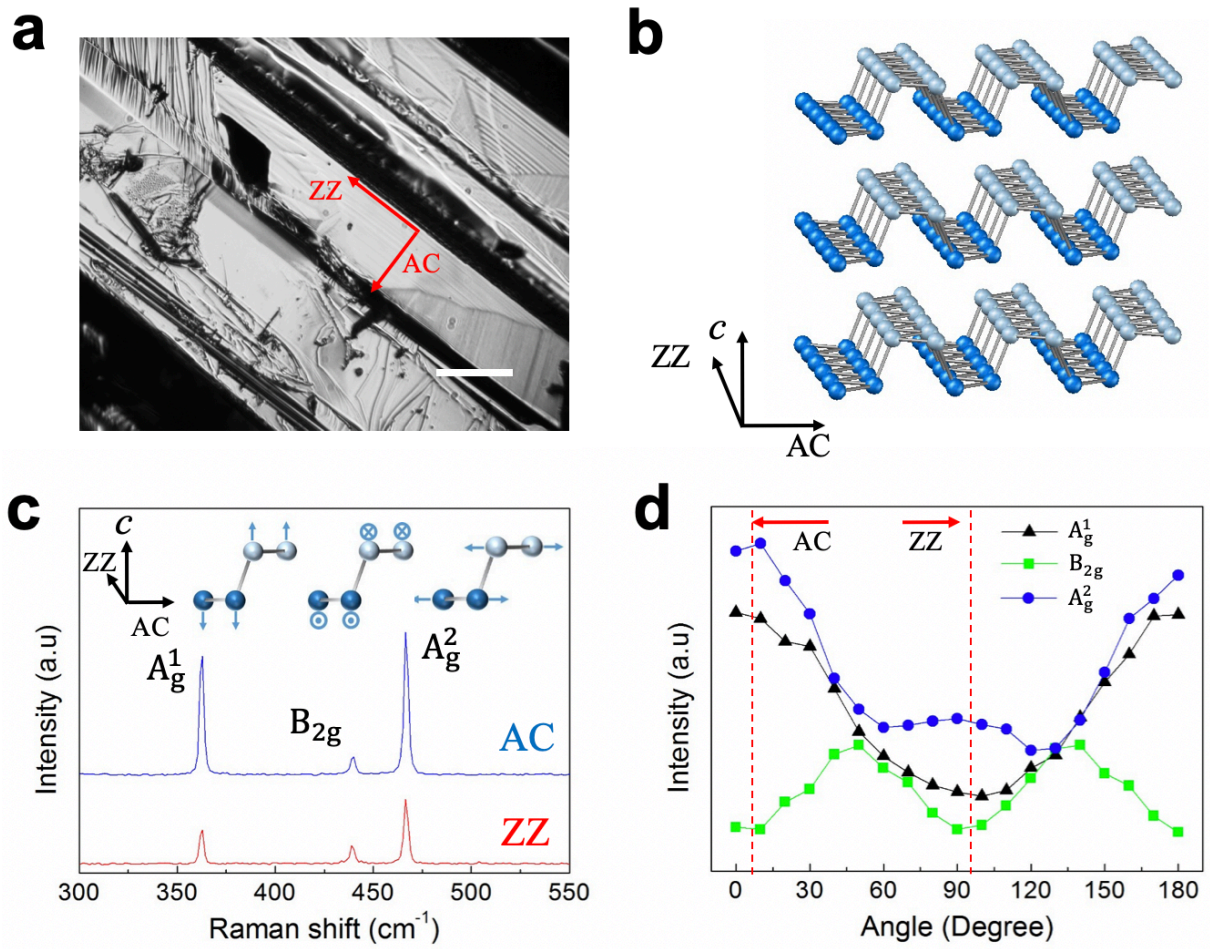

Figure 6.1. *Crystal structure and material characterization of BPh. (a) Optical image of BPh. The ZZ and AC direction is marked in the figure. The scale bar is 200μm; (b) Schematic of BPh. The phosphorus atoms on the top and bottom plane are indicated as light blue and dark blue respectively; (c) Angle-dependent Raman spectroscopy of pristine BPh. The blue and red lines is Raman shift which the laser is polarized with AC and ZZ direction, respectively. The inset figure is phonon vibration mode related with each* A_g^1, B_{2g}, *and* A_g^2 *peaks; (d) Raman intensity plot of* A_g^1, A_g^2, *and* B_{g2} *peaks as a function sample angle with parallel polarized beam. The blue, black, and green line represent angle-dependent* A_g^1, A_g^2, *and* B_{g2} *intensities, respectively. The red dash lines indicate the AC and ZZ direction.*

Next, for thermal conductivity measurement, BPh film with a clean surface was prepared by mechanically exfoliating a BPh crystal. Fig. 6.1a shows the optical image of an exfoliated BPh. This semiconducting BPh is a layered material with a puckered orthorhombic crystal

structure [157] (Fig. 6.1b). Each layer includes two kinds of P-P bonds: the shorter bond connects the nearest P atoms in the same plane, and the longer bond connects P atoms in the top and bottom planes. Therefore, each P atom forms three covalent bonds mainly from 3p orbitals, and the interlayer interaction is based on van der Waals forces. Such a unique anisotropic crystal structure leads to anisotropic physical properties and is usually discussed based on three characteristic directions: the armchair (AC), zigzag direction (ZZ), and cross-plane (c) directions (Fig. 1b).

To identify the crystalline orientation and orient the BPh sample for the following measurement, an angle-resolved, polarized Raman spectroscopy was performed. BPh crystal has a D_{2h}^{18} point group and six active Raman vibration modes [158]. Under laser excitation along the c-plane, only three vibration modes will be detected due to the symmetric selection rule [158,159]. Figure 6.1c clearly shows that three active Raman peaks have been measured: A_g^1 (363 cm^{-1}), B_{2g} (440 cm^{-1}), and A_g^2 (467 cm^{-1}), and their corresponding vibration modes are illustrated in the schematic. The intensity of these Raman peaks depends on the alignment between the Raman polarization and the crystal orientations [159]: The A_g^2 peak intensity reaches the maximum when the Raman polarization is along the AC direction; while the B_{2g} peak is of the maximum intensity when Raman polarization is right in-between of the AC and ZZ directions. Figure 6.1d shows the relative intensity of each Raman peak with its associated angle-dependence. From this measurement, the AC and ZZ directions of BPh samples are determined and marked down in Fig. 6.1d. In fact, the ZZ crystalline orientation corresponds to the stripe features naturally formed in the exfoliated BPh (Fig. 6.1a). In addition, no difference has been observed for Raman spectra performed at different spots of BPh samples up to centimeter sizes, which indicates a very high crystalline quality and uniformity of these BPh samples.

6.3 Thermal properties measurement of pristine black phosphorus

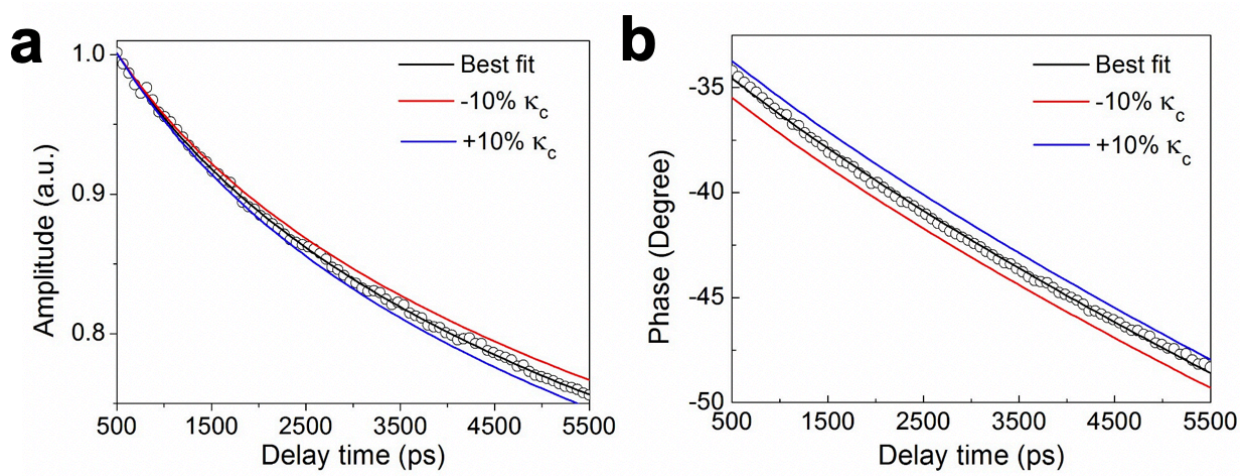

Figure 6.2. *Ultrafast pump-probe spectroscopy for measuring anisotropic thermal properties of pristine black phosphorus. Experimental measurement data and model fitting using both the (a) amplitude and (b) phase signals. Experimental data (black circles) and fits from the multilayer thermal transport model (black lines) for both the amplitude and phase signal. Calculated curves (red and blue lines) using the thermal conductivity changed by ±10% of best values are plotted to illustrate the measurement sensitivity.*

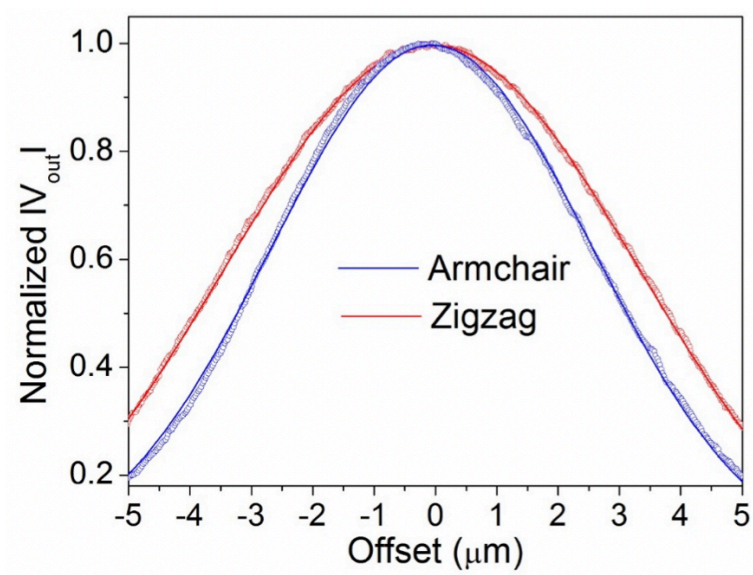

Figure 6.3. *In-plane thermal transport measurement of black phosphorus. Experimental data (circles) and fits from thermal transport model. The red color and blue color represent measurement in the armchair and zigzag direction respectively.*

The thermal property of BPh was characterized using TDTR technique [24,160]. The cross-plane thermal conductivity is measured by conventional TDTR method and in-plan thermal conductivity is measured by BO-TDTR. The cross-plane thermal conductivity (κ_c) of pristine BP was measured first. The experimental data from our TDTR measurement and fittings based on amplitude and phase signals are shown in Fig. 6.2a and 6.2b, respectively. The amplitude and phase measurement demonstrated excellent agreement with each other and measured $\kappa_c = 3.86 \pm 0.41$ $W \cdot m^{-1} \cdot K^{-1}$. Such agreement is also confirmed by the sensitivity analysis of amplitude and phase measurement signals under present experimental conditions, indicating both fittings are reliable. Note that, for the fitting of anisotropic materials, the anisotropic ratio of an in-plane thermal conductivity to a cross-plane conductivity is included in the thermal model. The cross-plane analysis was performed iteratively with the in-plane analysis. Typical experimental data from our BO-TDTR measurement and fittings are shown in Fig. 6.3. We used κ_c and interface conductance obtained from cross-plane measurement to extract κ_{ZZ} and κ_{AC}. The in-plan thermal conductivity (κ_{ZZ} and κ_{AC}) are measured at fixed delay time (-50 ps) and 1.5MHz modulation frequency. We use small beam radius (1.85 μm) for in-plan measurement with ×50 objective lens. The beam diameter is measured with both knife-edge beam profiler (BP-209VIS) and TDTR signal at short positive probe delay time (+50ps) with high modulation frequency (9.5MHz). Pump beam is swept by motorized piezo-mirror mount (Newport model 8809) with 0.7 μrad of step resolution, or corresponding to a spatial resolution down to 2 nm on the sample surface. During measurement, we double checked laser conditions, including spot size, beam alignment offset and power, and made sure these parameters are not changing along the delay stage. The V_{out} signal is recorded by lock-in amplifier and thermal model fitting is performed to extract the FWHM of V_{out} signal. The FWHM is converted to in-plane κ by thermal conductivity

tensor model[6]. For in-plane fitting, the cross-plane thermal conductivity and interface conductance is included in the thermal model. The in-plane analysis was performed iteratively with the cross-plane analysis. The measured in-plane κ of pristine BP are κ_{ZZ} = 85.80 $W \cdot m^{-1} \cdot K^{-1}$ and κ_{AC} = 27.58 $W \cdot m^{-1} \cdot K^{-1}$. The measured thermal conductivity of pristine BP is consistent with results in recent independent studies [7–9].

6.4 Device fabrication for *in-situ* thermal conductivity measurement

To enable the *in-situ* measurement and control of the thermal property of BPh, we developed a novel electrochemical device platform (Fig. 6.4). The internal structure of our device represents a planar lithium ion battery configuration, where BPh and lithium metal serve as the cathode and anode electrode respectively.

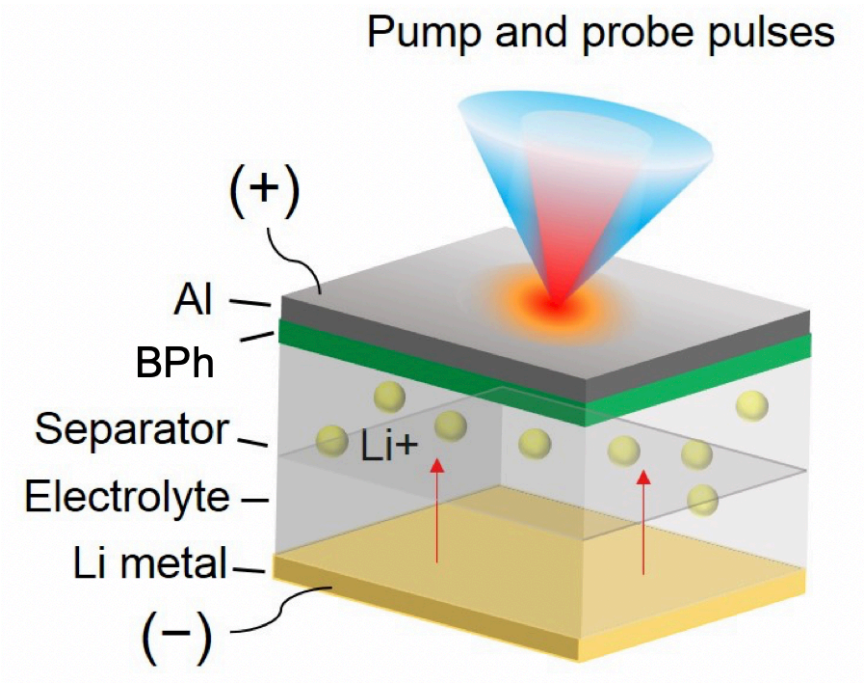

Figure 6.4. *In-situ thermal conductivity measurement setup of BPh. Electrochemical platform for in-situ thermal conductivity measurement.*

The coin cell battery was fabricated completely in standard argon-rich glovebox. A millimeter-sized window was opened on the CR2032 coin cell case for the TDTR measurements. The window was closed with quartz and completely sealed with chemically inert epoxy. To ensure efficient lithium intercalation, channel openings are made between the BP layers and copper current collector. The BP cathode was placed on top of the platform. Electrolyte (1M $LiPF_6$ in 1:1 w/w ethylene carbonate/diethyl carbonate from Sigma Aldrich) were added onto the BP and then the separator and lithium anode were stacked with the cathode. A spacer and a spring were added before the coin cell was closed and sealed with epoxy. The sealing condition was tested to ensure the batteries function properly after several months after fabrication without chemical degradation. Figure 6.5 shows that device fabrication sequence used in this research.

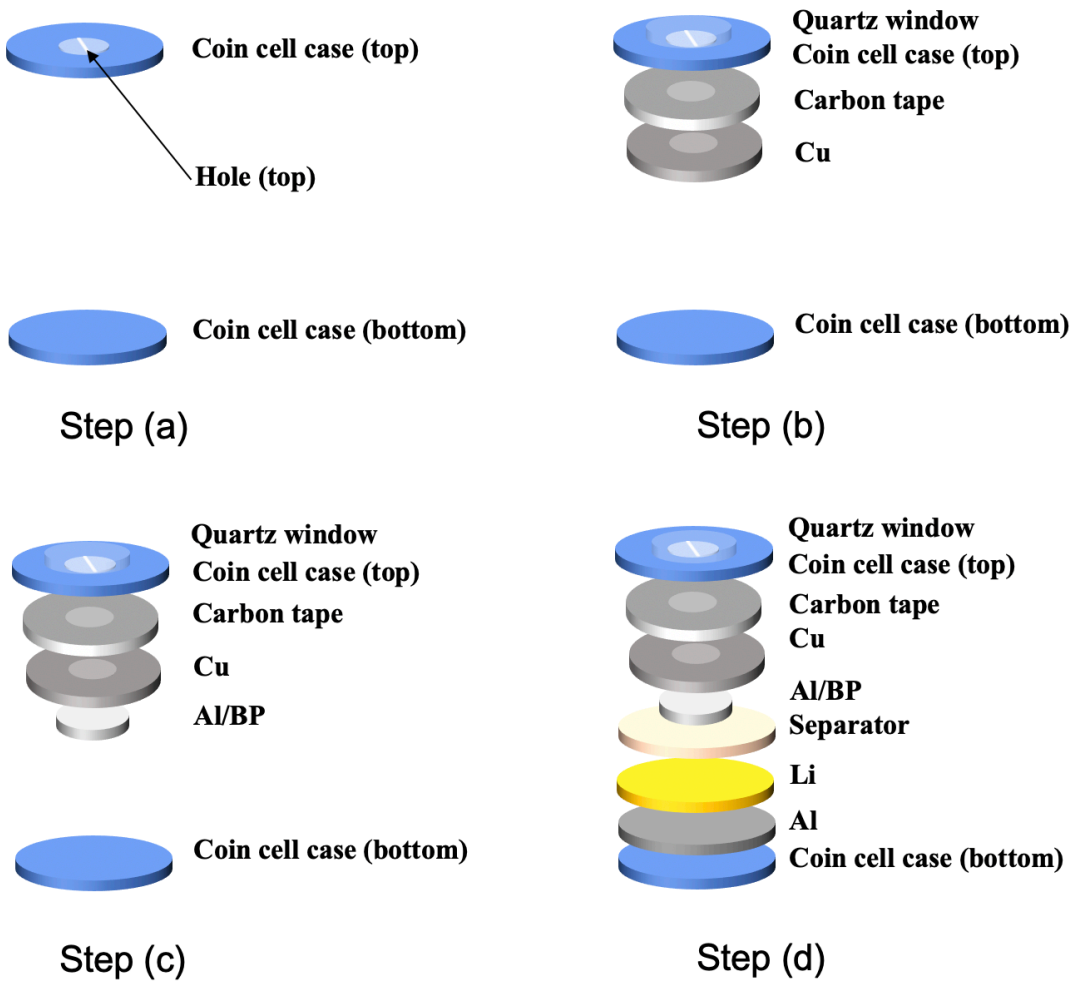

Figure 6.5. *Schematics and fabrication sequence of in-situ electrochemical device for in-situ measurement.*

During the device operation (i.e., a battery discharging/charging process), the intercalation of Li atoms into and out from the interlayer spacing of the BPh electrode is controlled using a BioLogic VSP-300 electrochemical workstation. The whole device with electrolyte was sealed inside a standard metal coin cell case to maintain the chemical stability. In addition, an optically transparent quartz window (1 mm × 1mm) was fabricated on the metal case to allow *in-situ* TDTR spectroscopy to probe the BPh surface while simultaneously controlling the ionic intercalation.

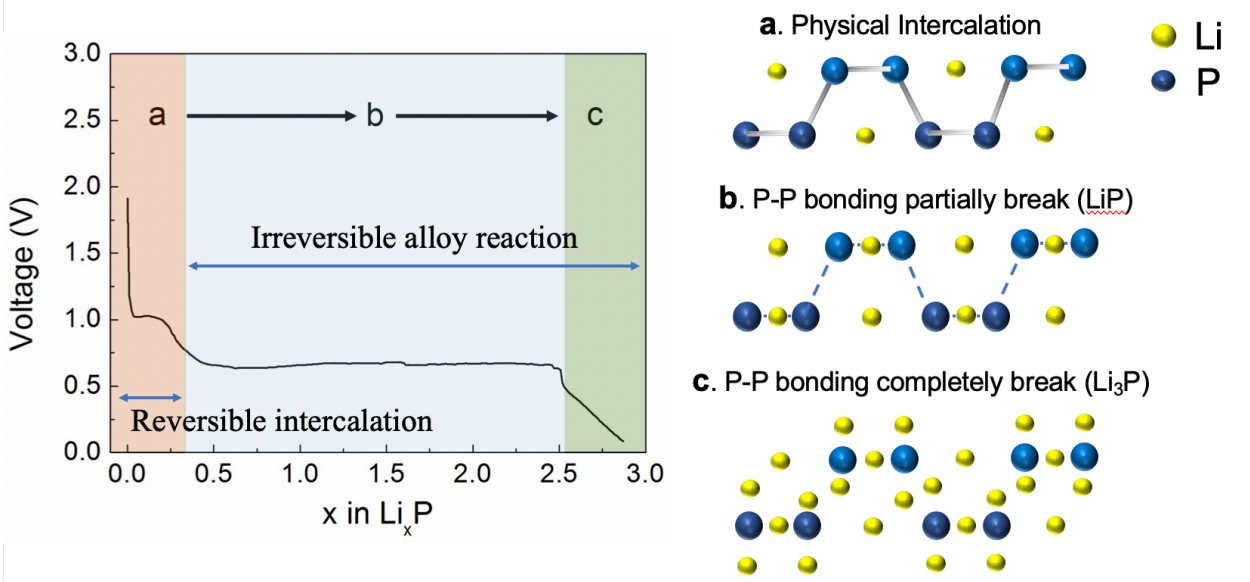

***Figure 6.6**. Galvanostatic discharge curve of a BPh-lithium battery. The different background colors indicate the phase changes that occur during lithiation. The red, blue, and green background indicate different phases for Li_xP when x <1, x=1, and x=3, respectively. The inset **a**, **b**, and **c** schematic are corresponded with red, blue, and green background regime. Yellow sphere and blue sphere (both light and dark blue) indicate Li ion and P atom, respectively.*

The electrochemical device serves as an excellent platform to investigate the dynamics of Li intercalation into BPh film and the resulting structural evolution. The electrochemical measurements and ionic intercalation control are performed using a BioLogic VSP-300 chemical station. The galvanostatic discharge was done with a constant current smaller than 3.0 μA and control the battery potential from 2.1 V to 0.01 V. The ionic intercalation discharge process was done by decreasing the voltage of a fully charged BP battery with a step size smaller than 0.05 V. For each step, before the thermal measurement, the battery device was hold at the constant voltage for more than 3 hour until battery current reduces to a small level (< 10 pA) , to ensure that Li intercalation is complete and Li_xP reaches a stable status,. The reversibility cycling of a BP battery was done in the reversible voltage range between 2.0 V and 0.78 V using constant currents of 1 μA for charging and discharging, respectively.

A pristine BPh film typically shows an open circuit voltage between 1.9 V and 2.2 V with respect to Li/Li^+. We carried out Li interaction by gradually reducing the BPh potential with respect to Li/Li^+. A typical galvanostatic discharge curve of the discharge potential vs. lithium concentration (represented by x in Li_xP) is shown in Fig. 6.5. Evolution in the Li_xP structure (insert in Fig. 6.5) during discharge consists of three major regimes: (a) The first regime, highlighted in red, corresponds to physical intercalation of lithium ions. Initially, a steep drop in potential is observed due to change in the battery internal resistance[161]. The first plateau appears near 1.0 V, where a mixture of metastable Li_xP phases forms. Recent literature [162–164] reported that, despite the appearance of these phases, the lattice still maintains a 2D like structure with minimum volume change (represented as the structure **a** in the insert of Fig. 6.5). Discharge continues until the lithium slots are completely filled. Li ions enter the BP structure through the channels running in the zig-zag direction and settles in between P atoms [165]. Li intercalation is more preferentially aligned with ZZ direction due to the large difference in diffusion energy barriers in these two directions [166] (i.e., 0.68 eV and 0.08 eV for AC and ZZ respectively). In this regime, lithium ions involve physical intercalation into the interlayer spacing without forming chemical bonding with the BP lattice. (b) As more Li is driven into Li_xP the large attraction force between Li and P pulls on the P-P bounds until the bounds break, causing the alloy formation of LiP [167] (structure **b**). The second regime, highlighted in blue, marks the first break down of the P-P bounds. Once the battery is discharged beyond this point, the P-P bounds cannot be recovered. The discharge curve reaches the second plateau when the new LiP alloy phase is established. At the end of this stage, the available slots for accommodating Li in structure **b** are all occupied. (c) Further introducing Li ions after saturation will induce another pull on the yet unbroken P-P bounds. This change (from structure **b** to structure **c**) is accompanied by another drop in voltage,

and the discharge curve enters the third regime. In the third regime, highlighted in green, LiP undergoes another alloy formation process. Alternating layers of LiP and Li_2 appear until the ultimate formation of Li_3P [168] (structure **c** in the insert). Significant expansion in both lateral and longitudinal direction has been reported after complete discharge [169]. Therefore, for the *in-situ* thermal measurement, we first focus on charging/discharging the battery in the first regime to maintain a reversible BP structure and device performance.

6.5 *In-situ* Thermal conductivity measurement

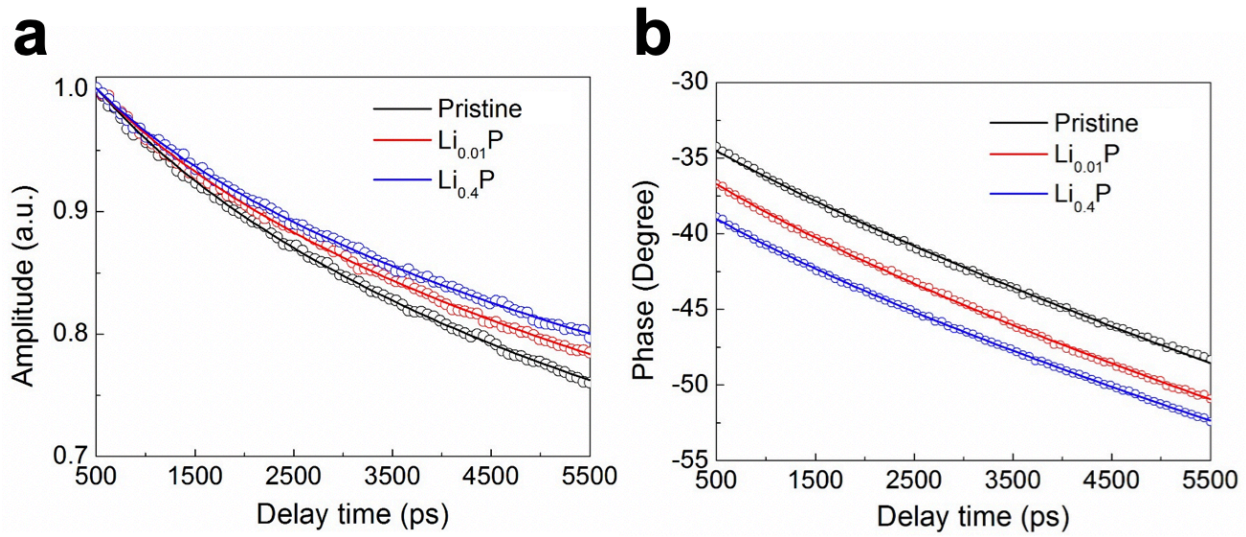

***Figure 6.7**. Experimental data for cross-plane thermal conductivity measurement based on the amplitude (a) and phase signals (b) (circles), and fits (solid line) from thermal model at different voltages.*

The cross-plane thermal conductivity of BP was measured *in-situ* during lithium interaction using TDTR. Typical experimental data of the transient TDTR amplitude and phase signal are shown in Fig 6.4a and 6.4b respectively. In addition, examples of measurement data at

different lithium concentrations (x = 0, 0.01, and 0.4 in Li_xP) are plotted together to illustrate the contrast in transport behaviors. Consistent results of κ_c are obtained by fitting amplitude and phase data using thermal diffusion modeling, and are shown in Fig. 6.4c. The κ_c of BP reduces gradually with increasing ionic intercalation. For example, κ_c is measured to be 3.24 ± 0.10 $W \cdot m^{-1} \cdot K^{-1}$ for $Li_{0.01}P$ and 2.45 ± 0.19 $W \cdot m^{-1} \cdot K^{-1}$ for $Li_{0.4}P$. The total drop of κ_c from pristine BP to $Li_{0.4}P$ is 37%.

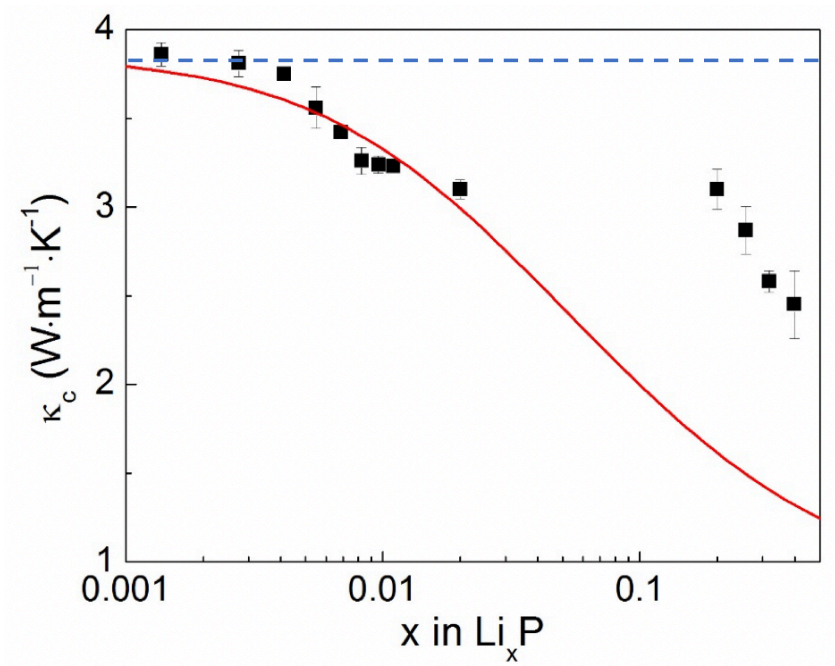

Figure 6.8. *The cross-plane thermal conductivity of black phosphorus is measured as a function of lithium concentrations during the battery discharge. Experimental data (solid rectangulars) is plot with the fit based on Callaway model (red line). The thermal conductivity of the pristine sample is marked in blue dashed line.*

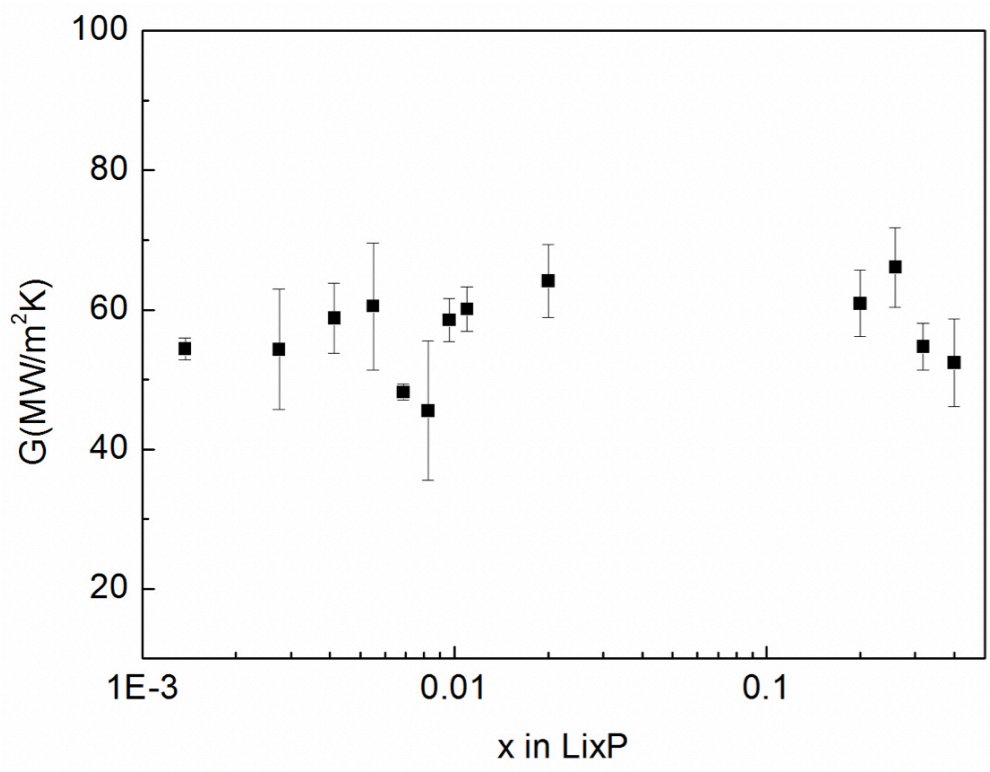

Figure 6.9. *The interface thermal conductance between aluminum and black phosphorus is measured as a function of lithium concentrations during the battery discharge*

Interface thermal conductance between optical transducer, aluminum, and BPh is also measured as a function of lithium concentration as shown in Fig. 6.9. In different with thermal conductivity, interface thermal conductance is not a function of lithium concentration.

The in-plane thermal conductivity of BPh was measured *in-situ* during lithium interaction using BO-TDTR. Typical experimental data of the out-phase signal V_{out} at different charge states (x = 0, x = 0.01, and x = 0.4 in Li_xP) along the ZZ direction are shown in Fig. 6.4d. The thermal conductivity in the ZZ direction are κ_{ZZ} = 85.80, 79.33, and 62.67 $W \cdot m^{-1} \cdot K^{-1}$, respectively for the three charge states after fitting with the obtained experimental data.

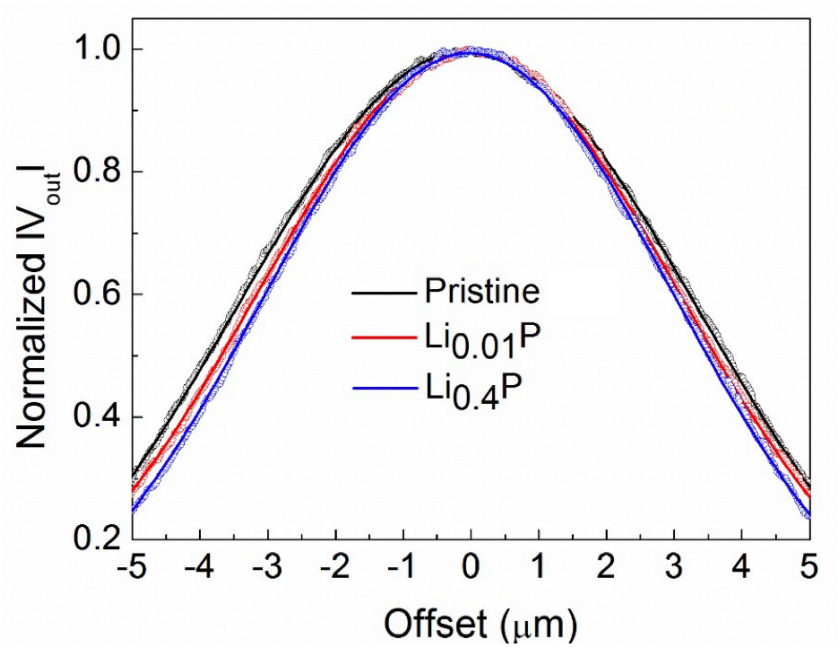

Figure 6.10. *Experimental data (V_{out}) (circles) for in-plane thermal conductivity measurement and fits from thermal model at three different lithium concentrations.*

Figures 6.4e and 6.4f show the charge state dependence of κ_{ZZ} and κ_{AC}, respectively. The in-plane κ reduces as more Li enters the interlayer spacing in BPh. κ_{ZZ} at x=0.4 is about 28% less than that of the pristine BPh. A similar trend in the ionic modulation of the thermal conductivity along the AC direction has been observed in experiment (Fig. 6.4f). For example, κ_{AC} are found to be 27.58, 25.23, and 21.66 $W \cdot m^{-1} \cdot K^{-1}$ at x=0, 0.01, and 0.4, respectively. The total thermal conductivity drop in the AC direction is 21%.

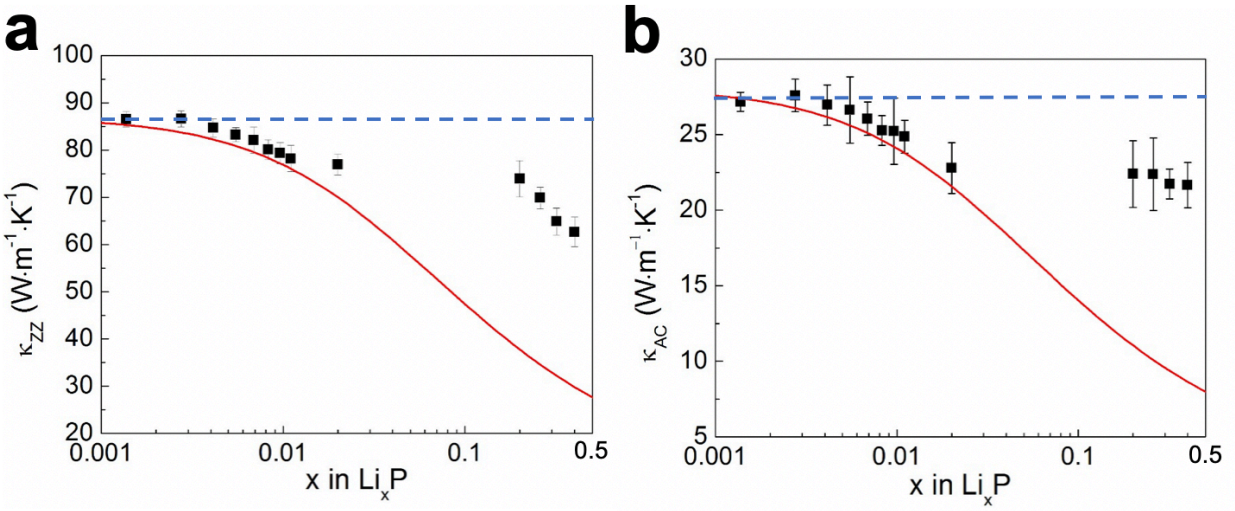

Figure 6.11. *The in-plane thermal conductivity (zigzag (e)and armchair (f) direction respectively) of black phosphorus is measured as a function of lithium concentrations during the battery discharge. Experimental data (solid rectangulars) is plot with the fit based on Callaway model (red line). The thermal conductivity of the pristine sample is marked in blue dashed line.*

It is interesting to note that such a reduction of the in-plane thermal conductivity of BPh, although impressive, is relatively small in comparison to previous studies on other 2D materials [170,171]. For example, a significant thermal conductivity reduction (from ~ 2500 to ~ 370 W·m^{-1}·K^{-1}) from suspended to substrate-supported graphene has been observed at room temperature[171], due to interactions between the substrate and graphene. On the other hand, the lithium ions here intercalated in the interlayer spacing and sandwiched between 2D layers, intuitively are expected to produce stronger scattering than that from the interaction with the substrate. However, a much less reduction in thermal conductivity is measured in the BPh samples. We attribute such difference to the following mechanisms: Firstly, BPh has a relatively larger interlayer space (~5 Å) to accommodate the intercalation of lithium ions (1.52 Å) and minimize structure distortion[165]. Secondly, the relative contribution to thermal conductivity from varied phonon vibration modes is different in BPh versus graphene. Generally, the heat in 2D materials can be carried by three different phonon modes: out-of-phase acoustic (ZA), longitudinal acoustic (LA),

and transverse acoustic (TA), among which ZA is most affected by ambient scattering such as scattering from the substrate or due to the ion intercalation. ZA mode contribution to the in-plane thermal conductivity of graphene is large and reported to be more higher than 75% [170,172]. In contrary, recent first principle calculations have predicted that ZA phonon in BPh only carries 12~31% of the in-plane thermal conductivity [173]. Our experimental results confirm that BPh is less susceptible than graphene under ambient scattering.

To elucidate the physical mechanism behind the thermal conductivity reduction due to ionic intercalation, the semi-classical Callaway model [174] is used to analyze our experimental results. The thermal conductivity derived by Callaway model is expressed by

$$\kappa = \frac{k_B}{2\pi^2 v}\left(\frac{k_B}{\hbar}\right)^3 T^3 \int_0^{\frac{\theta_D}{T}} \frac{\chi^4 e^{\chi}}{e^{\chi}-1}\tau\, d\chi \qquad (6\text{-}1)$$

where v, T, k_B, θ_D and ħ are the phonon group velocity, the sample temperature, the Boltzmann constant, Debye temperature, and the Plank constant, respectively. The dimensionless parameter χ is define as $\hbar\omega / k_B T$ and ω is the phonon frequency. The total phonon relaxation time (τ) is expressed by equation (3-2) and for the single crystal BPh sample, boundary scattering is considered negligible.

Therefore, equation (6-1) can be expressed as [138]

$$\kappa = \frac{k_B^2 T^3 \hbar}{2\pi^2 v}\int_0^{\frac{\theta_D}{T}} \frac{\chi^2 e^{\chi}}{T^2(Ak_B^2T^2\chi^2 + B)(e^{\chi}-1)^2}\, d\chi \qquad (6\text{-}2)$$

At high temperature limit (χ < 1), $\frac{\chi^4 e^{\chi}}{e^{\chi}-1} \approx 1$, then [138]

$$\kappa = \frac{k_B}{2v\pi^2 (AB)^{1/2}} \tan^{-1}\left(\frac{k_B\theta_D}{\hbar}\left(\frac{A}{B}\right)^{1/2}\right) \qquad (6\text{-}3)$$

For the pristine BPh (i.e., A→0)), the thermal conductivity is related to the coefficient B by

$$\kappa_0 = \frac{k_B^2 \theta_D}{2\pi^2 v \hbar B} \qquad (6\text{-}4)$$

Thus, the value of B (the coefficient of anharmonic scattering term) can be directly calculated from the experimentally measured κ_0 value. The Rayleigh coefficient A can be further expressed in two items to describe mass disorder and lattice disorder [175], is

$$A = \frac{\Omega_0}{4\pi v^3}(\Gamma_m + \Gamma_l) = \frac{\Omega_0}{4\pi v^3} c(1-c)\left(\left(\frac{\Delta M}{M_{avg}}\right)^2 + \varepsilon\left(\frac{\Delta r}{r_{avg}}\right)^2\right) \qquad (6\text{-}5)$$

where the Ω_0 is the unit cell volume, Γ_m and Γ_l are scaling parameters to descript mass disorder and lattice disorder, respectively. c is the relative impurity concentration of Li_xP, and can be calculated as $c = \frac{x}{1+x}$. ΔM is the mass different between BPh atom and Li ion, M_{avg} is the average mass of compound, Δr is the atomic radius different between BPh and Li, r_{ave} is the average atomic radius. The mass disorder term is directly calculated with respect to function of Li ions. To describe lattice disorder, phenomenological adjustable parameter, ε, is introduced to be determined by experimental fitting, which is a function of Grüneisen parameter by strain fluctuation [176]. Therefore, after A and B are replaced with Eq. (6-4) and (6-5) respectively, ε is the only fitting parameter for thermal conductivity in Eq. (6-5). We fit our experimental results using the derived Callaway model.

The fitting results from semi-classical Callaway model is shown in Fig. 6.4c, 6.4e and 6.4f. In the low concentration regime (x < 0.1), the model agrees well with our experimental results. The fitted value of ε along cross-plane and in-plane direction is different. For cross-plane

direction, ε is fitted to be ~ 40, which is consistent with literature expectation [175], and indicates that Li intercalation between BP layer introduces lattice distortion to the cross-plane direction. On the other hand, the ε value is ~ 1 for both in-plane directions which indicates that in-plane lattice distortion is not as important, while the large mass difference between Li ion and P atom (~ 5 times) provides the major contribution to impurity scattering.

In the high Li concentration regime (x > 0.1), however, model fitting is deviated from experiment despite of any choice of ε values. Interestingly, such discrepancy is consistent with the metastable phases between BPh and LiP predicted by recent theoretical study [177]. In addition, because Callaway model is derived for isotropic material such as silicon, it may not be able to capture the anisotropic properties of BPh. We expect future improvement of theoretical model using first-principle methods [178] and including anisotropic characteristics [179] will provide better understanding of our experimental data.

6.6 Cycle dependent thermal conductivity and thermal transistor

To check the reversibility of the electrochemical control over thermal conductivity, we performed *in-situ* measurement over battery charging/discharging up to 100 cycles. Figure 6.5a shows a cycling measurement on κ_c for pristine BPh and $Li_{0.4}P$, corresponding to 2.0V and 0.78V respectively. We use 0.05C current rate for battery cycling to minimize crystalline distortion of BPh. During 100 cycling, κ_c variations at 2.0 V and 0.78V are within measurement uncertainty range, which are 3.86~4.25 $W \cdot m^{-1} \cdot K^{-1}$ (2.0 V) and 2.36~2.52 $W \cdot m^{-1} \cdot K^{-1}$ (0.78 V). The results show that the electrochemical tuning of thermal conductivity is highly reversible: the modulation of κ_C maintains ~ 40% between the two state (i.e., x=0 and 0.4 in Li_xP) up to 100 cycles. This dynamic and reversible tunability of κ in layered material in fact demonstrates a novel ionic gate

thermal transistor [180] that controls thermal conductivity with ON/OFF switching capability.

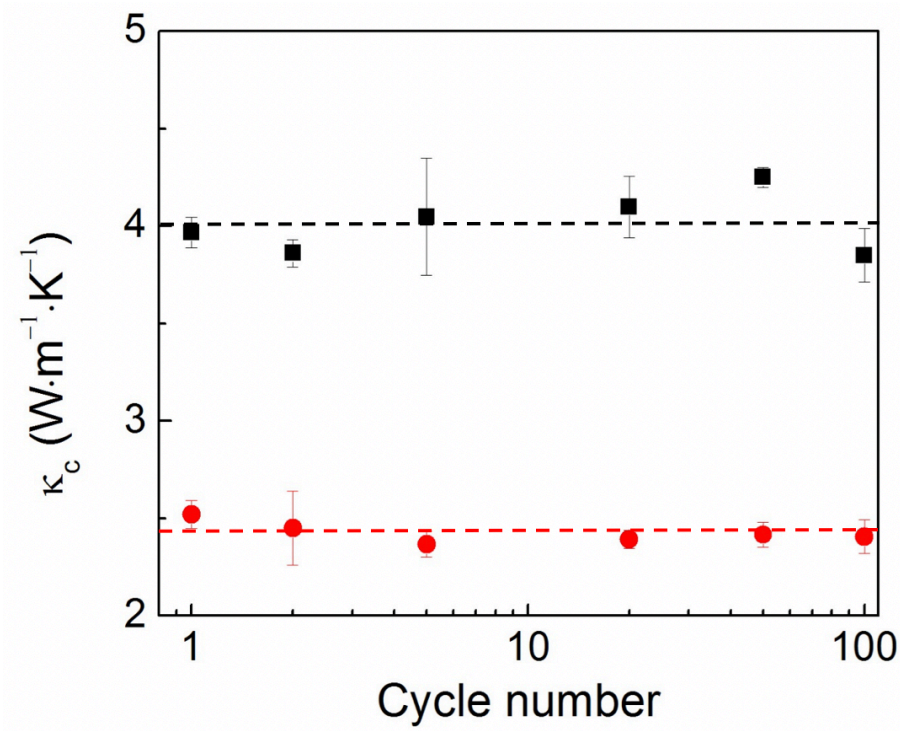

Figure 6.12. *Reversibility measurement of the thermal regulation, and summary of thermal conductivities of black phosphorus. Thermal conductivity is measured as a function of battery charge/discharge cycles. For each cycle, the cross-plane thermal conductivity is measured for fully charged state (rectangulars, V= 2.0 V) and at V= 0.78 V (circles). The average values of the maximum and minimum thermal conductivity over 100 charge cycles, are marked in black and red dash lines.*

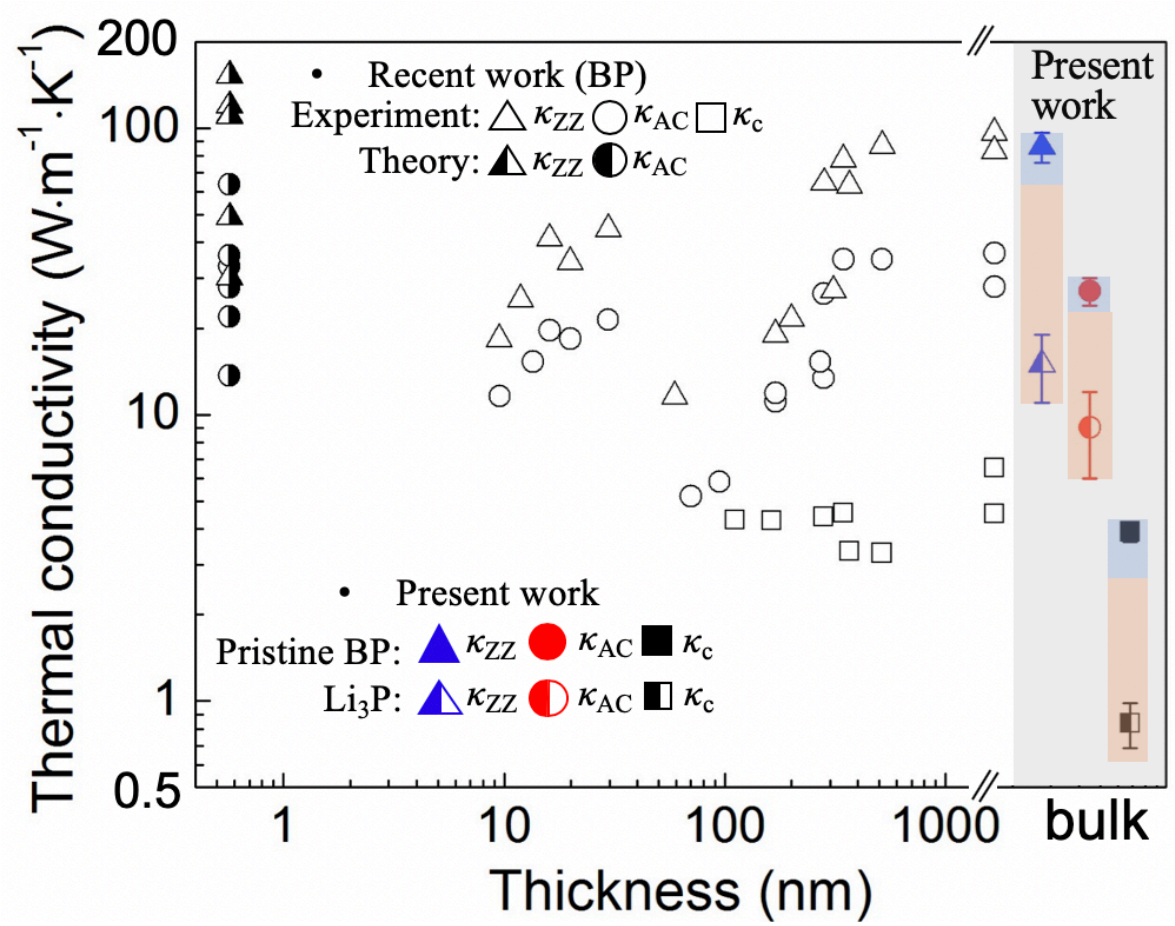

Figure 6.13. *Summary of thermal conductivity measurement in three different directions, plotted in comparison to reported values as a function of thickness. Results from this work are highlighted on the right side in the figure. Thermal conductivities of black phosphorus for the zigzag (blue), the armchair (red), and cross-plane (black) are plotted to illustrate the thermal regulation range from the fully charged state (filled symbols) to fully discharged state (half-filled symbols). Reversible and irreversible regime for thermal regulation is marked in blue and red background, respectively.*

Our study has demonstrated a novel electrochemical approach to reversibly control thermal conductivity through *in-situ* ionic intercalation. In addition to measurement in the first reversible regime of BPh, we also measured the κ of the fully discharged sample (Li_3P). In this irreversible regime, the measured κ_c, κ_{AC}, and κ_{ZZ}, are 0.84 ± 0.25 $W \cdot m^{-1} \cdot K^{-1}$, 9.25 ± 3.18 $W \cdot m^{-1} \cdot K^{-1}$ and 15.57 ± 4.98 $W \cdot m^{-1} \cdot K^{-1}$, respectively. The measured thermal conductivity of Li_3P are

remarkably lower than pristine BPh. Impressively, it gives the factors of 5, 3, and 6 times the tunability of κ_c, κ_{AC}, and κ_{ZZ}, respectively. The origin of the low thermal conductivity comes from the crystallinity of BPh that is damaged by Li intercalation and single crystal BPh is transformed into polycrystalline Li_3P. Consistently, the recently reported *in-situ* XRD measurement reveals that the BPh single crystal has been irreversibly transformed to a polycrystalline Li_3P in the fully discharge state [181]. Figure 6.5b summarizes the thermal conductivity values of BPh from our study and the literature [7,8,188,9,173,182–187]. The reversible and irreversible thermal conductivity tuning regime is shown in the Fig 6.5b. It covers remarkably a large thermal conductivity tuning range and shows that Li ion intercalation can be a powerful method for thermal conductivity tuning.

6.7 Summary

In summary, we reported, for the first time, an active and reversible tuning of thermal conductivity of 2D materials using Li ion intercalation. A unique *in-situ* measurement platform for modulating thermal property during electrochemical intercalation was developed. The pristine and voltage-dependent κ variations in BP are found to be highly anisotropic, with values in the reversible regime ($0 < x < 0.4$ in Li_xP) varying from 2.45~3.86 $W \cdot m^{-1} \cdot K^{-1}$, 62.67 ~ 85.80 $W \cdot m^{-1} \cdot K^{-1}$, and 21.66 ~ 27.58 $W \cdot m^{-1} \cdot K^{-1}$ in the cross-plane, ZZ, and AC directions, respectively. The difference in reduction is as high as 37%. Moreover, at the fully discharged state ($x \sim 3$ in Li_xP), the measured κ_c, κ_{ZZ}, and κ_{AC} are 0.84 $W \cdot m^{-1} \cdot K^{-1}$, 9.25 $W \cdot m^{-1} \cdot K^{-1}$, and 15.57 $W \cdot m^{-1} \cdot K^{-1}$ respectively, demonstrating an ultrahigh tunability of κ at factors of ~ 5, 3, and 6 times. These results reveal an effective mechanism for modifying the thermal conductivity of 2D materials based on electrochemical intercalation and phase transitions, and a novel approach to control

anisotropic energy transport by designing nanostructures. In addition, it may open up a new direction for spectral engineering thermal properties through mapping, scattering and manipulating the phonon spectra in a rational way.

CHAPTER 7

Conclusion

Maximizing or minimizing heat flow is one of the biggest bottlenecks in many engineering applications such as high-power electronics and high efficiency energy converter. Extreme thermal conductivity materials can be building block in many advanced technologies to solve it. In this dissertation, I synthesized new thermal materials and investigates their extreme thermal properties by developing new experimental methodology. My experimental measurement combined with atomistic simulation provided new physical understanding of extreme thermal transport in single crystal materials.

For ultrahigh thermal conductivity, I synthesize high quality single crystal BP and BAs are chemically synthesized and measured a record-high room temperature thermal conductivity ~ 460 and 1300 W/m·K, respectively. Thermal conductivity of BP is three times higher than that of Si and exceeding the best conducting metals such as copper and silver. Also, thermal conductivity of BAs is two times higher than c-BN and 60% of diamond which are second best and the best thermal conductor. I performed temperature-dependent thermal conductivity measurement using TDTR technique and analyzed phonon scattering mechanisms through modeling and multi-scale simulations. I further explored the phonon spectra through probing quasi-ballistic thermal transport and size-dependent measurement. Based on phonon Boltzmann transport equation and variance-reduced Monte Carlo simulation, the ballistic transport is

explained based on phonon mode dependent scattering. Furthermore, in combination of experiment and modeling, I directly reconstructed the phonon mean free path spectra for boron compound, which shows good consistency with the recent Density Functional Theory prediction. Our experimental measurements and modeling analysis on thermal transport of boron compound provides a detailed microscopic understanding of the phonon spectra and thermal transport mechanisms.

Additionally, I report basic physical properties of cubic BAs, including the optical, mechanical, and thermomechanical properties. With its ultrahigh thermal conductivity, I believe that the systematically reported physical properties of BAs will further facilitate the development of this new semiconductor for thermal, electrical, optical, and mechanical applications.

For ultralow thermal conductivity, I investigated the nanoscale anisotropic thermal transport on SnSe single-crystals and measured their intrinsic thermal conductivity. The room temperature thermal conductivities are 1.48, 0.91 and 0.49 W/m·K along the b, c and a-axis, respectively. My temperature dependent data from 120 to 300 K verifies that the anharmonic phonon scattering dominates transport in high purity single crystals. My result solves the literature controversy, which is clearly related to SnSe sample quality, and verifies the anharmonic contribution to the extremely low thermal conductivity of SnSe. Furthermore, I successfully measured the temperature dependent Grüneisen parameter at the Brillouin zone centre using Picosecond Laser Ultrasonics and XRD. Ab initio calculations is performed using harmonic, quasi-harmonic, and anharmonic models. The measurement and modelling study show a very strong temperature-dependent intrinsic anharmonicity and indicates that the harmonic and quasi-harmonic models that are widely used in the current first-principles theory may not be applicable to SnSe. My study represents a significant research benchmark for high-performance thermal and energy

materials and establishes a fundamental insight to improving the first-principles calculations and modern phonon transport theory.

Last, I investigated a dynamic tuning of thermal conductivity in layered materials using ion intercalation. A unique *in-situ* measurement platform for modulating thermal property during electrochemical intercalation was developed. Thermal conductivity of the pristine and ion intercalated BPh are studied by using TDTR method. I found that thermal conductivity is highly anisotropic, with values in the reversible regime ($0 < x < 0.4$ in Li_xP) varying from 2.45~3.86 $W \cdot m^{-1} \cdot K^{-1}$, 62.67 ~ 85.80 $W \cdot m^{-1} \cdot K^{-1}$, and 21.66 ~ 27.58 $W \cdot m^{-1} \cdot K^{-1}$ in the cross-plane, ZZ, and AC directions, respectively. The difference in reduction is as high as 37%. Moreover, at the fully discharged state ($x \sim 3$ in Li_xP), the measured κ_c, κ_{ZZ}, and κ_{AC} are 0.84 $W \cdot m^{-1} \cdot K^{-1}$, 9.25 $W \cdot m^{-1} \cdot K^{-1}$, and 15.57 $W \cdot m^{-1} \cdot K^{-1}$ respectively, demonstrating an ultrahigh tunability of κ at factors of ~ 5, 3, and 6 times. These results provide a promising way for modifying the thermal conductivity in layered materials based on electrochemical intercalation and phase transitions.

Reference

1. Schmidt, A. J., Chen, X. & Chen, G. Pulse accumulation, radial heat conduction, and anisotropic thermal conductivity in pump-probe transient thermoreflectance. *Rev. Sci. Instrum.* **79**, 114902 (2008).
2. Cahill, D. G. Analysis of heat flow in layered structures for time-domain thermoreflectance. *Rev. Sci. Instrum.* **75**, 5119–5122 (2004).
3. Liu, J., Choi, G. M. & Cahill, D. G. Measurement of the anisotropic thermal conductivity of molybdenum disulfide by the time-resolved magneto-optic Kerr effect. *J. Appl. Phys.* **116**, 233107 (2014).
4. Jiang, P., Qian, X. & Yang, R. Tutorial: Time-domain thermoreflectance (TDTR) for thermal property characterization of bulk and thin film materials. *J. Appl. Phys.* **124**, 161103 (2018).
5. Feser, J. P. & Cahill, D. G. Probing anisotropic heat transport using time-domain thermoreflectance with offset laser spots. *Rev. Sci. Instrum.* **83**, 104901 (2012).
6. Feser, J. P., Liu, J. & Cahill, D. G. Pump-probe measurements of the thermal conductivity tensor for materials lacking in-plane symmetry. *Rev. Sci. Instrum.* **85**, 104903 (2014).
7. Jang, H., Wood, J. D., Ryder, C. R., Hersam, M. C. & Cahill, D. G. Anisotropic Thermal Conductivity of Exfoliated Black Phosphorus. *Adv. Mater.* **27**, 8017–8022 (2015).
8. Zhu, J. *et al.* Revealing the Origins of 3D Anisotropic Thermal Conductivities of Black Phosphorus. *Adv. Electron. Mater.* **2**, 1600040 (2016).
9. Sun, B., Zeng, Q., Huang, X., Liu, Z. & Kan Koh, Y. Temperature dependence of anisotropic thermal conductivity tensor of bulk black phosphorus. *Adv. Mater.* **29**, 1603297 (2016).
10. Lee, T. *et al.* Elastic constants of single-crystal TiNx(001) ($0.67<x<1.0$) determined as a function of x by picosecond ultrasonic measurements. *Phys. Rev. B* **71**, 144106 (2005).
11. Waldrop, M. M. The chips are down for Moore's law. *Nature* **530**, 144 (2016).
12. Ball, P. Feeling the heat. *Nature* **492**, 175–176 (2012).
13. Shehabi, A. *et al. United States data center energy usage report*. (2016).

14. ITRS. International Technology Roadmap for Semiconductors 2.0: Executive Report. *Int. Technol. roadmap Semicond.* (2015).
15. Ziman, J. M. *Electrons and Phonons: The Theory of Transport Phenomena in Solids.* (1960).
16. Slack, G. A. Nonmetallic crystal with high thermal conductivity. *J. Phys. Phys. Chem. Solids* **34**, 321–335 (1973).
17. Lindsay, L., Broido, D. A. & Reinecke, T. L. First-Principles Determination of Ultrahigh Thermal Conductivity of Boron Arsenide: A Competitor for Diamond? *Phys. Rev. Lett.* **111**, 25901 (2013).
18. Mingo, N. & Broido, D. A. Lattice thermal conductivity crossovers in semiconductor nanowires. *Phys. Rev. Lett.* **93**, 1–4 (2004).
19. Mingo, N. & Broido, D. A. Carbon nanotube ballistic thermal conductance and its limits. *Phys. Rev. Lett.* **95**, 26–29 (2005).
20. Ward, A., Broido, D. A., Stewart, D. A. & Deinzer, G. Ab initio theory of the lattice thermal conductivity in diamond. *Phys. Rev. B* **80**, 125203 (2009).
21. Esfarjani, K., Chen, G. & Stokes, H. T. Heat transport in silicon from first-principles calculations. *Phys. Rev. B* **84**, 085204 (2011).
22. Lindsay, L., Broido, D. A. & Reinecke, T. L. Thermal conductivity and large isotope effect in GaN from first principles. *Phys. Rev. Lett.* **109**, 095901 (2012).
23. Luckyanova, M. N. *et al.* Coherent phonon heat conduction in superlattices. *Science (80-.).* **2360**, 936–939 (2012).
24. Hu, Y., Zeng, L., Minnich, A. J., Dresselhaus, M. S. & Chen, G. Spectral mapping of thermal conductivity through nanoscale ballistic transport. *Nat. Nanotechnol.* **10**, 701–706 (2015).
25. Feng, T., Lindsay, L. & Ruan, X. Four-phonon scattering significantly reduces intrinsic thermal conductivity of solids. *Phys. Rev. B* **96**, 1–6 (2017).
26. Chu, T., Jackson, J. & Smeltzer, R. The Crystal Growth of Boron Monophosphide from Metal Phosphide Solutions. *J. Electrochem. Soc.* **120**, 802–806 (1973).
27. Adachi, S. *Properties of semiconductor alloys: group-IV, III-V and II-VI semiconductors*. **28**, (John Wiley & Sons, 2009).
28. Goossens, A. & Schoonman, J. An impedance study of boron phosphide semiconductor

electrodes. *J. Electrochem. Soc* **139**, 893–900 (1992).

29. Sanjurjo, J. A., Lpez-Cruz, E., Vogl, P. & Cardona, M. Dependence on volume of the phonon frequencies and their effective charges of several III-V semiconductors. *Phys. Rev. B* **28**, 4579–4584 (1983).
30. Callaway, J. Model for Lattice Thermal Conductivity at Low Temperatures. *Phys. Rev.* **113**, 1046–1051 (1959).
31. Klemens, P. G. The Scattering of Low-Frequency Lattice Waves by Static Imperfections. *Proc. Phys. Soc. Sect. A* **68**, 1113–1128 (1955).
32. Slack, G. A. & Galginaitis, S. Thermal conductivity and phonon scattering by magnetic impurities in CdTe. *Phys. Rev.* **133**, A253 (1964).
33. Morelli, D. T., Heremans, J. P. & Slack, G. A. Estimation of the isotope effect on the lattice thermal conductivity of group IV and group III-V semiconductors. *Phys. Rev. B* **66**, 195304 (2002).
34. Yang, F. & Dames, C. Mean free path spectra as a tool to understand thermal conductivity in bulk and nanostructures. *Phys. Rev. B* **87**, 035437 (2013).
35. Broido, D. A., Lindsay, L. & Reinecke, T. L. Ab initio study of the unusual thermal transport properties of boron arsenide and related materials. *Phys. Rev. B* **88**, 214303 (2013).
36. Hu, Y. J., Zeng, L. P., Minnich, A. J., Dresselhaus, M. S. & Chen, G. Spectral mapping of thermal conductivity through nanoscale ballistic transport. *Nat. Nanotechnol.* **10**, 701–706 (2015).
37. Chen, G. Nonlocal and Nonequilibrium Heat Conduction in the Vicinity of Nanoparticles. *J. Heat Transfer* **118**, 539–545 (1996).
38. Mazumder, S. & Majumdar, A. Monte Carlo Study of Phonon Transport in Solid Thin Films Including Dispersion and Polarization. *J. Heat Transfer* **123**, 749–759 (2001).
39. Péraud, J.-P. M. & Hadjiconstantinou, N. G. Efficient simulation of multidimensional phonon transport using energy-based variance-reduced Monte Carlo formulations. *Phys. Rev. B* **84**, 205331 (2011).
40. Péraud, J.-P. M. & Hadjiconstantinou, N. G. An alternative approach to efficient simulation of micro/nanoscale phonon transport. *Appl. Phys. Lett.* **101**, 153114 (2012).
41. Forghani, M., Hadjiconstantinou, N. G. & Péraud, J.-P. M. Reconstruction of the phonon

relaxation times using solutions of the Boltzmann transport equation. *Phys. Rev. B* **94**, 155439 (2016).

42. Baker, L. L. & Hadjiconstantinou, N. G. Variance reduction for Monte Carlo solutions of the Boltzmann equation. *Phys. Fluids* **17**, 051703 (2005).
43. Wilson, R. B. & Cahill, D. G. Anisotropic failure of Fourier theory in time-domain thermoreflectance experiments. *Nat. Commun.* **5**, 5075 (2014).
44. Ding, D., Chen, X. & Minnich, A. J. Radial quasiballistic transport in time-domain thermoreflectance studied using Monte Carlo simulations. *Appl. Phys. Lett.* **104**, 143104 (2014).
45. Vermeersch, B., Mohammed, A. M. S., Pernot, G., Koh, Y. R. & Shakouri, A. Superdiffusive heat conduction in semiconductor alloys. II. Truncated L\'evy formalism for experimental analysis. *Phys. Rev. B* **91**, 85203 (2015).
46. Dames, C. & Chen, G. *Thermal conductivity of nanostructured thermoelectric materials*. (CRC Press, Boca Raton, FL, 2006).
47. Wei, L., Kuo, P. K., Thomas, R. L., Anthony, T. R. & Banholzer, W. F. Thermal conductivity of isotopically modified single crystal diamond. *Phys. Rev. Lett.* **70**, 3764–3767 (1993).
48. Onn, D. G., Witek, A., Qiu, Y. Z., Anthony, T. R. & Banholzer, W. F. Some aspects of the thermal conductivity of isotopically enriched diamond single crystals. *Phys. Rev. Lett.* **68**, 2806–2809 (1992).
49. Olson, J. R. *et al.* Thermal conductivity of diamond between 170 and 1200 K and the isotope effect. *Phys. Rev. B* **47**, 14850–14856 (1993).
50. Protik, N. H., Carrete, J., Katcho, N. A., Mingo, N. & Broido, D. Ab initio study of the effect of vacancies on the thermal conductivity of boron arsenide. *Phys. Rev. B* **94**, 045207 (2016).
51. Maradudin, A. & Fein, A. Scattering of Neutrons by an Anharmonic Crystal. *Phys. Rev.* **128**, 2589 (1962).
52. Lindsay, L. & Broido, D. A. Three-phonon phase space and lattice thermal conductivity in semiconductors. *J. Phys. Condens. Matter* **20**, 165209 (2008).
53. Tamura, S.-I. Isotope scattering. *Phys. Rev. B* **27**, 858–866 (1983).
54. Li, W., Carrete, J., Katcho, N. A. & Mingo, N. ShengBTE: A solver of the Boltzmann

transport equation for phonons. *Comput. Phys. Commun.* **185**, 1747–1758 (2014).

55. Hohenberg, P. & Kohn, W. Inhomogeneous Electron Gas. *Phys. Rev.* **136**, B864–B871 (1964).
56. Kohn, W. & Sham, L. . Self-Consistent Equations Including Exchange and Correlation Effects. *Phys. Rev.* **140**, A1133–A1138 (1965).
57. Baroni, S., Gironcoli, S. de & Corso, A. D. Phonons and related crystal properties from density-functional perturbation theory. *Rev. Mod. Phys.* **73**, 515–562 (2001).
58. Giannozzi, P. *et al.* QUANTUM ESPRESSO: A modular and open-source software project for quantum simulations of materials. *J. Phys. Condens. Matter* **21**, 395502 (2009).
59. Giannozzi, P. *et al.* Advanced capabilities for materials modelling with Quantum ESPRESSO. *J. Phys. Condens. Matter* **29**, 465901 (2017).
60. *We used the pseudopotentials B.pz-n-kjpaw_psl.0.1.UPF and As.pz-n-kjpaw_psl.0.2.UPF from the Quantum ESPRESSO pseudopotential data base*.
61. Li, W., Lindsay, L., Broido, D. A., Stewart, D. A. & Mingo, N. Thermal conductivity of bulk and nanowire Mg2Si xSn1-x alloys from first principles. *Phys. Rev. B* **86**, 174307 (2012).
62. Li, W. *et al.* Thermal conductivity of diamond nanowires from first principles. *Phys. Rev. B* **85**, 195436 (2012).
63. Kang, J. S., Wu, H. & Hu, Y. Thermal Properties and Phonon Spectral Characterization of Synthetic Boron Phosphide for High Thermal Conductivity Applications. *Nano Lett.* **17**, 7507–7514 (2017).
64. Lindsay, L., Broido, D. A. & Reinecke, T. L. Phonon-isotope scattering and thermal conductivity in materials with a large isotope effect: A first-principles study. *Phys. Rev. B* **88**, 144306 (2013).
65. Kang, J. S., Li, M., Wu, H., Nguyen, H. & Hu, Y. Experimental observation of high thermal conductivity in boron arsenide. *Science (80-.).* **361**, 575–578 (2018).
66. Stukel, D. J. Electronic structure and optical spectrum of boron arsenide. *Phys. Rev. B* **1**, 3458–3463 (1970).
67. Prasad, C. & Sahay, M. Electronic Structure and Properties of Boron Phosphide and Boron Arsenide. *Phys. Status Solidi* **154**, 201–207 (1989).
68. Bushick, K., Mengle, K., Sanders, N. & Kioupakis, E. Band structure and carrier effective

masses of boron arsenide: Effects of quasiparticle and spin-orbit coupling corrections. *Appl. Phys. Lett.* **114**, 022101 (2019).

69. Chu, T. L. & Hyslop, A. E. Preparation and properties of boron arsenide films. *J. Electrochem. Soc* **121**, 412–415 (1974).
70. Ku, S. M. Preparation and Properties of Boron Arsenides and Boron Arsenide-Gallium Arsenide Mixed Crystals. *J. Electrochem. Soc.* **113**, 813–816 (1966).
71. Ge, Y., Wan, W., Guo, X. & Liu, Y. The direct and indirect optical absorptions of cubic BAs and BSb. *arXiv* arXiv:1901.03947 (2019).
72. Wang, S. *et al.* Synthesis and characterization of a p-type boron arsenide photoelectrode. *J. Am. Chem. Soc.* **134**, 11056–11059 (2012).
73. Fox, M. *Optical properties of solids*. (Oxford university press, 2002).
74. Lalngaihawmi, R., Vanlalruata, B., Hnamte, L. & Thapa, R. K. Study of electronic and optical properties of boron arsenide. *Int. Conf. Electr. Electron. Optim. Tech. ICEEOT 2016* 1162–1166 (2016).
75. Guemou, M. *et al.* First-principles calculations of the structural, electronic and optical properties of cubic B xGa 1-xAs alloys. *Phys. B Condens. Matter* **407**, 1292–1300 (2012).
76. Manifacier, J. C., Gasiot, J. & Fillard, J. P. A simple method for the determination of the optical constants n, k and the thickness of a weakly absorbing thin film. *J. Phys. E.* **9**, 1002–1004 (1976).
77. Saleh, B. E. A. & Teich, M. C. *Fundamentals of photonics*. (John Wiley & Sons, 2019).
78. Bond, W. L. Measurement of the refractive indices of several crystals. *J. Appl. Phys.* **36**, 1674–1677 (1965).
79. Marple, D. T. F. Refractive index of GaAs. *J. Appl. Phys.* **35**, 1241–1242 (1964).
80. Auld, B. A. *Acoustic Fields and Waves in Solids*. **27**, (John Wiley & Sons, 1973).
81. Hopcroft, M. A., Nix, W. D. & Kenny, T. W. What is the Young's modulus of silicon? *J. Microelectromechanical Syst.* **19**, 229–238 (2010).
82. Bauchau, O. A. & Craig, J. I. *Structural analysis: with applications to aerospace structures*. (2009).
83. Thomsen, C., Grahn, H., Maris, H. & Tauc, J. Surface generation and detection of phonons by picosecond light pulses. *Phys. Rev. B* **34**, 4129–4138 (1986).
84. Li, M., Kang, J. S. & Hu, Y. Anisotropic thermal conductivity measurement using a new

Asymmetric-Beam Time-Domain Thermoreflectance (AB-TDTR) method. *Rev. Sci. Instrum.* **89**, (2018).

85. Kang, J. S., Ke, M. & Hu, Y. Ionic Intercalation in Two-Dimensional van der Waals Materials: In Situ Characterization and Electrochemical Control of the Anisotropic Thermal Conductivity of Black Phosphorus. *Nano Lett.* **17**, 1431–1438 (2017).
86. Kang, J. S., Wu, H., Li, M. & Hu, Y. Intrinsic Ultralow Thermal conductivity and Phonon Renormalization Due to Strong Anharmonicity of Single-Crystal Tin Selenide. *Nano Lett.* **19**, 4941–4948 (2019).
87. Kittel, C. *Introduction to solid state physics*. (Wiley New York, 1976).
88. Greene, R. G., Luo, H., Ruoff, A. L., Trail, S. S. & DiSalvo, F. J. Pressure induced metastable amorphization of BAs: Evidence for a kinetically frustrated phase transformation. *Phys. Rev. Lett.* **73**, 2476–2479 (1994).
89. Farnell, G. W. *Properties of elastic surface waves*. (1970).
90. Hu, Y., Kuemmeth, F., Lieber, C. M. & Marcus, C. M. Hole spin relaxation in Ge-Si core-shell nanowire qubits. *Nat. Nanotechnol.* **7**, 47–50 (2012).
91. Rogers, J., Maznev, A. & Nelson, K. Optical generation and characterization of acoustic waves in thin films: fundamentals and applications. *Annu. Rev. Mater. Sci.* **30**, 117 (2000).
92. Hess, P. Surface Acoustic Waves in Materials Science. *Phys. Today* **55**, 42 (2002).
93. Maznev, A. A. & Every, A. G. Surface acoustic waves in a periodically patterned layered structure. *J. Appl. Phys.* **106**, (2009).
94. Brantley, W. A. Calculated elastic constants for stress problems associated with semiconductor devices. *J. Appl. Phys.* **44**, 534–535 (1973).
95. Hill, R. The Elastic Behaviour of a Crystalline Aggregate. *Proc. Phys. Soc. Sect. A* **65**, 349–354 (1952).
96. Barron, T. H. K., Collins, J. G. & White, G. K. Thermal expansion of solids at nigh temperatures. *Adv. Phys.* **29**, 609–730 (1980).
97. Schelling, K. & Keblinski, P. Thermal expansion of carbon structures. *Phys. Rev. B - Condens. Matter Mater. Phys.* **68**, 1–7 (2003).
98. Mounet, N. & Marzari, N. First-principles determination of the structural, vibrational and thermodynamic properties of diamond, graphite, and derivatives. *Phys. Rev. B* **71**, 205214 (2005).

99. Tadano, T., Gohda, Y. & Tsuneyuki, S. Anharmonic force constants extracted from first-principles molecular dynamics: Applications to heat transfer simulations. *J. Phys. Condens. Matter* **26**, (2014).

100. Li, M., Kang, J. S. & Hu, Y. Anisotropic Thermal Boundary Resistance across 2D Black Phosphorus: Experiment and Atomistic Modeling of Interfacial Energy Transport. *Adv. Mater.* **31**, 1901021 (2019).

101. Reeber, R. R. & Wang, K. Lattice parameters and thermal expansion of GaN. *J. Mater. Res.* **15**, 40–44 (2000).

102. Blakemore, J. S. Semiconducting and other major properties of gallium arsenide. *J. Appl. Phys.* **53**, R123 (1982).

103. Sato, T., Ohashi, K., Sudoh, T., Haruna, K. & Maeta, H. Thermal expansion of a high purity synthetic diamond single crystal at low temperatures. *Phys. Rev. B* **65**, 092102 (2002).

104. Li, Z. & Bradt, R. C. Thermal expansion of the cubic (3C) polytype of SiC. *J. Mater. Sci.* **21**, 4366–4368 (1986).

105. Born, M. & Huang, K. *Dyanmical Thoery of Crystal Lattices*. (1954).

106. Koshchenko, V. I., Demidenko, A. F., Grinberg, Y. K., Yachmenex, V. E. & Radchenko, A. F. SPECIFIC-HEATS AND THERMODYNAMIC FUNCTIONS OF BP, BAS, AND B6AS AT 5-310K. *Inorg. Mater.* **17**, 1460 (1981).

107. Grüneisen, E. Theorie des festen Zustandes einatomiger Elemente. *Ann. Phys.* **39**, 257–306 (1912).

108. Novoselov, K. S. *et al.* Two-dimensional atomic crystals. *Proc. Natl. Acad. Sci.* **102**, 10451–10453 (2005).

109. Wang, Q. H., Kalantar-zadeh, K., Kis, A., Coleman, J. N. & Strano, M. S. Electronics and optoelectronics of two-dimensional transition metal dichalcogenides. *Nat. Nanotechnol.* **7**, 699–712 (2012).

110. Pospischil, A., Furchi, M. M. & Mueller, T. Solar-energy conversion and light emission in an atomic monolayer p-n diode. *Nat. Nanotechnol.* **9**, 257–261 (2014).

111. Lee, C. *et al.* Atomically thin p – n junctions with van der Waals heterointerfaces. *Nat. Nanotechnol.* **9**, 676–681 (2014).

112. Yu, W. J. *et al.* Vertically stacked multi-heterostructures of layered materials for logic

transistors and complementary inverters. *Nat. Mater.* **12**, 246–252 (2012).

113. Baugher, B. W. H., Churchill, H. O. H., Yang, Y. & Jarillo-herrero, P. Optoelectronic devices based on electrically tunable p – n diodes in a monolayer dichalcogenide. *Nat. Mater.* **9**, 262–267 (2014).
114. Xu, W. *et al.* Correlated fluorescence blinking in two-dimensional semiconductor heterostructures. *Nature* **541**, 62–67 (2017).
115. Rivera, P. *et al.* Valley-polarized exciton dynamics in a 2D semiconductor heterostructure. *Science (80-.).* **351**, (2016).
116. Wu, S. *et al.* Monolayer semiconductor nanocavity lasers with ultralow thresholds. *Nature* **520**, 69–72 (2015).
117. Chang, C. *et al.* 3D charge and 2D phonon transports leading to high out-of-plane ZT in n-type SnSe crystals. *Science* **360**, 778–783 (2018).
118. Zhao, L.-D. *et al.* Ultralow thermal conductivity and high thermoelectric figure of merit in SnSe crystals. *Nature* **508**, 373–7 (2014).
119. Zhao, L.-D. *et al.* Ultrahigh power factor and thermoelectric performance in hole-doped single-crystal SnSe. *Science (80-.).* **351**, 141–144 (2016).
120. Wei, P. C. *et al.* Thermoelectric Figure-of-Merit of Fully Dense Single-Crystalline SnSe. *ACS Omega* **4**, 5442–5450 (2019).
121. Jin, M. *et al.* Growth and characterization of large size undoped p-type SnSe single crystal by Horizontal Bridgman method. *J. Alloys Compd.* **712**, 857–862 (2017).
122. Ibrahim, D. *et al.* Reinvestigation of the thermal properties of single-crystalline SnSe. *Appl. Phys. Lett.* **110**, 032103 (2017).
123. Wang, S. *et al.* Low temperature thermoelectric properties of p -type doped single-crystalline SnSe. *Appl. Phys. Lett.* **112**, (2018).
124. Duong, A. T. *et al.* Achieving ZT=2.2 with Bi-doped n-type SnSe single crystals. *Nat. Commun.* **7**, 1–6 (2016).
125. González-Romero, R. L., Antonelli, A. & Meléndez, J. J. Insights into the thermoelectric properties of SnSe from: Ab initio calculations. *Phys. Chem. Chem. Phys.* **19**, 12804–12815 (2017).
126. Carrete, J., Mingo, N. & Curtarolo, S. Low thermal conductivity and triaxial phononic anisotropy of SnSe. *Appl. Phys. Lett.* **105**, 101907 (2014).

127. Wei, P. C. *et al.* The intrinsic thermal conductivity of SnSe. *Nature* **539**, E1–E2 (2016).
128. Sassi, S. *et al.* Assessment of the thermoelectric performance of polycrystalline p -type SnSe. *Appl. Phys. Lett.* **104**, 212105 (2014).
129. Chen, C.-L., Wang, H., Chen, Y.-Y., Day, T. & Snyder, J. Thermoelectric properties of p-type polycrystalline SnSe doped with Ag. *J. Mater. Chem. A* **2**, 11171–11176 (2014).
130. Chere, E. K. *et al.* Studies on thermoelectric figure of merit of Na-doped p-type polycrystalline SnSe. *J. Mater. Chem. A* **4**, 1848–1854 (2016).
131. Chen, Y. X. *et al.* Understanding of the Extremely Low Thermal Conductivity in High-Performance Polycrystalline SnSe through Potassium Doping. *Adv. Funct. Mater.* **26**, 6836–6845 (2016).
132. Popuri, S. R. *et al.* Large thermoelectric power factors and impact of texturing on the thermal conductivity in polycrystalline SnSe. *J. Mater. Chem. C* **4**, 1685–1691 (2016).
133. Guo, R., Wang, X., Kuang, Y. & Huang, B. First-principles study of anisotropic thermoelectric transport properties of IV-VI semiconductor compounds SnSe and SnS. *Phys. Rev. B - Condens. Matter Mater. Phys.* **92**, 1–13 (2015).
134. Li, C. W. *et al.* Orbitally driven giant phonon anharmonicity in SnSe. *Nat. Phys.* **11**, 1063 (2015).
135. Bansal, D. *et al.* Phonon anharmonicity and negative thermal expansion in SnSe. *Phys. Rev. B* **94**, 54307 (2016).
136. Liu, G., Zhou, J. & Wang, H. Anisotropic thermal expansion of SnSe from first-principles calculations based on Grüneisen's theory. *Phys. Chem. Chem. Phys.* **19**, 15187–15193 (2017).
137. Chandrasekhar, H. R., Humphreys, R. G., Zwick, U. & Cardona, M. Infrared and Raman spectra of the IV-VI compounds SnS and SnSe. *Phys. Rev. B* **15**, 2177–2183 (1977).
138. Callaway, J. & von Baeyer, H. Effect of Point Imperfections on Lattice Thermal Conductivity. *Phys. Rev.* **120**, 1149–1154 (1960).
139. Ziman, J. M. Principles of the Theory of Solids. *Cambridge Univ. Press* (1972).
140. Ashcroft, N. W. & Mermin, D. *Solid State Physics*. (Saunders College, 1976).
141. Postmus, C. & Ferraro, J. R. Pressure Dependence of Infrared Eigenfrequencies of KCl and KBr. *Phys. Rev.* **174**, 983 (1968).
142. Venkataraman, G. Soft modes and structural phase transitions. *Bullutin Mater. Sci.* **1**,

129–170 (1979).

143. Kim, D. S. *et al.* Phonon anharmonicity in silicon from 100 to 1500 K. *Phys. Rev. B* **91**, (2015).

144. Werthamer, N. R. Self-consistent phonon formulation of anharmonic lattice dynamics. *Phys. Rev. B* **1**, 572 (1970).

145. Tadano, T. & Tsuneyuki, S. Self-consistent phonon calculations of lattice dynamical properties in cubic SrTiO with first-principles anharmonic force constants. *Phys. Rev. B* **92**, 54301 (2015).

146. Tadano, T. & Tsuneyuki, S. First-Principles Lattice Dynamics Method for Strongly Anharmonic Crystals. *J. Phys. Soc. Japan* **87**, 41015 (2018).

147. Hooton, D. J. The use of a model in anharmonic lattice dynamics. *Philos. Mag.* **3**, 49–54 (1958).

148. Maradudin, A. A. & Fein, A. E. Scattering of Neutrons by an Anharmonic Crystal. *Phys. Rev.* **128**, 2589–2608 (1962).

149. Lang, G. *et al.* Anharmonic line shift and linewidth of the Raman mode in covalent semiconductors. *Phys. Rev. B* **59**, 6182 (1999).

150. Lazzeri, M., Calandra, M. & Mauri, F. Anharmonic phonon frequency shift in MgB2. *Phys. Rev. B* **68**, 220509(R) (2003).

151. Bonini, N., Lazzeri, M., Marzari, N. & Mauri, F. Phonon Anharmonicities in Graphite and Graphene. *Phys. Rev. Lett.* **99**, 176802 (2007).

152. Feng, T., Yang, X. & Ruan, X. Phonon anharmonic frequency shift induced by four-phonon scattering calculated from first principles. *J. Appl. Phys.* **124**, 145101 (2018).

153. Zee, A. Quantum field theory in a nutshell. *Princet. Univ. Press* (2010).

154. Mattuck, R. D. *A guide to Feynman diagrams in the many-body problem*. (Courier Corporation, 1992).

155. Towns, J. *et al.* XSEDE: Accelerating Scientific Discovery. *Comput. Sci. Eng.* **16**, 62–74 (2014).

156. We used the pseudopotentials Sn.pz-dn-kjpaw_psl.0.2.UPF and Se.pz-n-kjpaw_psl.0.2.UPF from http://www.quantum-espresso.org.

157. Morita, A. Semiconducting black phosphorus. *Appl. Phys. A Solids Surfaces* **39**, 227–242 (1986).

158. Sugai, S. & Shirotani, I. Raman and infrared reflection spectroscopy in black phosphorus. *Solid State Commun.* **53**, 753–755 (1985).

159. Wu, J., Mao, N., Xie, L., Xu, H. & Zhang, J. Identifying the crystalline orientation of black phosphorus using angle-resolved polarized Raman spectroscopy. *Angew. Chemie - Int. Ed.* **54**, 2366–2369 (2015).

160. Zeng, L. *et al.* Measuring Phonon Mean Free Path Distributions by Probing Quasiballistic Phonon Transport in Grating Nanostructures. *Sci. Rep.* **5**, 17131 (2015).

161. Bard, A. J. & Faulkner, L. R. *Electrochemical Methods*. (2001).

162. Zhao, S. J., Kang, W. & Xue, J. M. The potential application of phosphorene as an anode material in Li-ion batteries. *J. Mater. Chem. A* **2**, 19046–19052 (2014).

163. Li, Q. F., Duan, C. G., Wan, X. G. & Kuo, J. L. Theoretical prediction of anode materials in Li-ion batteries on layered black and blue phosphorus. *J. Phys. Chem. C* **119**, 8662–8670 (2015).

164. Zhang, C., Anderson, G., Dharmasena, R. R., Sumanasekera, G. & Yu, M. Phosphorene as an Anode Material for High Performance Lithium-Ion Battery: First Principle Study and Experimental Measurement. *arXiv* arXiv:1607.00317 (2016).

165. Sun, J. *et al.* A phosphorene-graphene hybrid material as a high-capacity anode for sodium-ion batteries. *Nat. Nanotechnol.* **10**, 980–985 (2015).

166. Li, W., Yang, Y., Zhang, G. & Zhang, Y. W. Ultrafast and directional diffusion of lithium in phosphorene for high-performance lithium-ion battery. *Nano Lett.* **15**, 1691–1697 (2015).

167. Park, C.-M. & Sohn, H.-J. Black phosphorus and its composite for lithium rechargeable batteries. *Adv. Mater.* **19**, 2465–2468 (2007).

168. Nazri, G. A., Julien, C. & Mavi, H. S. Structure of Li3X (X = N, P, As) superionic conductors: X-ray diffraction and FTIR studies. *Solid State Ionics* **70–71**, 137–143 (1994).

169. Sun, J. *et al.* Formation of stable phosphorus-carbon bond for enhanced performance in black phosphorus nanoparticle-graphite composite battery anodes. *Nano Lett.* **14**, 4573–4580 (2014).

170. Seol, J. H. *et al.* Two-Dimensional Phonon Transport in Supported Graphene. *Science (80-.).* **328**, 213–216 (2010).

171. Cai, W. *et al.* Thermal transport in suspended and supported monolayer graphene grown

by chemical vapor deposition. *Nano Lett.* **10**, 1645–1651 (2010).

172. Lindsay, L. *et al.* Phonon thermal transport in strained and unstrained graphene from first principles. *Phys. Rev. B* **89**, 155426 (2014).

173. Jain, A. & McGaughey, A. J. H. Strongly anisotropic in-plane thermal transport in single-layer black phosphorene. *Sci. Rep.* **5**, 8501 (2015).

174. Callaway, J. Model for lattice Thermal Conductivity at Low Temperatures. *Phys. Rev.* **113**, 1046–1051 (1959).

175. Abeles, B. Lattice thermal conductivity of disordered semiconductor alloys at high temperatures. *Phys. Rev.* **131**, 1906–1911 (1963).

176. Zhou, Z., Uher, C., Jewell, A. & Caillat, T. Influence of point-defect scattering on the lattice thermal conductivity of solid solution Co(Sb1-xAsx)3. *Phys. Rev. B* **71**, 235209 (2005).

177. Mayo, M., Griffith, K. J., Pickard, C. J. & Morris, A. J. Ab Initio Study of Phosphorus Anodes for Lithium- and Sodium-Ion Batteries. *Chem. Mater.* **28**, 2011–2021 (2016).

178. Regner, K. T. *et al.* Broadband phonon mean free path contributions to thermal conductivity measured using frequency domain thermoreflectance. *Nat. Commun.* **4**, 1640 (2013).

179. Chen, Z., Wei, Z., Chen, Y. & Dames, C. Anisotropic Debye model for the thermal boundary conductance. *Phys. Rev. B* **87**, 125426 (2013).

180. Li, B., Wang, L. & Casati, G. Negative differential thermal resistance and thermal transistor. *Appl. Phys. Lett.* **88**, 143501 (2006).

181. Xu, F. *et al.* Scalable shear-exfoliation of high-quality phosphorene nanoflakes with reliable electrochemical cycleability in nano batteries. *2D Mater.* **3**, 025005 (2016).

182. Qin, G. Z. *et al.* Anisotropic intrinsic lattice thermal conductivity of phosphorene from first principles. *Phys. Chem. Chem. Phys.* **17**, 4854–4858 (2015).

183. Liu, T. H. & Chang, C. C. Anisotropic thermal transport in phosphorene: effects of crystal orientation. *Nanoscale* **7**, 10648–10654 (2015).

184. Luo, Z. *et al.* Anisotropic in-plane thermal conductivity observed in few-layer black phosphorus. *Nat. Commun.* **6**, 8572 (2015).

185. Lee, S. *et al.* Anisotropic in-plane thermal conductivity of black phosphorus nanoribbons at temperatures higher than 100 K. *Nat. Commun.* **6**, 8573 (2015).

186. Hong, Y., Zhang, J., Huang, X. & Zeng, X. C. Thermal Conductivity of Phosphorene Nanoribbon: A Comparative Study with Graphene. *Nanoscale* 18716–18724 (2015).

187. Xu, W., Zhu, L., Cai, Y., Zhang, G. & Li, B. Direction dependent thermal conductivity of monolayer phosphorene: Parameterization of Stillinger-Weber potential and molecular dynamics study. *J. Appl. Phys.* **117**, 214308 (2015).

188. Zhang, J. *et al.* Thermal conductivities of phosphorene allotropes from first-principle calculations : a comparative study. *Sci. Rep.* **7**, 4623 (2017).